

**POOL AND FLOW BOILING OF NOVEL HEAT TRANSFER  
FLUIDS FROM NANOSTRUCTURED SURFACES**

A Dissertation  
Presented to  
The Academic Faculty

by

Aravind Sathyanarayana

In Partial Fulfillment  
of the Requirements for the Degree  
Doctor of Philosophy in the  
George W. Woodruff School of Mechanical Engineering

Georgia Institute of Technology  
December 2013

Copyright © 2013 by Aravind Sathyanarayana

**POOL AND FLOW BOILING OF NOVEL HEAT TRANSFER  
FLUIDS FROM NANOSTRUCTURED SURFACES**

Approved by:

Dr. Yogendra Joshi, Advisor  
School of Mechanical Engineering  
*Georgia Institute of Technology*

Dr. Samuel Graham  
School of Mechanical Engineering  
*Georgia Institute of Technology*

Dr. Aryn S. Teja  
School of Chemical and Biomolecular  
Engineering  
*Georgia Institute of Technology*

Dr. Sushil Bhavnani  
School of Mechanical Engineering  
*Auburn University*

Dr. Mostafa S. Ghiaasiaan  
School of Mechanical Engineering  
*Georgia Institute of Technology*

Date Approved: October 8, 2013

To my grandparents, *G. Sriramulu Pillai* and *K. Jambavathi*

## ACKNOWLEDGEMENTS

I would like to express my sincere gratitude to all the people who have helped me during the course of my doctoral study at Georgia Tech. First and foremost, I would like to thank my PhD advisor, Dr. Yogendra Joshi, for his constant support, guidance as well as for his comments and critiques. He continually stimulated my thinking ability and made me capable of performing independent research. I have had the opportunity to interact with several researchers who visited our lab, present my work at various conferences and I cannot thank him enough for this enriching experience.

This work was performed in collaboration with Dr. Aryn Teja from the School of Chemical and Biomolecular Engineering at Georgia Tech, and I would like to thank him for his guidance in the chemistry aspects of this work. I am also grateful to my PhD committee members Dr. Sushil Bhavnani, Dr. Mostafaa Ghiaasiaan and Dr. Samuel Graham, for their valuable feedback, as well as reviewing the proposal and dissertation. This work was funded by the Office of Naval Research and I would like to acknowledge their financial support.

I have worked with Dr. Pramod Warriar as a part of this research work, and I would like to acknowledge his help in evaluating the properties of all the fluids and for providing me with the custom fluids in a timely manner. I would specially like to thank Dr. Yunhyeok Im, a visiting scholar in our group, for graciously allowing me to use his pool boiling setup for my research. I have learnt a lot working with him in the lab and I would always cherish those memories. My thanks are also due to Dr. Minami Yoda and Dr. David Hu for letting me borrow the high speed camera for my experiments. I would

also like to thank Dr. Naveenan Thiagarajan at Auburn University for his help in measuring dissolved gas percentages.

I extend many thanks to all my colleagues in the Microelectronics and Emerging Technologies Thermal Laboratory (METTL) for their valuable feedback during our group meetings and also for training me on several tools. I would specially like to thank Dr. Pramod Kumar and Dr. Krishna Kota for their valuable advice during the initial stages of my research. I have had several informal discussions with them over various topics and they have greatly influenced me as a thinker.

I am grateful to all the staff members at the Microelectronics Research Center (MiRC) for their invaluable help and guidance with the micro-fabrication tools and processes in the cleanroom. I would also like to thank Mr. Louis Boulanger in the ME machine shop for machining the test section for flow boiling experiments. My special thanks go to Mrs. Regina Neequaye for her help in ordering all the components required for my research.

I have made a lot of good friends during my stay in Atlanta, and I would like to thank each and every one of them for making me feel at home all these years. Last but not the least, I express my deepest gratitude to my parents, siblings, my uncle Nagaraju's family and my aunt Usha's family for their unconditional love and encouragement throughout my life. I would not have been in this position today without their support.

# TABLE OF CONTENTS

	Page
ACKNOWLEDGEMENTS.....	iv
LIST OF TABLES.....	x
LIST OF FIGURES.....	xi
NOMENCLATURE.....	xv
SUMMARY.....	xviii
<b>CHAPTER 1: INTRODUCTION.....</b>	<b>1</b>
1.1 Motivation.....	1
1.2 Heat Transfer Fluid Selection - Approaches.....	3
1.2.1 Ad hoc Approach.....	3
1.2.2 Enhancing the Properties of Existing Fluids.....	4
1.2.3 Computer Aided Molecular Design.....	4
1.3 Research Objectives.....	5
1.4 Thesis Outline.....	5
<b>CHAPTER 2: LITERATURE REVIEW.....</b>	<b>8</b>
2.1 Pool Boiling of Mixtures.....	8
2.1.1 Pool Boiling of Aqueous and Alcohol Mixtures.....	8
2.1.2 Pool Boiling of Dielectric Liquid Mixtures.....	11
2.2 Flow Boiling of Mixtures.....	13
2.3 Summary.....	15
<b>CHAPTER 3: DESIGN OF HEAT TRANSFER FLUIDS.....</b>	<b>16</b>
3.1 Computer Aided Molecular Design.....	16
3.2 Fluid Property Prediction.....	19

3.2.1 Group Contribution Methods.....	19
3.2.2 Evaluation of Group Contribution Methods .....	20
3.3 Constraints on Fluid Properties.....	21
3.4 Figure of Merit Analysis.....	23
3.5 New Heat Transfer Fluids.....	27
3.6 Summary .....	28
<b>CHAPTER 4: FLUID PROPERTIES.....</b>	<b>29</b>
4.1 Thermophysical Properties Measurement.....	29
4.2 Contact Angle .....	32
4.3 Vapor Liquid Equilibrium Curves .....	35
4.4 Summary .....	39
<b>CHAPTER 5: POOL BOILING EXPERIMENTS. ....</b>	<b>41</b>
5.1 Experimental Setup.....	41
5.2 Test Chip Fabrication.....	43
5.3 Experimental Procedure.....	50
5.4 Measurement Uncertainty.....	52
5.5 Experimental Results .....	54
5.5.1 Effect of Enhanced Surface .....	54
5.5.2 Pool Boiling of HFE 7200 – Ethoxybutane and HFE 7200 – Methanol Mixtures .....	55
5.5.3 Pool Boiling of HFE 7200 – C <sub>6</sub> H <sub>11</sub> F <sub>3</sub> Mixture .....	59
5.5.4 Pool Boiling of HFE 7200 – C <sub>4</sub> H <sub>4</sub> F <sub>6</sub> O Mixture.....	63
5.5.5 Pool Boiling of HFE 7200 – C <sub>4</sub> H <sub>5</sub> F <sub>3</sub> O Mixture.....	65
5.5.6 Pool Boiling of HFE 7200 – C <sub>4</sub> H <sub>12</sub> O <sub>2</sub> Si Mixture .....	67
5.5.7 Pool Boiling of HFE 7200 – C <sub>4</sub> H <sub>11</sub> N Mixture .....	69
5.6 CHF Prediction for Higher Mixture Concentrations .....	71

5.7 CHF Mechanism .....	74
5.8 Summary .....	78
<b>CHAPTER 6: POOL BOILING SIMULATIONS .....</b>	<b>80</b>
6.1 Need for Numerical Simulations .....	80
6.2 Phase Field Method.....	83
6.2.1 Interface Equations .....	84
6.2.2 Conservation Equations .....	86
6.3 Pool Boiling Model.....	88
6.3.1 Computational Model .....	89
6.3.2 Boundary Conditions .....	91
6.4 Simulation Results .....	95
6.4.1 Effect of Grid Size .....	95
6.4.2 Simulations using HFE 7200 and C4H4F6O.....	98
6.4.3 Possible Reasons for Discrepancy .....	104
6.4.4 Effect of Constant ‘C’ on Simulation Results.....	105
6.5 Validation with Experimental Results .....	107
6.6 Summary .....	110
<b>CHAPTER 7: FLOW BOILING EXPERIMENTS .....</b>	<b>111</b>
7.1 Experimental Setup.....	111
7.2 Microgap Channel Test Section.....	113
7.3 Leak Test and Degassing .....	118
7.4 Experimental Procedure.....	118
7.5 Data Reduction.....	119
7.6 Calibration and Measurement Uncertainty .....	121
7.7 Experimental Results .....	122



7.7.1 Flow Boiling on Polished Surface .....	123
7.7.2 Flow Boiling on Unpolished Surface.....	131
7.8 Summary .....	136
<b>CHAPTER 8: CONCLUSIONS AND FUTURE WORK.....</b>	<b>137</b>
8.1 Conclusions.....	137
8.2 Recommendations for Future Work.....	139
8.2.1 New Fluid Synthesis .....	139
8.2.2 Pool Boiling Experiments .....	139
8.2.3 Pool Boiling Modeling.....	140
8.2.4 Flow Boiling Experiments .....	140
<b>REFERENCES.....</b>	<b>141</b>

## LIST OF TABLES

	Page
Table 3.1: Screening of compounds for structural feasibility.....	18
Table 3.2: Properties of some existing coolants .....	22
Table 3.3: FOM correlations.....	24
Table 3.4: FOM for HFE 7200, and cut-off values for candidate fluids .....	25
Table 3.5: Candidate fluids selected after FOM analysis .....	26
Table 4.1: Supplier information for heat transfer fluids .....	30
Table 4.2: Thermophysical property measurements of new fluids.....	30
Table 4.3: Properties of heat transfer fluids considered for experiments .....	31
Table 5.1: Uncertainties in parameters .....	53
Table 5.2: CHF predictions.....	78
Table 6.1: Boundary conditions and initial conditions for the computational model.....	91
Table 6.2: Mesh statistics and solution time for grid size dependence study .....	96
Table 6.3: Properties of heat transfer fluids considered for simulations .....	99
Table 6.4: Mesh statistics and solution time for different fluids .....	99
Table 6.5: Comparison between theoretical predictions and simulations for the bubble departure diameter.....	103
Table 6.6: Comparison between theoretical predictions and simulations for the bubble departure frequency.....	103
Table 7.1: Flow boiling experimental conditions .....	122

## LIST OF FIGURES

	Page
Figure 3.1: CAMD – FOM approach.....	17
Figure 4.1: Contact angle measurement system .....	32
Figure 4.2: Instantaneous droplet shape of HFE 7200 on a plain surface .....	34
Figure 4.3: Instantaneous droplet shape of $C_6H_{11}F_3$ on a plain surface.....	34
Figure 4.4: Instantaneous droplet shape of $C_4H_4F_6O$ on a plain surface .....	34
Figure 4.5: Instantaneous droplet shape of water on a plain surface .....	35
Figure 4.6: Vapor liquid equilibrium curve for mixture of HFE 7200 – ethoxybutane...36	
Figure 4.7: Vapor liquid equilibrium curve for mixture of HFE 7200 – methanol .....	37
Figure 4.8: Vapor liquid equilibrium curve for mixture of HFE 7200 – $C_6H_{11}F_3$ .....	37
Figure 4.9: Vapor liquid equilibrium curve for mixture of HFE 7200 – $C_4H_4F_6O$ .....	38
Figure 4.10: Vapor liquid equilibrium curve for mixture of HFE 7200 – $C_4H_5F_3O$ .....	38
Figure 4.11: Vapor liquid equilibrium curve for mixture of HFE 7200 – $C_4H_{12}O_2Si$ .....	39
Figure 5.1: Schematic of pool boiling experimental setup .....	42
Figure 5.2: Test chip package mounted on the Teflon block.....	43
Figure 5.3: Test chip fabrication process .....	44
Figure 5.4: Platinum RTD fabricated on the backside of the chip.....	45
Figure 5.5: SEM image of Cu nanowire array (height of nanowires - 4 $\mu m$ ).....	47
Figure 5.6: SEM image of Cu nanowire array (height of nanowires - 20 $\mu m$ ).....	47
Figure 5.7: SEM image of CuO hybrid micro-nanostructured surface_1.....	48
Figure 5.8: SEM image of CuO hybrid micro-nanostructured surface_2.....	48
Figure 5.9: Temperature – resistance calibration curve for Pt RTD.....	50
Figure 5.10: Pool boiling of HFE 7200 on a bare chip, Cu groove surface (width – 70 $\mu m$ and depth - 70 $\mu m$ ), 3 $\mu m$ tall and 20 $\mu m$ tall Cu nanowire surfaces.....	54

Figure 5.11: Pool boiling curves for HFE 7200, 10 vol. % mixtures of HFE 7200 – ethoxybutane and HFE 7200 – methanol at saturation condition on 4 $\mu\text{m}$ nanowire array .....	56
Figure 5.12: Pool boiling curves for HFE 7200, 10 vol. % mixtures of HFE 7200 – ethoxybutane and HFE 7200 – methanol at 10K subcooling on 4 $\mu\text{m}$ nanowire array .....	57
Figure 5.13: Pool boiling curves for HFE 7200, 10 vol. % mixtures of HFE 7200 – ethoxybutane and HFE 7200 – methanol at 20K subcooling on 4 $\mu\text{m}$ nanowire array .....	59
Figure 5.14: Pool boiling curves for HFE 7200 at saturation condition on hybrid micro - nanostructured surface.....	61
Figure 5.15: Pool boiling curves for 7 wt. % mixture of HFE 7200 – $\text{C}_6\text{H}_{11}\text{F}_3$ at saturation condition on hybrid micro-nanostructured surface .....	62
Figure 5.16: Pool boiling curves for HFE 7200 at saturation condition on hybrid micro-nanostructured surface.....	63
Figure 5.17: Pool boiling curve for 10 wt. % mixture of HFE 7200 – $\text{C}_4\text{H}_4\text{F}_6\text{O}$ at saturation condition on hybrid micro-nanostructured surface.....	64
Figure 5.18: Pool boiling curves for HFE 7200 at saturation condition on hybrid micro-nanostructured surface.....	65
Figure 5.19: Pool boiling curve for 20 wt. % mixture of HFE 7200 – $\text{C}_4\text{H}_5\text{F}_3\text{O}$ at saturation condition on hybrid micro-nanostructured surface.....	66
Figure 5.20: Pool boiling curves for HFE 7200 at saturation condition on hybrid micro-nanostructured surface.....	67
Figure 5.21: Pool boiling curves for 10 wt. % mixture of HFE 7200 – $\text{C}_4\text{H}_{12}\text{O}_2\text{Si}$ at saturation condition on hybrid micro-nanostructured surface.....	68
Figure 5.22: Sediments deposited during saturated boiling of 10 wt. % mixture of $\text{C}_4\text{H}_{11}\text{N}$ – HFE 7200 on a) glass walls, and b) test chip .....	70
Figure 5.23: CHF prediction for different concentrations of new fluid – HFE 7200 mixtures on an infinite heater .....	72
Figure 5.24: CHF prediction for different concentrations of new fluid – HFE 7200 mixtures on a small heater of area 10 x 10 $\text{mm}^2$ .....	73
Figure 5.25: Cavities on a nanowire (200 nm diameter, 20 $\mu\text{m}$ tall) coated surface .....	76
Figure 6.1: Saturated pool boiling of HFE 7200 at 2.5 $\text{W}/\text{cm}^2$ (2000 fps).....	82

Figure 6.2: Saturated pool boiling of HFE 7200 at 19.5 W/cm <sup>2</sup> (2000 fps).....	83
Figure 6.3: Interface between two immiscible phases, a) Actual interface, and b) Diffuse interface in PFM.....	85
Figure 6.4: Computational model with key dimensions .....	89
Figure 6.5: Domains occupied by the liquid and vapor phases initially.....	90
Figure 6.6: Mesh settings for a) Case 1, and b) Case 2 .....	96
Figure 6.7: Fluid volume fraction plots before bubble departure for a) Case 1, and b) Case 2.....	98
Figure 6.8: Fluid volume fraction plots before bubble departure for a) HFE 7200, and b) C <sub>4</sub> H <sub>4</sub> F <sub>6</sub> O .....	100
Figure 6.9: Fluid volume fraction plots before bubble departure for a) C = 0.005 m/s and b) C = 0.1 m/s.....	106
Figure 6.10: Fluid volume fraction plots before bubble departure for a) q'' = 1 W/cm <sup>2</sup> , b) q'' = 4 W/cm <sup>2</sup> , c) q'' = 6 W/cm <sup>2</sup> , and d) q'' = 8 W/cm <sup>2</sup> .....	109
Figure 7.1: Schematic of the flow boiling experimental setup .....	112
Figure 7.2: a) Cross-sectional view of test section assembly, and b) exploded view of the microgap channel .....	116
Figure 7.3: Copper block a) Front view, and b) Side view (all dimensions in mm).....	117
Figure 7.4: Three regions of the microgap test section used for high speed visualization .....	123
Figure 7.5: SEM image of the polished copper surface (top view) .....	124
Figure 7.6: SEM image of the edge of the polished copper surface (top view) .....	124
Figure 7.7: Flow boiling curve for HFE 7200 at subcooled condition on a polished Cu surface .....	125
Figure 7.8: Flow boiling curve for 20 wt. % mixture of HFE 7200 - methanol at subcooled condition on a polished Cu surface .....	125
Figure 7.9: Flow boiling of HFE 7200 at subcooled condition on a polished Cu surface at 6 W/cm <sup>2</sup> .....	128
Figure 7.10: Flow boiling of 20 wt. % HFE 7200 – methanol mixture at subcooled condition on a polished Cu surface at 7 W/cm <sup>2</sup> .....	128

Figure 7.11: Flow boiling of HFE 7200 at subcooled condition on a polished Cu surface at 11 W/cm <sup>2</sup> .....	129
Figure 7.12: Flow boiling of 20 wt. % HFE 7200 – methanol mixture at subcooled condition on a polished Cu surface at 11 W/cm <sup>2</sup> .....	129
Figure 7.13: Flow boiling of HFE 7200 at subcooled condition on a polished Cu surface at 15 W/cm <sup>2</sup> .....	130
Figure 7.14: Flow boiling of 20 wt. % HFE 7200 – methanol mixture at subcooled condition on a polished Cu surface at 15 W/cm <sup>2</sup> .....	130
Figure 7.15: Flow boiling curve for HFE 7200 at subcooled condition on an unpolished Cu surface.....	132
Figure 7.16: Flow boiling curve for 20 wt. % mixture of HFE 7200 - methanol at subcooled condition on an unpolished Cu surface .....	132
Figure 7.17: Flow boiling of HFE 7200 at subcooled condition on an unpolished Cu surface at 6 W/cm <sup>2</sup> .....	133
Figure 7.18: Flow boiling of 20 wt. % HFE 7200 – methanol mixture at subcooled condition on an unpolished Cu surface at 7 W/cm <sup>2</sup> .....	133
Figure 7.19: Flow boiling of HFE 7200 at subcooled condition on an unpolished Cu surface at 11 W/cm <sup>2</sup> .....	134
Figure 7.20: Flow boiling of 20 wt. % HFE 7200 – methanol mixture at subcooled condition on an unpolished Cu surface at 11 W/cm <sup>2</sup> .....	134
Figure 7.21: Flow boiling of HFE 7200 at subcooled condition on an unpolished Cu surface at 15 W/cm <sup>2</sup> .....	135
Figure 7.22: Flow boiling of 20 wt. % HFE 7200 – methanol mixture at subcooled condition on an unpolished Cu surface at 15 W/cm <sup>2</sup> .....	135

## NOMENCLATURE

A	area [m <sup>2</sup> ]
$c_p$	specific heat [J/kg-K]
$C_E$	Ergun coefficient
d	bubble departure diameter [m]
D	height of the nanostructures [m]
f	bubble departure frequency [Hz]
F	free energy function
g	gravitational acceleration [m/s <sup>2</sup> ]
$h_{fg}$	latent heat of vaporization [J/kg]
I	current [A]
K	permeability of the porous structure
L	length [m]
$L'$	non-dimensional heater size
m	total number of free bonds
$\dot{m}$	mass flux [kg/s]
p	number of groups
P	absolute pressure [kPa]
q	number of rings in the structure
$q''$	heat flux [W/cm <sup>2</sup> ]
$\dot{Q}$	heat transfer rate [W]
R	resistance [ $\Omega$ ]
t	time [s]

T	temperature [K]
u	velocity [m/s]
V	voltage [V]
$\dot{V}$	volumetric flow rate [m <sup>3</sup> /s]
V <sub>f</sub>	volume fraction
w	uncertainty
W	width [m]
x	molefraction of more volatile component in the liquid phase
y	molefraction of more volatile component in the vapor phase

### **Greek Symbols**

$\rho$	density [kg/m <sup>3</sup> ]
$\rho_e$	electrical resistivity [ $\Omega$ -m]
$\varepsilon$	capillary width [m]
$\varepsilon_s$	nanowire packing configuration
$\kappa$	thermal conductivity [W/m-K]
$\sigma$	surface tension [N/m]
$\mu$	dynamic viscosity [Pa.s]
$\theta$	contact angle [deg]
$\lambda$	mixing energy density
$\lambda_d$	Taylor wavelength [m]
$\varphi_s$	porosity of the nanowire subarray
$\phi$	phase field variable
$\gamma$	mobility [m <sup>3</sup> -s/kg]
$\delta$	smoothed representation of the interface



## **Subscripts**

b	boiling/bubble point
c	capillary
CHF	critical heat flux
CHF_Z	critical heat flux based on Zuber's correlation
CHF_f	critical heat flux based on far field mechanism
CHF_c	critical heat flux based on near field mechanism
in	inlet
int	interface
l	saturated liquid
out	outlet
sat	saturated condition
v	saturated vapor
w	heater surface (wall)

## SUMMARY

Steadily increasing heat dissipation in electronic devices has generated renewed interest in direct immersion cooling. The ideal heat transfer fluid for direct immersion cooling applications should be chemically and thermally stable, and compatible with the electronic components. These constraints have led to the use of Novec fluids and fluoro-inerts as coolants. Although these fluids are chemically stable and have low dielectric constants, they are plagued by poor thermal properties. These factors necessitate the development of new heat transfer fluids with improved heat transfer properties and applicability.

Computer Aided Molecular Design (CAMD) approach was used in this work to systematically design novel heat transfer fluids that exhibit significantly better properties than those of current high performance electronic coolants. The candidate fluids generated by CAMD were constrained by limiting their boiling points, latent heat of vaporization and thermal conductivity. The selected candidates were further screened using a figure of merit (FOM) analysis. Some of the fluids/additives that have been identified after the FOM analysis include  $C_4H_5F_3O$ ,  $C_4H_4F_6O$ ,  $C_6H_{11}F_3$ ,  $C_4H_{12}O_2Si$ , methanol, and ethoxybutane.

The heat transfer performance of these new fluids/fluid mixtures was analyzed through pool boiling and flow boiling experiments. Pool boiling experiments were performed using mixtures of above fluids with an existing coolant (HFE 7200) on nanowire coated, and hybrid micro-nanostructured surfaces. All the fluid mixtures tested showed an improvement in the critical heat flux (CHF) when compared to the base fluid

(HFE 7200). Theoretical predictions for the CHF show that near field mechanism is the dominant one leading to CHF for pool boiling of mixtures on nanowire surfaces. A pool boiling model was developed using the phase field method available in the commercial software COMSOL. Although the simulations are computationally intensive, they provide a possible approach to evaluating several candidate fluids generated using the CAMD approach. There are several limitations to the current model, and further research is required to validate these results.

Flow boiling experiments were performed using two fluids, HFE 7200 and 20 wt. % mixture of HFE 7200 – methanol, at subcooled conditions in a microgap channel. High speed visualization was performed to analyze the bubble departure parameters. The bubble departure diameters were found to be smaller for the mixture, when compared to HFE 7200 at all heat fluxes. This could possibly be one reason for the enhancement in CHF using the mixture. Also, the mixture had the potential to handle higher heat fluxes when compared to HFE 7200.

# CHAPTER 1

## INTRODUCTION

Performance enhancement while reducing system size is a universal characteristic of technological development. In the microelectronics industry, this is exemplified by Moore's law, which states that the number of transistors in integrated circuits doubles approximately every two years. With increasing intensification of processes that generate heat, thermal management becomes critical due to increased heat fluxes. Hence, thermal management technologies must advance to match the growth in heat removal demands, along with other geometrical constraints. This work focuses on identifying and evaluating new heat transfer fluids for thermal management of microelectronic systems.

### 1.1 Motivation

Advances in semiconductor chips have led to significant thermal management challenges. Increasing heat fluxes are a direct result of an increase in transistor density, processing speeds, and more sophisticated functions being performed. Present day microelectronic systems generate heat fluxes in excess of  $100 \text{ W/cm}^2$  for a single chip,  $25 \text{ W/cm}^2$  for a multichip module, and  $10 \text{ W/cm}^2$  for a printed circuit board [1]. With the miniaturization trend and integration continuing, high performance electronic devices of the future are predicted to generate surface averaged heat fluxes of over  $1 \text{ kW/cm}^2$ , along with localized heat fluxes several times larger. Thermal management is widely regarded as a key bottleneck in further development of such systems. Such high heat fluxes can potentially be handled using forced convection of liquids, and/or direct immersion phase change cooling [1, 2].

Phase change heat transfer is characterized by high heat transfer coefficients and therefore provides an attractive solution over single phase heat transfer. In general, a high critical heat flux (CHF) is necessary so that the device can be cooled safely at higher wall superheat, without the adverse risk of burnout. There are two different approaches to enhancing the CHF at the same operating conditions (system pressure, bulk liquid temperature):

1. Modifying the surface geometry
2. Using a new heat transfer fluid/fluid mixture with better thermal properties.

The first approach has been studied extensively in the literature and a comprehensive review on boiling enhancement from modified surfaces can be found in the book by Poniewski and Thome [3]. The second approach is to use heat transfer fluids/fluid mixtures with better thermal properties for enhancing the CHF. The most commonly used heat transfer fluids for direct immersion cooling applications are either fluoroinerts (FC – 72, FC – 86, and FC – 77) or Novec fluids (HFE 7100, HFE 7200) [4]. However, these fluids are plagued by low thermal conductivity (about twice that of air) and specific heat (about the same as that of air). Also, they suffer from temperature overshoot in pool boiling applications due to low surface tensions [6], which delays the inception of nucleate boiling. Moreover, a number of these chemicals have significant environmental impact [6]. These factors necessitate the development of new heat transfer fluids with improved heat transfer properties for thermal management of future high performance microelectronic systems.

## **1.2 Heat Transfer Fluid Selection - Approaches**

New heat transfer fluids for thermal management of electronic systems should possess the following properties in order to be considered superior over existing heat transfer fluids (HFE 7200, FC – 72, etc.):

- High thermal conductivity
- High enthalpy of vaporization
- High specific heat
- Low viscosity
- Low global warming potential
- Zero ozone depletion potential

In addition, the fluids must be dielectric, compatible with system components, chemically inert, inexpensive, and possess liquid range within the operating heat transfer regime. The search for heat transfer fluids with these properties can be pursued using several approaches.

### **1.2.1 Ad hoc Approach**

Ad hoc experiments have traditionally been used to identify a large number of potential fluids. In such cases, the desired properties must be readily available or be measured. However, all potential candidates cannot be evaluated through experiments because of economic and time constraints. The list of candidates is therefore usually generated by the practitioner's insight or by scanning through existing chemical property databases. As a result, the search space using this approach is very limited and potential candidates are often not considered.

### **1.2.2 Enhancing the Properties of Existing Fluids**

The properties of existing heat transfer fluids can be augmented for specific applications by adding other miscible liquids. The properties of such fluid mixtures have a non-linear dependence on composition and this offers the potential of yielding formulations with enhanced properties. Customized formulations of liquids are routinely used in industry to obtain products with desired properties. For example, ethylene glycol is used as antifreeze in automobile applications. Adding ethylene glycol to water lowers the freezing point and increases the boiling point of the resulting mixture. This ensures that the coolant can be operated over a wide temperature range in harsh climates.

### **1.2.3 Computer Aided Molecular Design**

Computer-aided molecular design (CAMD) is able to generate a large number of candidates that satisfy specified thermo-physical property constraints [5-8] and therefore provides an attractive alternate solution for identifying new heat transfer fluids. The success of several CAMD methods has been demonstrated in identifying new heat transfer fluids [8], as well as solvents [9] and refrigerants [8, 10]. The fundamental objective of CAMD is to identify a collection of fluids having specific desired properties. CAMD can be used when validated mathematical models are available to predict all properties. Hence, this approach depends on the accuracy of the property estimation methods, and if they are not accurate, then there is a possibility that some candidates will not be selected.

### **1.3 Research Objectives**

The overall objective of this research work is to design new heat transfer fluids for direct immersion cooling applications. With this in mind, the following specific goals and objectives are proposed:

1. Develop a systematic approach to design new heat transfer fluids and fluid mixtures that is exhaustive and able to identify candidates that are outside the scope of empirical approaches.
2. Develop a ranking mechanism to screen thousands of candidate fluids generated using the CAMD approach.
3. Experimentally measure and validate the thermophysical properties of top ranked fluids with the theoretical predictions.
4. Investigate the heat transfer performance of new fluids through pool boiling and flow boiling experiments on both plain and nanostructured surfaces.
5. Develop a computational model to analyze the pool boiling performance of new heat transfer fluids, and supplement experimental observations.

### **1.4 Thesis Outline**

The overall objective of this work is to develop a systematic approach to design novel heat transfer fluids for direct immersion cooling application. The motivation for this study, approaches currently followed to select heat transfer fluids are discussed in Chapter 1. In chapter 2, a brief literature review is presented to give a perspective on the



existing state-of-the-art on boiling of mixtures. Pool and flow boiling of aqueous, dielectric fluid mixtures are reviewed in this chapter.

In Chapter 3, details of the Computer Aided Molecular Design approach employed in this work to design new heat transfer fluids is discussed. The constraints on the fluid properties, group contribution methods, and figure of merit analysis used to rank candidate fluids, are discussed in this chapter.

The thermophysical properties of candidate fluids are experimentally evaluated, and this is discussed in Chapter 4. The wetting characteristics of new fluids and the vapor liquid equilibrium curves for new fluid mixtures are presented in this chapter.

The heat transfer performance of new fluids was investigated through pool and flow boiling experiments. In Chapter 5, the details of the pool boiling experimental setup is presented. Various nanostructured surfaces were used for the experiments. The details of the test chip fabrication, experimental results using various fluid mixtures, and CHF prediction for higher mixture concentrations are discussed.

The bubble departure parameters could not be experimentally measured because of restrictions imposed by the pool boiling experimental setup. To supplement experimental observations, a pool boiling model was developed using the phase field method in COMSOL. The theory of the phase field method, computational model and its boundary conditions, grid size dependence study and the simulation results for two fluids are discussed in Chapter 6.

The FOM predictions show that new fluids would enhance heat transfer even under flow boiling conditions. To investigate this, flow boiling experiments were performed with pure HFE 7200 and HFE 7200 – Methanol mixture. In Chapter 7, the

details of the flow boiling experimental setup, microgap channel test section assembly, and experimental results using the above two fluids are discussed. Chapter 8 summarizes the entire work and provides recommendations for future work.

## **CHAPTER 2**

### **LITERATURE REVIEW**

Boiling of mixtures has been of interest for the last five decades and a vast body of research exists on this topic in the literature. Earlier work on boiling of liquid mixtures was primarily with polar, hydrocarbon liquids such as water, alcohols, acetone etc. Although these fluids have good thermal properties, they are plagued by low dielectric strength, large surface tension and are also chemically reactive. Also, the alcohol mixtures have flammability issues. Hence, these fluids cannot be used for direct immersion cooling applications. Several researchers as a result have turned to dielectric fluids.

Pool and flow boiling of pure dielectric fluids has also been studied extensively in the literature. However, there exist very few studies on pool boiling of dielectric liquid mixtures. To the best of author's knowledge, there is no work on flow boiling of dielectric liquid mixtures in the literature. In this chapter, pool and flow boiling of several liquid mixtures discussed above, are reviewed.

#### **2.1 Pool Boiling of Mixtures**

##### **2.1.1 Pool Boiling of Aqueous and Alcohol Mixtures**

Van Wijk et. al. [11] were one of the first researchers to investigate the pool boiling of mixtures. The authors studied the effect of mixture concentration on the CHF, using mixtures of water with acetone, aliphatic alcohols, ethylene glycol and methylethylketone. From their experimental results, they concluded that there exists an

optimum concentration at which the CHF is maximum and this optimum concentration depends on the number of carbon atoms in the solute. Using high speed visualization and also through qualitative analysis, they concluded that this enhancement in CHF is due to the reduction in the bubble departure diameter for mixtures when compared to the pure fluid. In a later study [12], they attributed this reduction in bubble departure diameters and increase in the CHF of mixtures to the reduction in bubble growth rates when compared to the pure fluid.

However, the above concept has the disadvantage of attributing the increase in CHF to the stagnation in vapor production because of slow bubble growth rates. Hovestrejdt [13] later explained that this enhancement in CHF could be due to surface tension gradients arising because of preferential evaporation. To further demonstrate the importance of surface tension gradients, the author performed pool boiling experiments using several positive (more volatile component has the lower surface tension) and negative (less volatile component has the lower surface tension) organic mixtures. An improvement in the CHF was observed for both positive and negative mixtures. For positive mixtures, he attributed this enhancement to the increased liquid flow towards the heater surface because of surface tension gradients along the liquid – vapor interface (Marangoni effect). The author however was not able to explain this enhancement for negative mixtures.

Avedisian and Purdy [14] also observed an enhancement in the CHF for binary mixtures over pure fluid. They conducted pool boiling experiments over a wide pressure range (136 – 205 kPa), using mixtures of n-pentane with n-propanol, n-heptane and n-decane on smooth Cu surface and high flux (Union Carbide) surfaces. From their

experimental results, they observed that the CHF increases as the concentration of the more volatile component in the mixture increases. They also observed that the high flux surfaces had higher CHF when compared to smooth surface using n-pentane/n-propanol mixture.

McGillis and Carey [15] also attributed their observed enhancement in CHF for binary mixtures to the Marangoni effect. They conducted pool boiling experiments using mixtures of water with ethylene glycol, methanol and 2-propanol on a plain copper surface. From the experimental results, they observed that small addition of alcohols to water enhanced the CHF. However, addition of ethylene glycol to water reduced the CHF when compared to pure water. They classified their mixtures into positive and negative mixtures, and explained this trend in CHF in terms of the surface tension gradients along the liquid-vapor interface. They also developed a new correlation for CHF which incorporates surface tension gradients for mixtures.

Fujita and Bai [16] reported an experimental study of CHF of binary liquid mixtures on a horizontal platinum wire. They performed saturated pool boiling experiments using mixtures of methanol – water, ethanol – water, methanol – ethanol, methanol – benzene, ethanol – n-butanol, benzene – n-heptane, and water – ethylene glycol at different concentrations. Their experimental results revealed different trends in the CHF for different mixtures. Only aqueous mixtures of methanol and water showed an improvement in the CHF, while other mixtures showed either an invariable or reduced CHF when compared to the pure fluid. They attributed this trend in CHF to the Marangoni flow induced at the liquid – vapor interface and developed a correlation for CHF in terms of the Marangoni number.

Kandlikar and Alves [17] determined that changes in the contact angle and wetting characteristics might also play an important role for pool boiling of binary mixtures. The authors conducted pool boiling experiments using mixtures of water with ethylene glycol at low concentrations (1 – 10 wt. %). They observed a moderate improvement in the heat transfer coefficient for the binary mixture when compared to pure water. They determined that effects of binary diffusion and surface tension gradients were negligible at low mixture concentrations, and attributed this improvement in heat transfer coefficient to the changes in contact angle and wetting characteristics of the binary mixture.

Sakashita et. al. [18] investigated the saturated pool boiling of 2-propanol/water mixtures on a horizontal disk at atmospheric pressure. Using these mixtures, the authors reported an improvement in the CHF of up to 1.7 times the CHF of pure water. To determine the mechanism behind this enhancement, the authors studied the liquid-vapor distribution over the heater surface using a conductance probe. They observed that the liquid-vapor structures were distributed non-uniformly over the heater surface and that the void fractions were small at the central region and large near the periphery of the heater surface. For the mixtures, the liquid layer between the vapor and the heater surface was considerably thicker than that of water at the central region, and was thinner at the periphery. They speculated that the thicker liquid layer for mixtures could be the reason for CHF enhancement.

### **2.1.2 Pool Boiling of Dielectric Liquid Mixtures**

Normington et. al. [19] investigated the effect of mixing dielectric fluids on the CHF and temperature overshoot. They performed subcooled pool boiling experiments

using two families of dielectric liquids: 3M's perfluorocarbon fluids (FC-84 and FC-104) and Austimont's perfluoropolyether (D80 and HT110) mixtures. From the experimental data, the authors observed that the mixtures exhibited a dramatic reduction in the temperature overshoot when compared to the pure fluids. They also found that the CHF increased with increasing concentration of HT – 110, but that the mixtures of perfluorocarbon did not show any improvement in the CHF. The authors however, could not explain the mechanism behind this effect.

Watwe and Bar-Cohen [20] studied the pool boiling heat transfer characteristics of FC-72, FC-40 mixtures. They observed a significant enhancement in the CHF using low mixture concentrations (5 – 10 %) of FC-72. The authors explained that this enhancement in the CHF could be due to the localized depletion of more volatile component near the heater surface. They concluded that the addition of liquid with higher boiling point, higher molecular weight, higher surface tension and higher viscosity would lead to significant enhancement in the CHF.

More recently, Arik and Bar-Cohen [21] demonstrated significant enhancement in the CHF using mixtures of FC-72 and FC-40. The authors performed pool boiling experiments using several mixture concentrations (10 wt. %, 15 wt. % and 20 wt. % of FC-40 in FC-72,) at different pressures and different levels of subcooling. All the mixtures tested showed an improvement in the CHF and also, the CHF increased with increasing pressure and level of subcooling for all concentrations. The authors attributed this enhancement in the CHF to the improvement in thermal properties (latent heat of vaporization, surface tension) of the mixture in addition to the preferential evaporation of low boiling point liquid near the heater surface

## 2.2 Flow Boiling of Mixtures

Bennett and Chen [22] were one of the first researchers to investigate the flow boiling of aqueous mixtures. The authors performed subcooled flow boiling experiments using mixtures of water and ethylene glycol. From their experimental data, the authors revealed that Prandtl number plays an important role in boiling heat transfer for both pure fluids and mixtures. The authors also observed a significant reduction in the heat transfer coefficient for mixtures and they attributed this degradation to mass transfer effects.

Sivagnanam and Varma [23] studied the subcooled flow boiling of aqueous mixtures at different flow rates, degrees of subcooling and mixture concentrations. The authors performed experiments using acetone – water, isopropanol – water, and n-butanol – water mixtures. The experimental results revealed an increase in the wall superheat at the onset of subcooled boiling as the molefraction of the more volatile component was increased.

Peng et al. [24] studied the subcooled flow boiling heat transfer characteristics of methanol – water mixtures in microchannel plates. They observed that the concentration of more volatile component in the mixture has a great effect on the boiling heat transfer. Their results exhibited an optimum concentration at which the flow boiling heat transfer was maximum. The heat transfer increased at low concentrations of methanol, and decreased at higher concentrations.

McAssey and Kandlikar [25] compared the heat transfer performance of two binary mixtures for automotive engine cooling application. They performed saturated and subcooled flow boiling experiments using mixtures of water with ethylene glycol and



propylene glycol, in a horizontal aluminum channel. From their experimental results, they concluded that the thermal performance of both coolant mixtures were very similar.

Rivera et. al. [26] investigated the flow boiling heat transfer characteristics of water – lithium bromide mixtures (48 – 58 wt. %) in a vertical tube. From their experimental data, the authors concluded that the heat transfer coefficients depend strongly on the mixture concentration and the mass flux. The average heat transfer coefficients for the mixture increased with a decrease of the solute concentration, and increase of mass flux. Also, the local heat transfer coefficient was found to be strongly dependent on the Boiling number and Martinelli parameter.

Kandlikar and Bulut [27] reported an experimental study on subcooled flow boiling of ethylene glycol – water mixture at various concentrations (0 – 40 wt. %). The authors observed that as the concentration of ethylene glycol in the mixture increases, the heat transfer performance deteriorates. They attributed this degradation to the adverse effects of mass diffusion on boiling heat transfer.

Lin et. al. [28] investigated experimentally the boiling heat transfer and CHF of methanol – water mixtures, in a diverging microchannel with artificial cavities. They found that at a given mass flux, the CHF increases gradually as the concentration of ethanol in water increases, reaches a maximum at an optimum concentration and thereafter, decreases rapidly with the increasing concentration. The authors attributed this enhancement to the Marangoni effect that drives the liquid flow towards the contact line. High speed visualization also demonstrated that the flow pattern of liquid film breakup persisted to a high heat flux at this optimum concentration than other concentrations. In another study, Fu et. al. [29] also reported similar results for flow boiling using mixtures

of ethanol – water. The CHF was maximum at an optimum concentration (0.1 molefraction of ethanol in water).

More recently, Sarafraz and Peyghambarzadeh [30] investigated the subcooled flow boiling of water – diethylene glycol (DEG) mixtures in a vertical annulus. From the experimental results, the authors observed that flow boiling heat transfer coefficient increases at low mixture concentrations (0 – 4 vol. %). However, for mixture concentrations above 5 vol. %, the heat transfer coefficient deteriorated when compared to pure water. The authors speculated that reduction of surface tension by the addition of DEG could be responsible for the enhancement in heat transfer coefficient at low concentrations.

### **2.3 Summary**

A detailed literature review on pool and flow boiling of mixtures is presented in this chapter. A number of investigations on boiling of aqueous solutions have been carried out and are readily available in the literature. However, very few studies exist on pool boiling of dielectric liquid mixtures, and no work is available on flow boiling of dielectric liquid mixtures. The experimental results available in the literature show a mixed trend for boiling heat transfer of mixtures. Some studies have shown an improvement in the CHF with increase in mixture concentration, while other studies have shown that there exists an optimum concentration at which the CHF is maximum. However, it can be inferred from these investigations that preferential evaporation of the more volatile component at the heater surface, and changes in mixture properties with concentration might play an important role in boiling heat transfer of mixtures.

## **CHAPTER 3**

### **DESIGN OF HEAT TRANSFER FLUIDS**

Computer-aided molecular design (CAMD) approach has been used to identify new heat transfer fluids for direct immersion cooling of electronic systems. This was accomplished using Integrated Computer Aided Systems (ICAS) software developed by the Computer Aided Process-Product Engineering Center (CAPEC) of the Technical University of Denmark. The candidate fluids identified using CAMD were screened using figure of merit (FOM) analysis. Fluids with FOMs greater than those of an existing coolant HFE 7200 were selected for further evaluation. The CAMD – FOM approach is illustrated in Figure 3.1. The details of this approach are discussed in this chapter.

#### **3.1 Computer Aided Molecular Design**

The first four steps in Figure 3.1 constitute CAMD. The CAMD approach uses mathematical algorithms and property estimation methods to generate molecular structures from combinations of atoms or groups of atoms. Molecules were generated by combining more than 25 functional groups including the methyl, methylene, methyne, ethenyl, allenyl, alcohol, ketone, ester, ether, and fluorine groups, with only single and double bonds between groups being permitted. The maximum number of groups in a molecule was restricted to 10, because boiling points of molecules containing more than 10 groups are likely to be too high. In addition, chlorine, carboxylic acid, aldehydes, phenol, amine, amide functional groups were excluded because of environmental concerns.

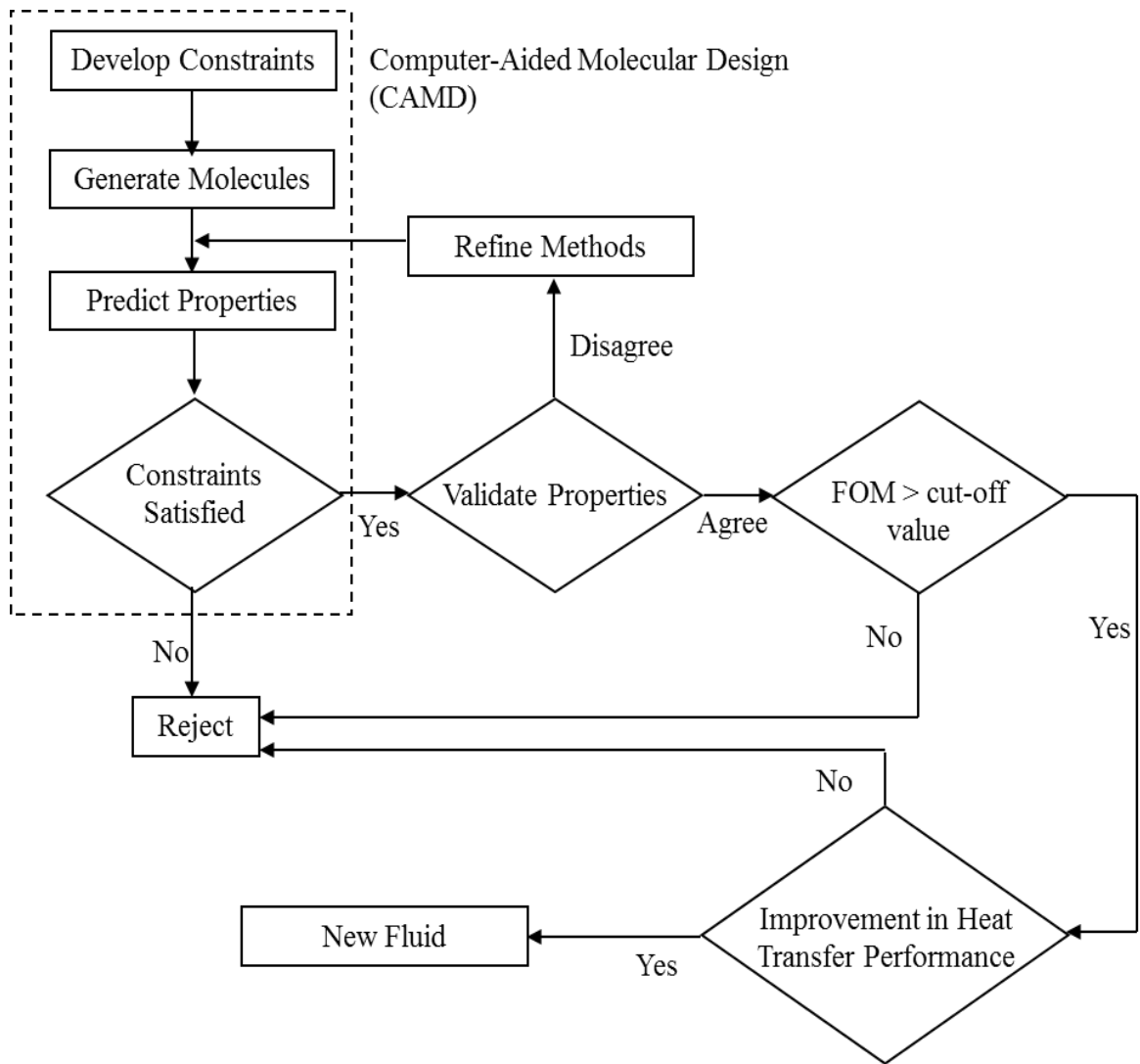


Figure 3.1: CAMD – FOM approach

All possible combinations of the specified groups were evaluated, and screened for structural feasibility based on graph theory [31]. For example, the structural feasibility of saturated compounds can be tested based on the following relation,

$$\frac{m}{2} = p + q - 1 \quad (3.1)$$

where,  $m$  is the total number of free bonds,  $p$  the number of groups and  $q$  the number of rings in the structure. The application of Equation 3.1 to determine the structural feasibility is illustrated in Table 3.1.

Table 3.1: Screening of compounds for structural feasibility

Groups	$m$	$p$	$q$	Equation 3.1	Feasibility
CH <sub>3</sub> , CH <sub>2</sub> , OH	4	3	0	$\frac{4}{2} = 3 + 0 - 1$	Yes
CH, CH <sub>2</sub>	5	2	0	$\frac{5}{2} \neq 2 + 0 - 1$	No

After this screening, the groups were then connected together into complete molecular structures. This procedure forms all pairings of bonds, checks that each bond pair is connectable (i.e., that single bonds are paired with single bonds, double bonds with double bonds, etc.), and then checks for duplicated structures. Thermophysical properties of the feasible candidate molecules were then estimated using property estimation methods such as group contribution (GC) methods, and molecules which failed to satisfy the property constraints were eliminated.

## 3.2 Fluid Property Prediction

The success of any CAMD approach depends on the availability and accuracy of property estimation methods used to predict the properties of the newly generated molecules. If uncertainties associated with the property predictions are high, then it is possible that potential candidates might be screened out. In this work, GC methods were used to predict properties of the candidate fluids.

### 3.2.1 Group Contribution Methods

The basis of GC methods is the presence of certain groupings of atoms (called functional groups) that determine most of the chemical and physical properties of organic compounds. A functional group can be defined as a unique collection of chemically bonded atoms that displays distinct set of properties [32]. Organic compounds can be systematically organized into classes (alcohols, ethers, esters, carboxylic acids, etc.) with each class characterized by a particular functional group (OH, O, COO, COOH). All alcohols, for example, contain the OH functional group that exhibits similar properties whether it is linked to CH<sub>3</sub>, CH<sub>2</sub>, or C<sub>6</sub>H<sub>5</sub> groups. Therefore, the properties of the OH group are transferable across different organic compounds. GC methods utilize this property of functional groups and further assume that properties are additive. Thus, the contribution of a group towards any property is assumed to be constant and independent of the group to which it is attached. For example, methanol (CH<sub>3</sub>OH) has two functional groups, CH<sub>3</sub> and OH. The normal boiling point of methanol can be calculated from the sum of contributions from CH<sub>3</sub> and OH groups. This assumption, while not always valid, provides an opportunity for estimating the properties of a large number of compounds

from a much smaller number of parameters that characterize the contributions of individual groups.

Group contribution methods proposed by Joback and Reid [33], Constantinou and Gani [34], Wilson and Jasperson [35], and Marrero and Gani [36] were considered for this study as they can be applied for a wide variety of compounds. These four group contribution methods were incorporated into the property prediction module of ICAS software and were used to predict properties of candidate fluids. The details of the property prediction are presented elsewhere [37].

### **3.2.2 Evaluation of Group Contribution Methods**

A wide variety of existing organic compounds including, alkanes, alkenes, alkynes, carboxylic acids, alcohols, ketones, aldehydes, ethers, esters, amides, fluorinated (F), organosilicon (Si) as well as aromatic and alicyclic compounds were selected for the evaluation of the four group contribution methods. These families of compounds were selected on the basis of availability of group contributions and their potential in heat transfer applications. Data for approximately ten compounds from each family was compiled from the DIPPR database [38] and used to evaluate the four group contribution methods for eight properties: melting point, normal boiling point, enthalpy of vaporization, surface tension, density, thermal conductivity, viscosity, and specific heat. Enthalpy of vaporization, density, and thermal conductivity were computed using the corresponding states correlations [39] with the critical properties predicted by the GC methods. This evaluation was performed not only to select the best method for each property but also in identifying properties that can be predicted with a reasonable degree of accuracy.

These four methods were critically evaluated [37] and found to provide reasonable estimates of many thermo-physical properties of interest in heat transfer applications. Average absolute deviations of about 10% were obtained for most properties, with the exception of surface tension and viscosity.

### 3.3 Constraints on Fluid Properties

New heat transfer fluids must have good thermophysical properties to obtain high heat transfer coefficients. Some of the fluid properties that are important for direct immersion phase change cooling are:

- *Thermal conductivity ( $k$ ):* Thermal conductivity has a greater influence on heat transfer coefficient than other properties. Hence, a high value of thermal conductivity is essential for efficient heat transfer.
- *Latent heat of vaporization ( $h_{fg}$ ):* A high enthalpy of vaporization is desirable for phase change cooling.
- *Boiling point ( $T_b$ ):* The International Technology Roadmap for Semiconductors [40] predicts that the maximum junction temperature has to be below 85 °C for both cost performance and high performance systems. Hence, the boiling point was constrained to be in the vicinity of 80 °C for phase change cooling.
- *Specific heat ( $c_p$ ):* Specific heat determines the thermal storage and transport capacity of the fluid. In general, a high specific heat is desirable.
- *Viscosity ( $\mu$ ):* Fluids with low viscosity require less pumping power than those with high viscosity. Hence, a low value of viscosity is desirable.



- *Electrical resistivity* ( $\rho_e$ ): Fluids for direct immersion cooling have to be dielectric. Therefore, electrical resistivity of new fluids should be comparable with those of existing coolants. However, due to lack of estimation methods for  $\rho_e$ , this property was not used as a constraint in CAMD.

Table 3.2: Properties of some existing coolants

Property	FC-72	FC-84	HFE 7100	HFE 7200	HFE 7500
$T_b$ (K)	329	353	334	349	401
$\rho$ (kg/m <sup>3</sup> )	1680	1730	1510	1420	1614
$h_{fg}$ (kJ/mol)	29.7	35	28	31.4	36.8
$k$ (W/m-K)	0.057	0.060	0.069	0.068	0.065
$c_p$ (J/mol-K)	372	427	296	322	467
$\mu$ (cP)	0.64	0.91	0.58	0.60	1.24
$\sigma$ (dynes/cm)	10	12	13.6	13.6	16.2

The properties of some existing coolants are listed in Table 3.2, and were used as the basis for developing property constraints. The four GC methods were able to predict properties (except for viscosity and surface tension) to a reasonable degree of accuracy

(with average absolute deviations less than 10%). However, applying all property constraints in the initial design phase is not practical because too few candidates will be selected in that case. Hence, the following constraints were set for screening thousands of candidate fluids generated using the CAMD approach:

- $320 \text{ K} \leq T_b \leq 370 \text{ K}$
- $k \geq 0.09 \text{ W/m-K}$
- $h_{fg} \geq 35 \text{ kJ/mol}$

### 3.4 Figure of Merit Analysis

The candidates that satisfied the above constraints were further refined using FOM analysis. A FOM represents the relationship among thermo-physical properties of the fluid, and these relationships were derived from existing heat transfer correlations by grouping all the fluid thermophysical property dependent terms. FOMs based on the Rohsenow correlation for nucleate pool boiling [41], the Lazarek and Black correlation for flow boiling in vertical channels [42], and the Tran correlation for flow boiling in horizontal channels [43], were chosen for this study as these are the most likely regimes/geometries of interest in direct immersion cooling. FOMs derived from these correlations are listed in Table 3.3. These FOM's are such that a higher value of FOM corresponds to better heat transfer characteristics.

FOMs were computed for candidates that satisfied the boiling point, thermal conductivity and latent heat of vaporization constraints. Candidates with FOMs that were lower than those of existing coolants (allowing for errors in property estimation methods)

were screened out. The cut-off values for FOMs were calculated using a 20% change in viscosity and 10% change in all other properties. HFE 7200 was chosen as the base fluid in this work. The FOMs for HFE 7200 and the cut-off values are presented in Table 3.4 [44]. The FOM's of some of the shortlisted candidates are shown in Table 3.5.

Table 3.3: FOM correlations

Correlation	FOM
Rohsenow	$\frac{10^3}{\left(\frac{h_{fg}}{c_p}\right)\left(\frac{c_p\mu}{k}\right)^{1.7}\left(\frac{1}{\mu h_{fg}}\sqrt{\frac{\sigma}{g(\rho_l - \rho_v)}}\right)^{0.33}}$
Lazarek and Black	$\frac{10^3 \times k}{\mu^{0.857} h_{fg}^{0.714}}$
Tran	$\frac{10^6 \times k}{(\mu h_{fg})^{0.62}} \left(\frac{\rho_v}{\rho_l}\right)^{0.607}$

Table 3.4: FOM for HFE 7200, and cut-off values for candidate fluids

<b>Correlation</b>	<b>HFE 7200</b>	<b>FOM Cut-off</b>
Rohsenow	7.20	13.72
Lazarek and Black	9.21	13.22
Tran	260.87	311.43

Table 3.5: Candidate fluids selected after FOM analysis.

Formula	Name	FOM		
		L & B	Tran	Rohsenow
C <sub>5</sub> H <sub>6</sub> F <sub>6</sub>	1,1,1,4,4,4-hexafluoro-2-methylbutane	29.34	571.77	44.26
C <sub>6</sub> H <sub>8</sub> F <sub>6</sub>	1,1,1-trifluoro-3-methyl-2-(trifluoromethyl)butane	29.22	621.78	42.03
C <sub>5</sub> H <sub>6</sub> F <sub>6</sub>	1,1,1,5,5,5-hexafluoropentane	27.53	533.93	40.74
C <sub>6</sub> H <sub>9</sub> F <sub>3</sub>	(E)-6,6,6-trifluorohex-2-ene	25.83	514.50	37.31
C <sub>6</sub> H <sub>8</sub> F <sub>6</sub>	1,1,1,5,5,5-hexafluoro-3-methylpentane	26.24	565.44	36.01
C <sub>7</sub> H <sub>11</sub> F <sub>5</sub>	2,2-difluoro-4-methyl-3-(trifluoromethyl)pentane	25.88	569.35	34.75
C <sub>6</sub> H <sub>9</sub> F <sub>5</sub>	1,1,1,5,5-pentafluorohexane	24.45	494.68	33.56
C <sub>7</sub> H <sub>11</sub> F <sub>3</sub>	4-methyl-3-(trifluoromethyl)pent-1-ene	24.20	522.44	31.67
C <sub>6</sub> H <sub>9</sub> F <sub>3</sub>	(E)-1,1,1-trifluoro-3-methylpent-2-ene	22.28	465.67	30.03
C <sub>6</sub> H <sub>9</sub> F <sub>3</sub>	6,6,6-trifluorohex-1-ene	22.46	461.31	29.55
<b>C<sub>6</sub>H<sub>11</sub>F<sub>3</sub></b>	<b>1,1,1-trifluoro-3-methylpentane</b>	<b>21.83</b>	<b>461.31</b>	<b>26.87</b>
C <sub>4</sub> H <sub>7</sub> F <sub>3</sub> O	1,1,1-trifluoro-3-methoxypropane	20.33	371.17	26.40
C <sub>7</sub> H <sub>11</sub> F <sub>3</sub>	(E)-5,5,5-trifluoro-4,4-dimethylpent-2-ene	21.13	481.22	26.04
C <sub>6</sub> H <sub>8</sub> F <sub>6</sub>	1,1,1,4,4,4-hexafluoro-2,2-dimethylbutane	20.98	494.18	25.17
C <sub>6</sub> H <sub>9</sub> F <sub>3</sub>	5,5,5-trifluoro-2-methylpent-1-ene	19.94	425.40	24.46
C <sub>6</sub> H <sub>9</sub> F <sub>5</sub> O	2-(2,2-difluoropropoxy)-1,1,1-trifluoropropane	19.65	435.16	23.18
C <sub>5</sub> H <sub>9</sub> F <sub>3</sub> O	1,1,1-trifluoro-3-methoxybutane	19.22	391.49	22.97
<b>C<sub>5</sub>H<sub>6</sub>F<sub>6</sub>O</b>	<b>1,1,1-trifluoro-3-(2,2,2-trifluoroethoxy)propane</b>	<b>19.34</b>	<b>419.21</b>	<b>22.97</b>
C <sub>4</sub> H <sub>12</sub> OSi	ethoxydimethylsilane	18.81	381.05	22.86
C <sub>6</sub> H <sub>11</sub> F <sub>3</sub>	1,1,1-trifluorohexane	19.45	417.06	22.63
<b>C<sub>4</sub>H<sub>5</sub>F<sub>3</sub>O</b>	<b>1,1,1-trifluorobutan-2-one</b>	<b>16.70</b>	<b>328.77</b>	<b>22.45</b>
C <sub>7</sub> H <sub>11</sub> F <sub>5</sub>	2,2-difluoro-3-methyl-3-(trifluoromethyl)pentane	18.80	455.17	21.21
C <sub>4</sub> H <sub>5</sub> F <sub>3</sub> O <sub>2</sub>	methyl 3,3,3-trifluoropropanoate	15.83	317.06	20.95
C <sub>7</sub> H <sub>14</sub> F <sub>2</sub>	3,3-difluoroheptane	18.01	389.37	19.91
C <sub>7</sub> H <sub>11</sub> F <sub>3</sub>	3-methyl-3-(trifluoromethyl)pent-1-ene	17.38	414.27	18.97
C <sub>7</sub> H <sub>13</sub> F <sub>3</sub>	1,1,1-trifluoro-2,3,3-trimethylbutane	16.98	406.64	18.08
C <sub>5</sub> H <sub>9</sub> F <sub>3</sub> O	3-ethoxy-1,1,1-trifluoropropane	16.30	345.26	17.51
C <sub>5</sub> H <sub>12</sub> O	1-methoxybutane	15.86	300.50	16.82
C <sub>7</sub> H <sub>11</sub> F <sub>3</sub>	4,4,4-trifluoro-2,3,3-trimethylbut-1-ene	16.10	394.35	16.74
C <sub>7</sub> H <sub>13</sub> F <sub>3</sub>	1,1,1-trifluoro-2,2-dimethylpentane	15.10	385.54	14.57
C <sub>7</sub> H <sub>13</sub> F <sub>3</sub>	1,1,1-trifluoro-2,3-dimethylpentane	14.73	368.63	14.20
<b>C<sub>4</sub>H<sub>12</sub>O<sub>2</sub>Si</b>	<b>dimethoxydimethylsilane</b>	<b>11.48</b>	<b>274.83</b>	<b>10.83</b>

### 3.5 New Heat Transfer Fluids

Among the 32 compounds listed in Table 3.5, four fluids were selected for further evaluation.

- $C_4H_5F_3O$  and  $C_4H_{12}O_2Si$  were available commercially
- $C_6H_{11}F_3$  and  $C_5H_6F_6O$  were selected for custom synthesis

A surrogate for  $C_5H_5F_6O$ ,  $C_4H_4F_6O$  was available commercially and its thermo-physical properties are very close to those of  $C_5H_6F_6O$ . If heat transfer experiments with  $C_4H_4F_6O$  show improvement over HFE 7200, it becomes highly likely that  $C_5H_6F_6O$  will also have superior heat transfer properties. Hence,  $C_4H_4F_6O$  was selected for further evaluation.

In addition to these fluids, methanol and ethoxybutane were selected as candidates for designing mixture formulations with HFE 7200 based on knowledge based approach. Methanol is often used as an additive in heat transfer fluids [45] and it has been shown to be miscible with HFE 7200 [46]. Moreover, methanol has a high thermal conductivity, low viscosity, high heat of vaporization, and a low boiling point. Therefore, addition of methanol to HFE 7200 is expected to enhance the heat transfer performance.

Ethoxybutane was selected because of its structural similarity with HFE 7200 and its low dielectric constant which is especially relevant for direct immersion electronic cooling applications. Thermophysical properties of ethoxybutane were also found to be superior to those of HFE 7200. In addition, ethoxybutane was expected to be completely soluble in HFE 7200 because of the structural similarities of the two molecules and solubility parameters that were very close.

### 3.6 Summary

In this chapter, the CAMD approach used to design new heat transfer fluids is discussed. The four group contribution methods used to predict fluid properties and their evaluation procedure is briefly discussed. The constraints imposed on the candidate fluids and the basis for selecting these constraints is presented. The fluids that satisfied these constraints were further screened using FOM analysis. The main conclusions from this study are:

- 1) The group contribution methods provide reasonable estimates of several fluid properties except surface tension and viscosity. Hence, these two properties were not selected as constraints to screen candidate fluids.
- 2) The fluids generated using CAMD approach were screened based on the constraints imposed on boiling point, thermal conductivity and latent heat of vaporization. These properties were chosen as they could be predicted accurately and also due to their importance in phase change heat transfer.
- 3) FOM analysis was used to screen candidate fluids that satisfied the above constraints. FOM's were derived from existing heat transfer correlations by grouping all fluid property dependent terms. Taking into account the errors in property estimation methods, the cut-off values for FOM were chosen appropriately.
- 4) After the FOM analysis, four new fluids ( $C_4H_5F_3O$ ,  $C_6H_{11}F_3$ ,  $C_4H_4F_6O$  and  $C_4H_{12}O_2Si$ ) were identified for further evaluation. Two existing fluids (methanol and Ethoxybutane) were also selected using the knowledge based approach.

## **CHAPTER 4**

### **FLUID PROPERTIES**

The thermophysical properties of the new heat transfer fluids identified using CAMD – FOM approach were experimentally measured and validated with the theoretical predictions. The wetting characteristics of new fluids were analyzed through contact angle measurements. The details of these measurements are discussed in this chapter.

#### **4.1 Thermophysical Properties Measurement**

The chemicals used in this study were purchased from various sources and the details are shown in Table 4.1. The purity of the chemical is specified in mole percentage, and signifies what proportion of a sample from the container is composed of the pure fluid.  $C_6H_{11}F_3$  was synthesized by Dr. Pramod Warriar from Prof. Aryn Teja's group in the School of Chemical and Biomolecular Engineering at Georgia Tech, in collaboration with Prof. Stefan France in the School of Chemistry and Biochemistry at Georgia Tech.

Density, thermal conductivity and viscosity of the pure fluids were measured using a glass pycnometer [47], transient hot wire cell method [48], and a viscometer respectively. Uncertainties in the property measurements are  $\pm 1 \text{ kg/m}^3$ , 2%, and 0.16% for density, thermal conductivity, and viscosity respectively. Thermophysical properties measured experimentally (Exp) and GC estimates for these properties are shown in Table 4.2.



Table 4.1: Supplier information for heat transfer fluids

Name	Formula	Purity (mol. %)	Supplier
HFE 7200	C <sub>6</sub> H <sub>5</sub> F <sub>9</sub> O	98	3M Company, MN
Dimethoxydimethylsilane	C <sub>4</sub> H <sub>12</sub> O <sub>2</sub> Si	99.5	Sigma Aldrich, MO
1-ethoxybutane	C <sub>6</sub> H <sub>14</sub> O	98	Sigma Aldrich, MO
1,1,1-trifluoro-2-butanone	C <sub>4</sub> H <sub>5</sub> F <sub>3</sub> O	95	SynQuest Labs, FL
Bis(2,2,2-trifluoroethyl)ether	C <sub>4</sub> H <sub>4</sub> F <sub>6</sub> O	99	SynQuest Labs, FL
Methanol	CH <sub>3</sub> OH	99.9	Fisher Scientific, PA

Table 4.2: Thermophysical property measurements of new fluids.

Fluid	$\rho$ (g/cc)		$\mu$ (cP)		$k$ (W/m-K)	
	Exp	GC	Exp	GC	Exp	GC
HFE 7200	1.417	1.627	0.607	0.210	0.066	0.081
C <sub>6</sub> H <sub>11</sub> F <sub>3</sub>	0.973	0.896	0.350	0.250	0.089	0.106
C <sub>4</sub> H <sub>4</sub> F <sub>6</sub> O	1.396	1.312	0.560	0.270	0.083	0.092
C <sub>4</sub> H <sub>5</sub> F <sub>3</sub> O	1.137	1.016	0.367	0.320	0.091	0.112
C <sub>4</sub> H <sub>12</sub> SiO <sub>2</sub>	0.857	0.862	0.341	0.452	0.115	0.126

From this table, it can be observed that GC estimates are in reasonable agreement with the measured data, except for the case of viscosity. This, therefore, validates our decision to not use viscosity as a constraint to screen candidates.

Table 4.3: Properties of heat transfer fluids considered for experiments

Property	C <sub>6</sub> H <sub>11</sub> F <sub>3</sub>	C <sub>4</sub> H <sub>4</sub> F <sub>6</sub> O	C <sub>4</sub> H <sub>5</sub> F <sub>3</sub> O	C <sub>4</sub> H <sub>12</sub> O <sub>2</sub> Si	CH <sub>3</sub> OH	C <sub>6</sub> H <sub>14</sub> O	HFE 7200
T <sub>b</sub> (C)	67	62	66	81	65	92	76
ρ <sub>l</sub> (kg/m <sup>3</sup> )	973	1404	1137	857	792	743	1420
h <sub>fg</sub> (kJ/kg)	192	138	226	288	1100	307	119
k (W/m-K)	0.089	0.083	0.091	0.115	0.2	0.126	0.069
c <sub>p</sub> (J/kg-K)	1615	1252	1489	1814	2484	1549	1220
μ (kg/m-s)	0.00035	0.00056	0.00037	0.00034	0.00055	0.00039	0.0063
σ (N/m)	0.0148	0.018	0.0246	0.0218	0.0218	0.0202	0.0136

## 4.2 Contact Angle

Contact angle plays an important role in boiling heat transfer [49] and it can affect the mechanism of boiling from plain or enhanced surfaces. The surface wetting characteristics of the new fluids were investigated via measurements of the contact angle using a Goniometer (Ramehart Model 250). The contact angle measurement system is shown in Figure 4.1.

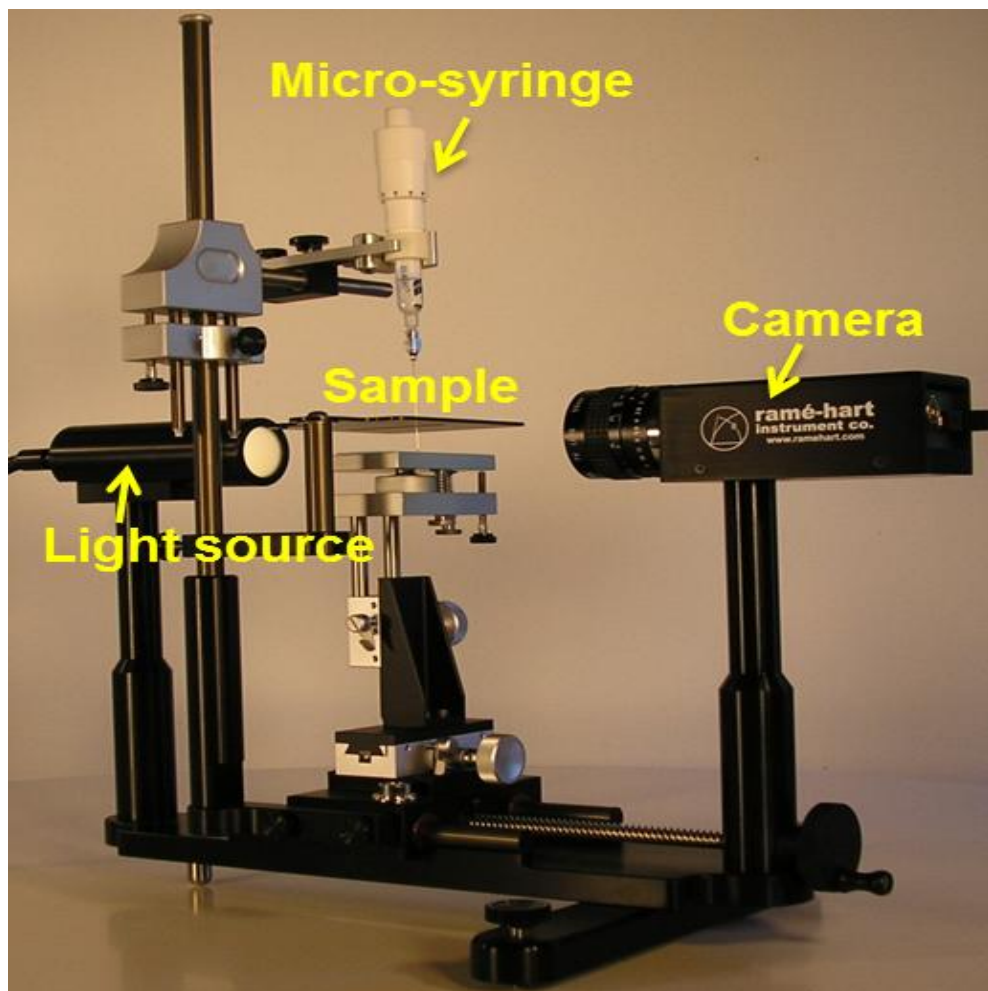


Figure 4.1: Contact angle measurement system [50]

The Goniometer consists of a fiber optic light source, 3-axis specimen stage with leveling, micro-syringe and a high speed F4 series digital camera. DROPimage Advanced Software was used to analyze the measurements. First, the test chip was mounted on the stage and it was leveled using the thumbscrews located underneath the stage. The stage is set to be level when the tilt reading is zero in the software. The micro-syringe was filled with the test liquid and a 10  $\mu$ l drop was created at the tip of the needle by twisting the micro-syringe. The micro-syringe was slowly lowered using the thumbscrews on the micro-syringe fixture until the drop came in contact with the chip surface. Once the drop touched the surface, the needle was slowly raised so that it released and created a drop on the chip surface.

The entire process was captured using the high speed camera. The instantaneous shapes of the dispensed drop of different fluids on bare surface are shown in Figures 4.2 – 4.4. Since all the fluids are volatile, it is difficult to accurately measure the static contact angle. These images were taken at the instant when the drop was dispensed onto the chip surface. The contact angle of water on the same surface is shown in Figure 4.5 for comparison. Water is relatively non-volatile when compared to these fluids and hence the static contact angle could be measured accurately ( $\pm 0.1^\circ$ ). These images show that the new fluids wet the bare SiO<sub>2</sub> surface to approximately the same extent as HFE 7200. The static contact angle for these highly volatile fluids can be measured accurately if these measurements are performed in a vacuum chamber.



Figure 4.2: Instantaneous droplet shape of HFE 7200 on a plain surface



Figure 4.3: Instantaneous droplet shape of C<sub>6</sub>H<sub>11</sub>F<sub>3</sub> on a plain surface



Figure 4.4: Instantaneous droplet shape of C<sub>4</sub>H<sub>4</sub>F<sub>6</sub>O on a plain surface



Figure 4.5: Instantaneous droplet shape of water on a plain surface

### 4.3 Vapor Liquid Equilibrium Curves

Difficulties in custom synthesis and high cost of some of the newly identified coolants prohibited evaluation of the heat transfer characteristics of pure fluids. For example, 100 grams of  $C_6H_{11}F_3$  would cost \$4,995 (quote from SynQuest Laboratories Inc., FL). Therefore, heat transfer experiments were performed for mixture formulations of newly identified fluids with existing heat transfer fluid, HFE 7200. Properties of the mixture were estimated using mass fraction weighted average of the pure component properties.

Vapor liquid equilibria (VLE) play an important role in boiling heat transfer of mixtures as the preferential evaporation of the low boiling component can have detrimental effects on heat transfer performance. VLE of binary mixtures were evaluated using regular solution theory [51]. Due to significant difference in polarities, VLE of HFE 7200 - methanol mixture were evaluated using COSMO-RS [52]. The VLE curves are shown in Figures 4.6 - 4.11. The curves in red and blue color represent the dew point and bubble point curves respectively. The bubble point is the temperature at which a liquid begins to vaporize. The dew point is the temperature at which a saturated vapor

begins to condense. The locus of the bubble point and dew point temperatures for different mixture concentrations gives the bubble point and dew point curves. The difference between the dew point and the bubble point temperatures is called the temperature glide. The smaller the temperature difference, the less loss of heat transfer due to concentration differences. If the temperature glide at a particular concentration is zero, then the mixture is said to be azeotropic at that concentration. An azeotropic mixture behaves like a pure fluid as the concentration of the liquid and vapor phases are equal.

It can be observed that the temperature glide is very small for mixtures of new fluids (except methanol) with HFE 7200 for low mole fractions ( $< \sim 0.3$ ) of the first component, and they can be considered as azeotropes at these concentrations. As pool boiling experiments were performed at low concentrations of the new fluids, detrimental effects due to preferential evaporation are likely to be insignificant.

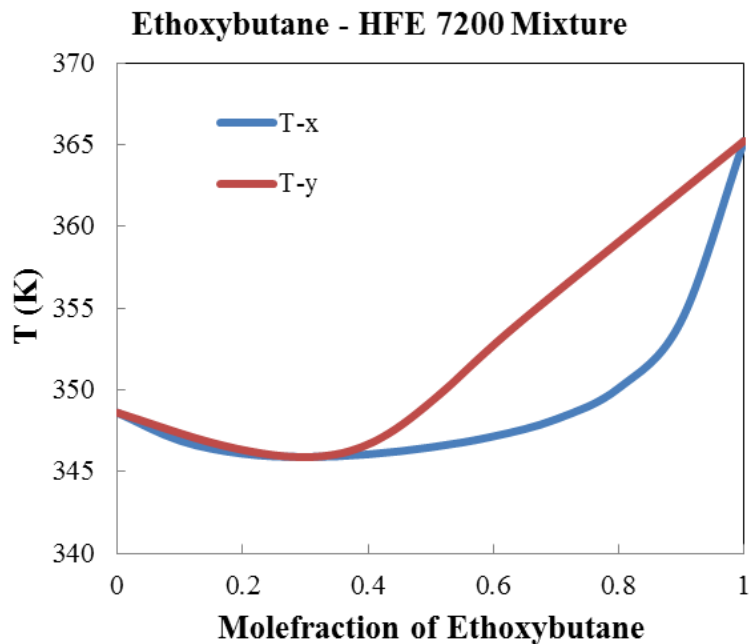


Figure 4.6: Vapor liquid equilibrium curve for mixture of HFE 7200 – ethoxybutane

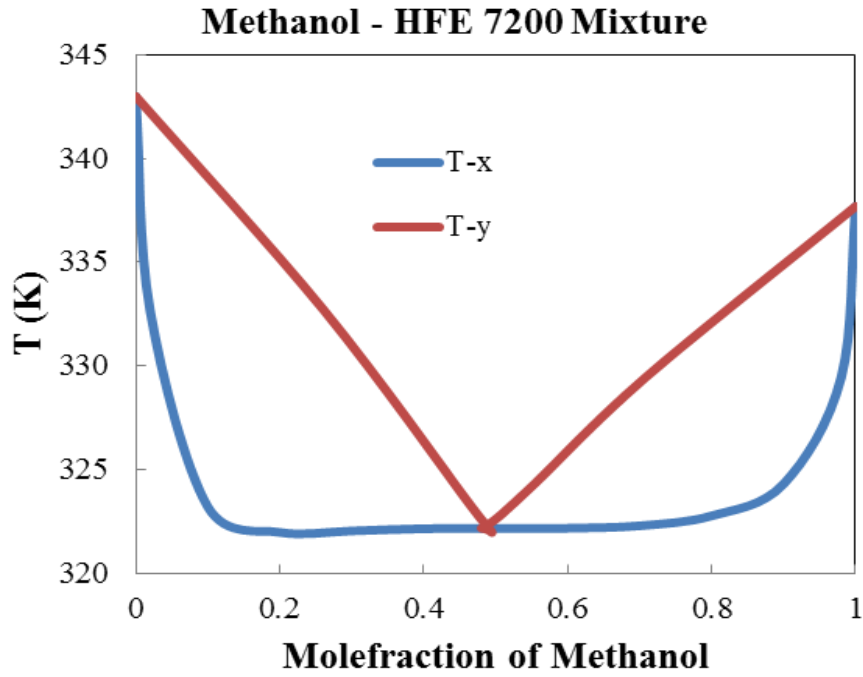


Figure 4.7: Vapor liquid equilibrium curve for mixture of HFE 7200 – methanol

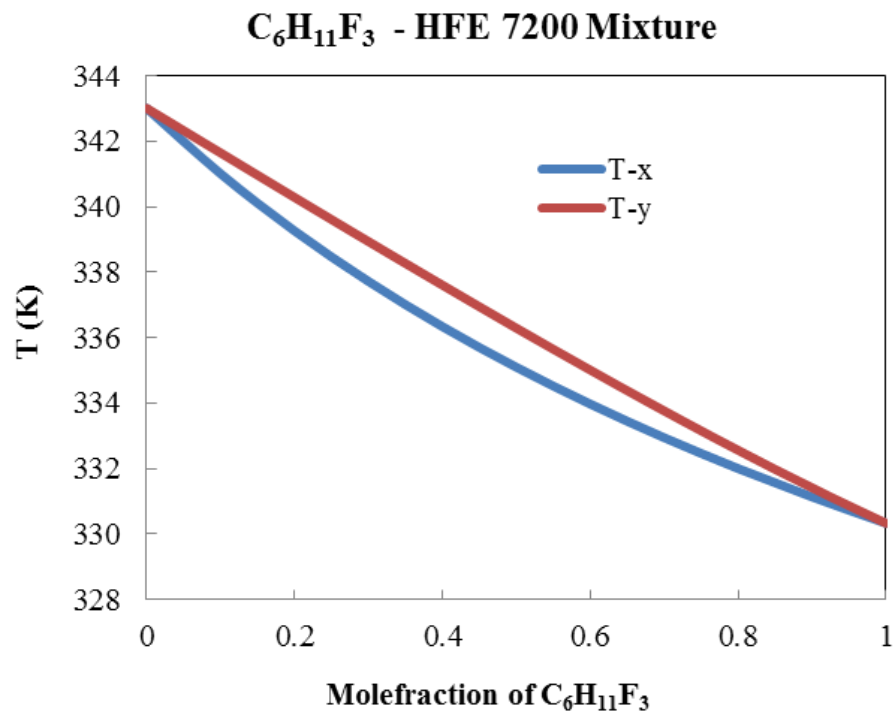


Figure 4.8: Vapor liquid equilibrium curve for mixture of HFE 7200 – C<sub>6</sub>H<sub>11</sub>F<sub>3</sub>



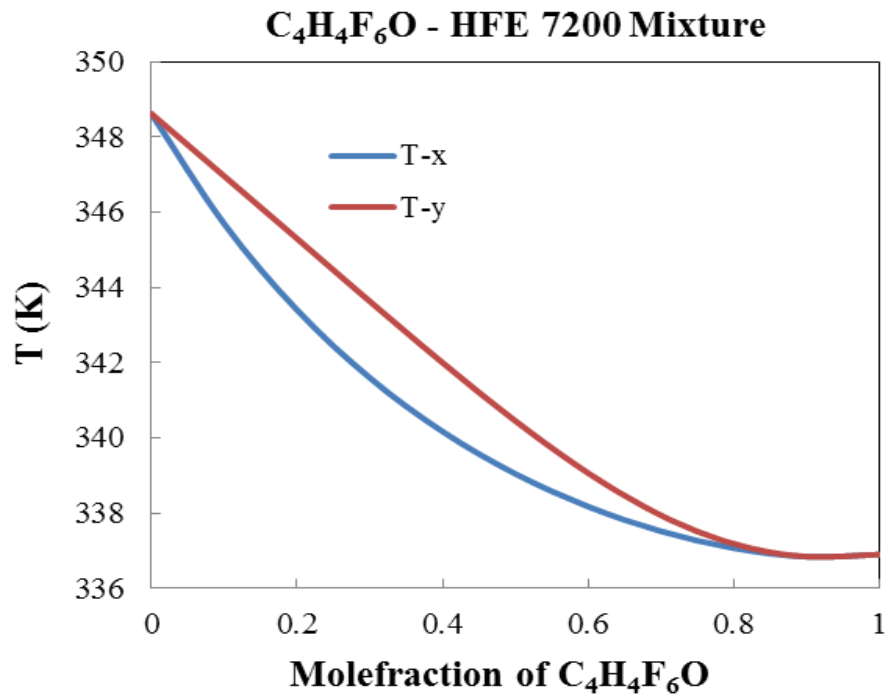


Figure 4.9: Vapor liquid equilibrium curve for mixture of HFE 7200 – C<sub>4</sub>H<sub>4</sub>F<sub>6</sub>O

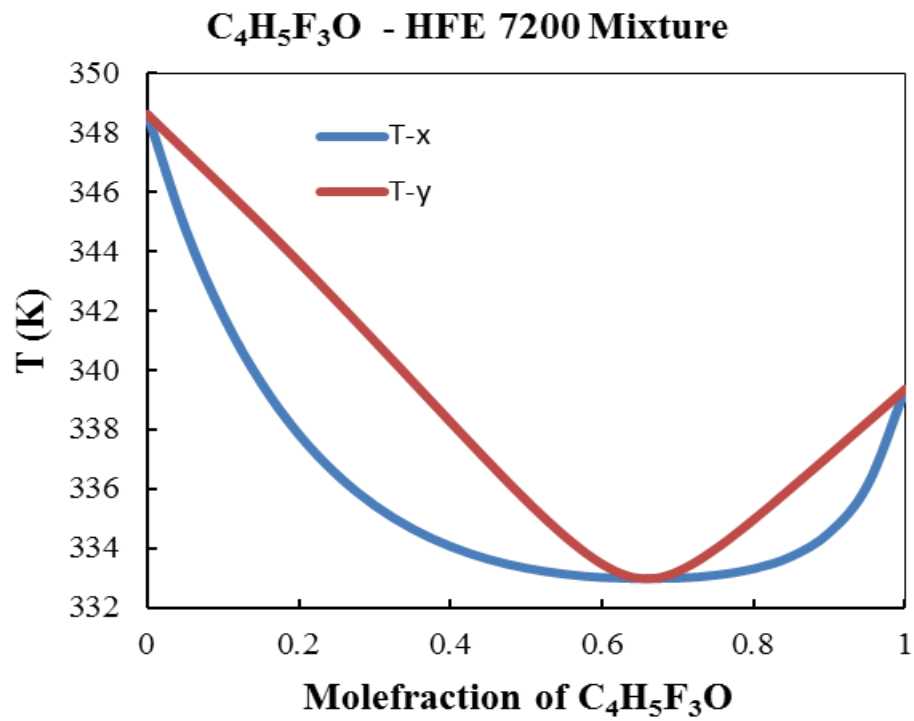


Figure 4.10: Vapor liquid equilibrium curve for mixture of HFE 7200 – C<sub>4</sub>H<sub>5</sub>F<sub>3</sub>O

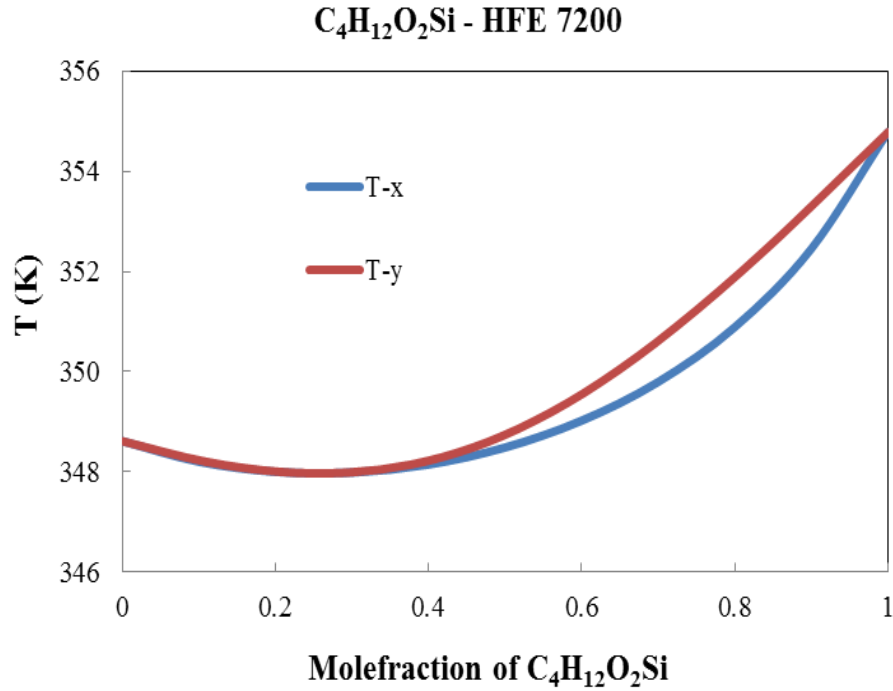


Figure 4.11: Vapor liquid equilibrium curve for mixture of HFE 7200 – C<sub>4</sub>H<sub>12</sub>O<sub>2</sub>Si

For the heat transfer experiments, the fluid mixture concentrations were chosen based on two criteria: a) the availability of the new fluid, and b) ability to form an azeotropic mixture with the available quantity. Pool boiling of HFE 7200 – C<sub>6</sub>H<sub>11</sub>F<sub>3</sub> mixture was restricted to 7 wt.% as C<sub>6</sub>H<sub>11</sub>F<sub>3</sub> could not be synthesized in large quantities to make higher mixture concentrations.

#### 4.4 Summary

Density, thermal conductivity and viscosity of selected candidate fluids were experimentally measured and validated with the GC estimates for these properties. The details of this validation are discussed in this chapter. The wetting characteristics of new fluids were analyzed through contact angle measurements and these results are presented.

The vapor liquid equilibrium curves for mixtures of new fluids with HFE 7200 are presented in this chapter. The important observations from this study are:

1) The GC estimates were in reasonable agreement with the measured data, except for viscosity. This justifies our decision to not screen candidate fluids using viscosity as a constraint.

2) All the new fluids are very volatile and hence it was impossible to accurately measure the static contact angle. However, high speed visualization shows that these new fluids are highly wetting and wet the surface to approximately the same extent as HFE 7200.

3) From the VLE curves, it was observed that the temperature glide was very small for mixtures of new fluids (except methanol) with HFE 7200 for low mole fractions ( $< \sim 0.3$ ) of the first component. As most of the heat transfer experiments were performed using low mixture concentrations, preferential evaporation of more volatile component at the heater surface is assumed to be insignificant.

## CHAPTER 5

### POOL BOILING EXPERIMENTS

Pool boiling experiments were performed to investigate the heat transfer performance of the HFE 7200 – new fluid mixtures at atmospheric pressure. Various flip-chip packaged Silicon (Si) thermal test chips with  $10 \times 10 \text{ mm}^2$  boiling surface were utilized for the experiments. The details of the experimental setup, test chip fabrication process and pool boiling results for new fluid mixtures are discussed in this chapter.

#### 5.1 Experimental Setup

Pool boiling experimental setup designed by Im [53] was used for the experiments. The schematic of the experimental setup is shown in Figure 5.1. The experimental setup consists of a transparent jacketed glass beaker. The jacketed beaker has an inner chamber that contains the test fluid and an outer chamber, with a closed flow loop around the perimeter of the inner chamber. The temperature of the test fluid inside the beaker was controlled by circulating water from a constant temperature bath (Lab-Companion, model: RW-1025G) around the perimeter of the jacketed beaker. The jacketed beaker was mechanically fitted to a Teflon block and a glass lid using an O – ring and a clamp. The test chip package was mounted on this Teflon block having a square recess at its center, and this is shown in Figure 5.2. To reduce heat loss from the bottom of the test chip, vacuum conditions were created on the back side using a vacuum pump (GAST, model: DOA-P704-AA). The bottom of the Teflon block was heated using a plate heater so that a non-powered test chip reads the saturation/bubble point temperature of the test fluid.

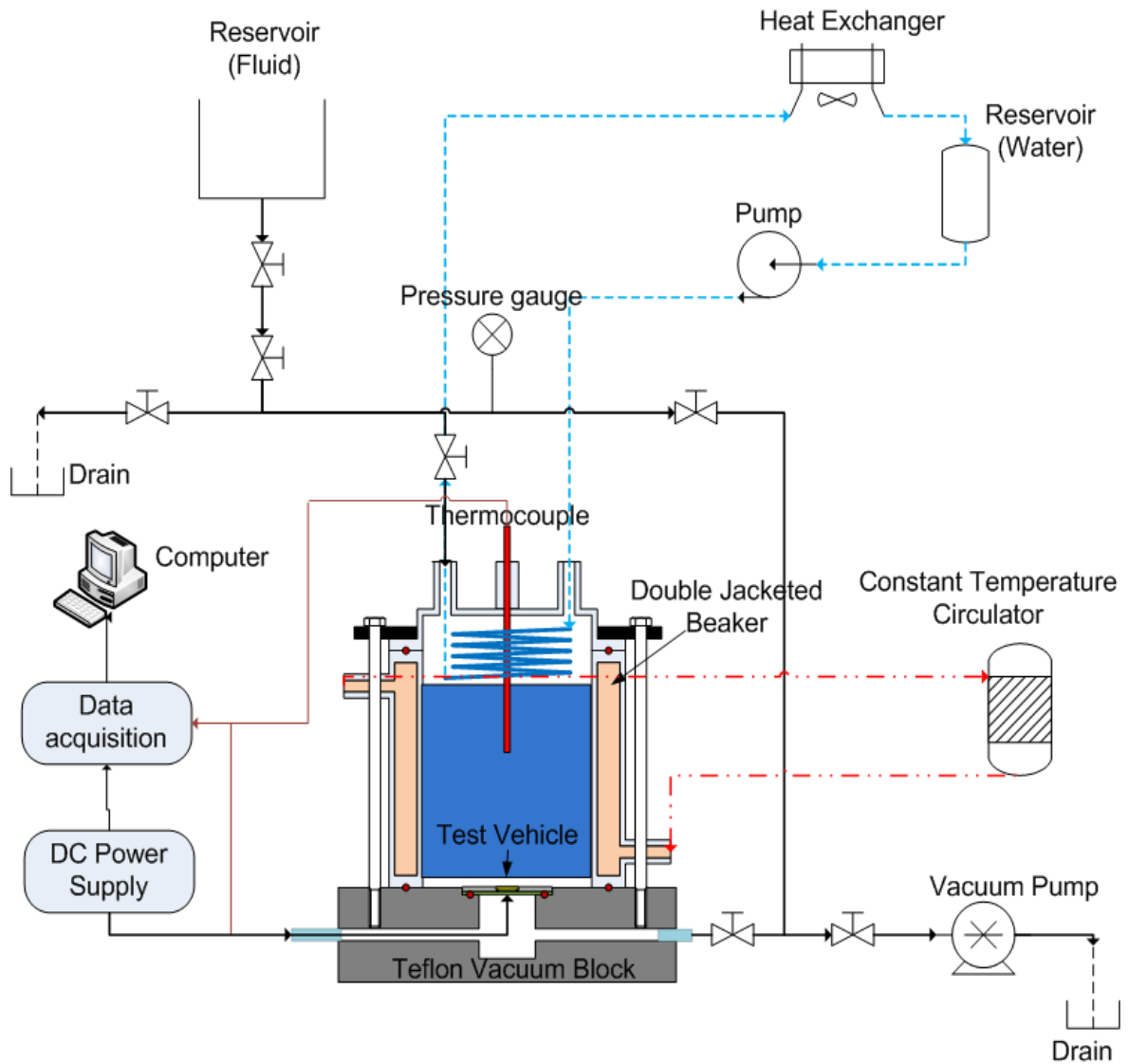


Figure 5.1: Schematic of pool boiling experimental setup

A water cooled condenser coil located in the top portion of the glass chamber was used to condense the vapor generated during the boiling process. A peristaltic pump (Cole-Parmer, model:7518-00) was used to circulate water in the condenser loop. The hot water leaving the condenser was cooled externally using a liquid-to-air heat exchanger. A T-type thermocouple (Omega<sup>TM</sup> TMQSS-062G-6) immersed in the liquid bath was used to monitor the temperature of the test fluid. The pressure inside the inner glass chamber

was monitored using a pressure gauge (Robinair, model:11692). A vent line at the top of the chamber ensures that the pressure inside the glass chamber is atmospheric during boiling. Power to the test chip was supplied using an Agilent E3645A DC power supply (0-60V, 0-1.3A). National Instruments LabVIEW™ software was used to control the power supply and the data acquisition system.

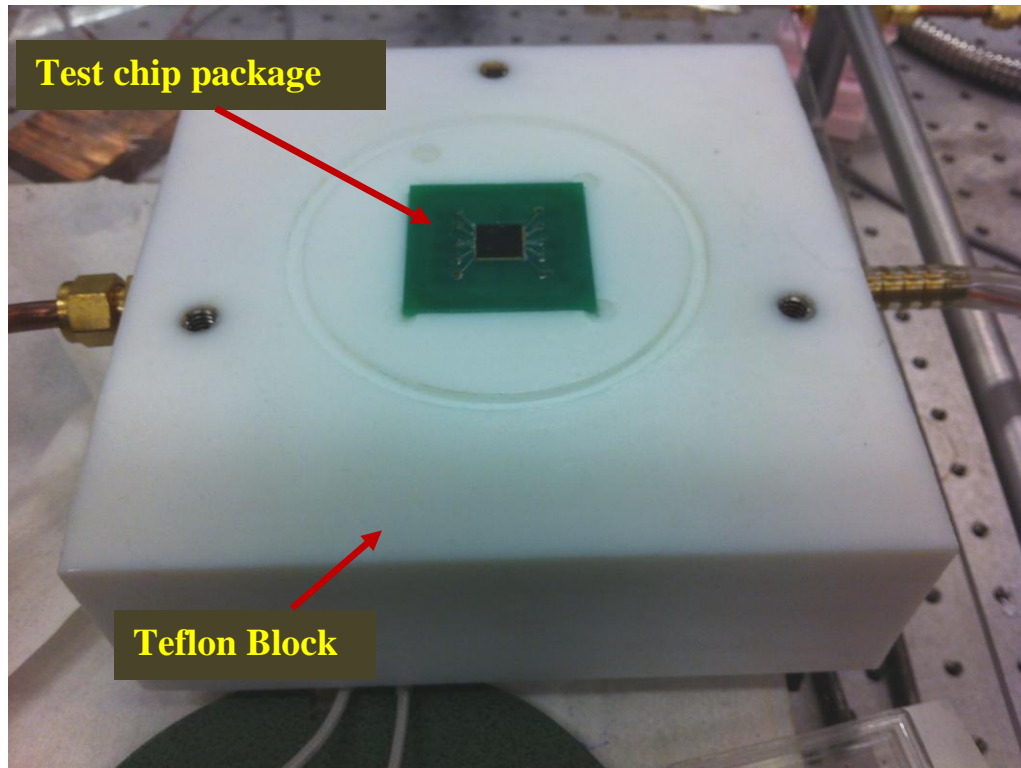


Figure 5.2: Test chip package mounted on the Teflon block

## 5.2 Test Chip Fabrication

The thermal test chip (width – 10 mm, length – 10 mm, thickness – 0.5 mm) consists of a Platinum (Pt) Resistance Temperature Detector (RTD) patterned on one side of a Si substrate using standard MEMS processes. The Pt RTD was used to provide a

uniform and known heat flux to the chip surface, while simultaneously providing average surface temperature measurement. Pt was selected as the RTD material because of its high output (temperature coefficient of  $0.00385\Omega/^\circ\text{C}$ ), thermal/chemical durability, excellent linearity, and ease of fabrication.

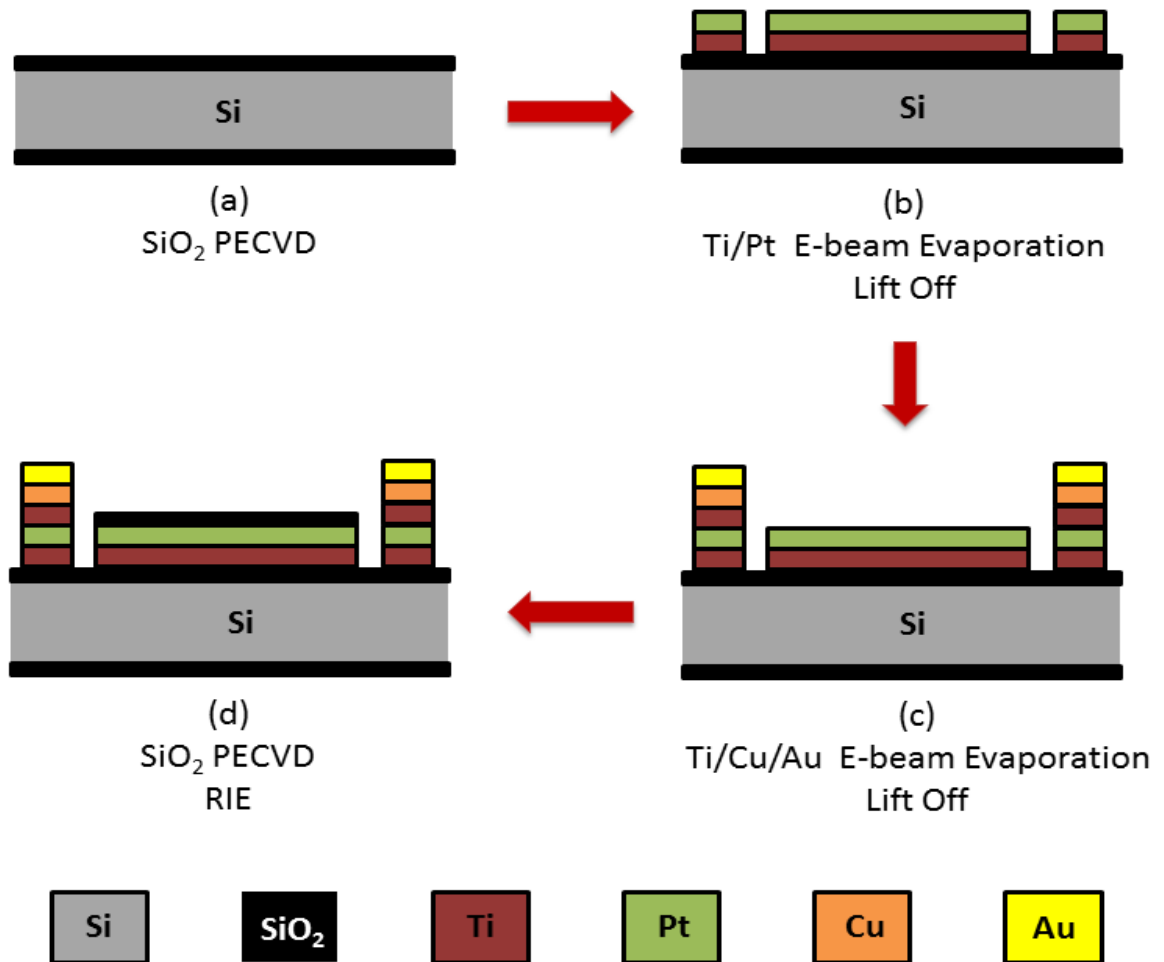


Figure 5.3: Test chip fabrication process

As shown in Figure 5.3(a), the Si wafer was first coated with dielectric  $\text{SiO}_2$  layer ( $0.4\ \mu\text{m}$  thick) on both sides by Plasma Enhanced Chemical Vapor Deposition (PECVD). Next, Titanium (Ti) and Pt layers of thickness  $0.05\ \mu\text{m}$  and  $0.4\ \mu\text{m}$  respectively were

deposited by E-beam evaporation. Ti acts as an adhesion layer and Pt layer serves as the RTD. Subsequently, the Ti and Pt layers were patterned by lift off process and this is shown in Figure 5.3(b). The Pt RTD was electrically connected to the PCB via contact pads. To form the contact pads, first Ti, Copper (Cu) and Gold (Au) layers of thickness 0.05  $\mu\text{m}$ , 0.4  $\mu\text{m}$  and 0.2  $\mu\text{m}$  respectively, were deposited by E-beam evaporation process as shown in Figure 5.3(c) and patterned by lift off process. These three layers act as the adhesion layer, solder wetting layer and oxidation inhibiting layer respectively. Then a layer of  $\text{SiO}_2$  (0.4  $\mu\text{m}$  thick) was deposited to electrically passivate the RTD and was selectively etched by Reactive Ion Etching (RIE) as shown in Figure 5.3(d). The Pt RTD on the underside of the test substrate is shown in Figure 5.4. The test chip was attached to a Printed Circuit Board (PCB) by flip-chip bonding. The gap between the test chip and the PCB was filled with an underfill material to reduce unwanted boiling from the edges of the chip.

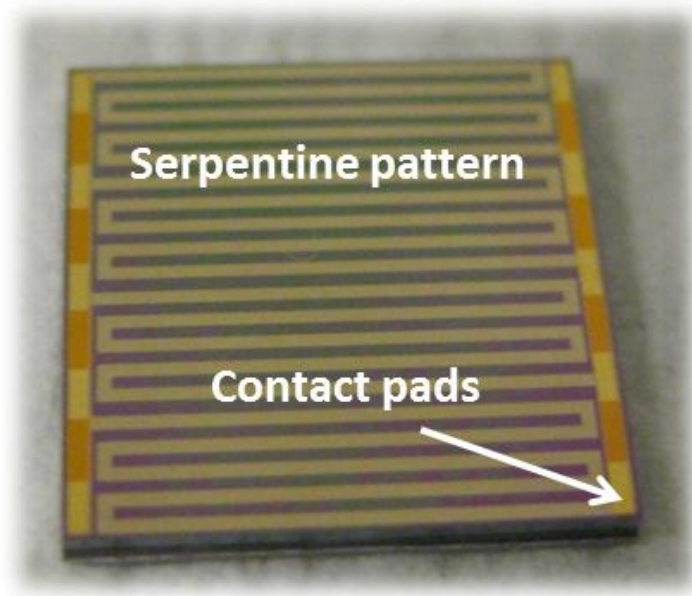


Figure 5.4: Platinum RTD fabricated on the backside of the chip



The other side of the test chip was used to fabricate Cu nanowire and CuO hybrid nanostructured surfaces. Cu nanowires were fabricated by electrochemically assisted template growth of copper. Commercial AAO (Anodisc 25, Whatman, 200 nm pore, 60  $\mu\text{m}$  thick, 25 mm diameter, porosity of 0.5) was used as the template to fabricate nanowires. First Ti, Cu, and Au films of thicknesses 50, 400, and 200 nm respectively were deposited on one side of the AAO template by E-beam evaporation, to make a seed layer for electrochemical deposition. This AAO was mounted on copper plate using polyimide tape, to give electrical interconnection mechanically and was then immersed in DI water. It was then subjected to sonication for 5 minutes to eject bubbles from electrochemical deposition.

Before starting the actual electrochemical deposition, dummy electrochemical deposition was conducted in an electrolytic bath consisting of sulfuric acid 120 ml/l, copper sulfate 90 g/l, copper carrier 12 ml/l, and copper additive 6 ml/l, for 30 minutes to stabilize the electrolyte and the electrode. The electrochemical depositions were conducted at 2.5 mA DC. The AAO template having copper nanowires was detached from the copper plate after electrochemical deposition. It was then attached to the backside of test chip using Ag epoxy, ablebond 2000T. Finally, free standing copper nanowires were obtained by dissolving the AAO template in 5 wt.% NaOH solution for 5 minutes. The Scanning Electron Microscope (SEM) images of different nanostructured surfaces used for the experiments are shown in Figures 5.5 – 5.8. Two hybrid micro-nanostructured surfaces (surface\_1 and surface\_2), shown in Figures 5.7 and 5.8, developed by Im [53] was also used for the pool boiling experiments. More details on the hybrid surface fabrication and packaging are available in the literature [53].

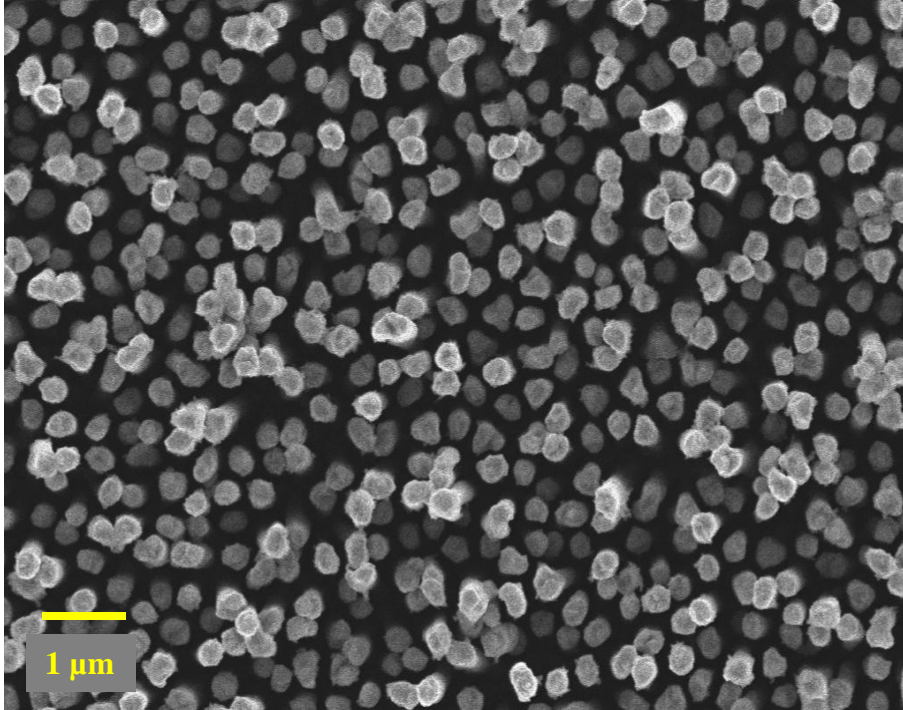


Figure 5.5: SEM image of Cu nanowire array (height of nanowires - 4 μm)

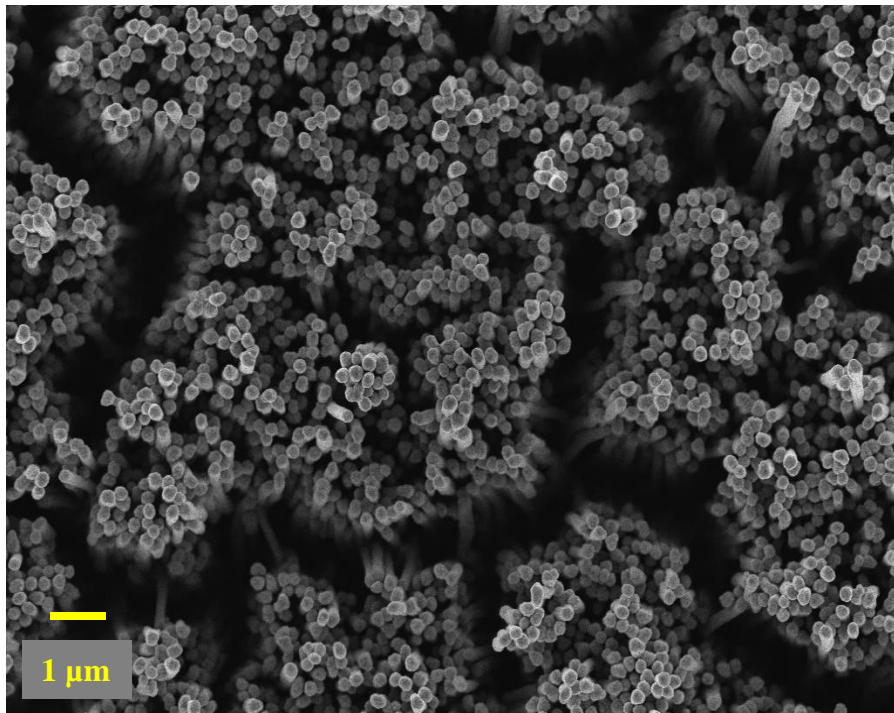


Figure 5.6: SEM image of Cu nanowire array (height of nanowires - 20 μm)

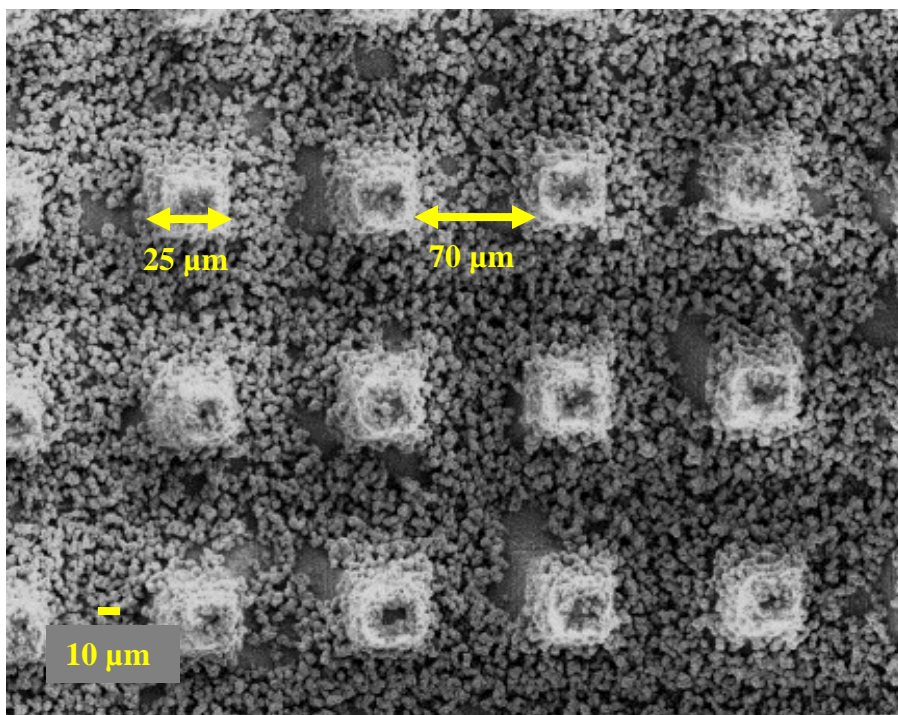


Figure 5.7: SEM image of CuO hybrid micro-nanostructured surface\_1

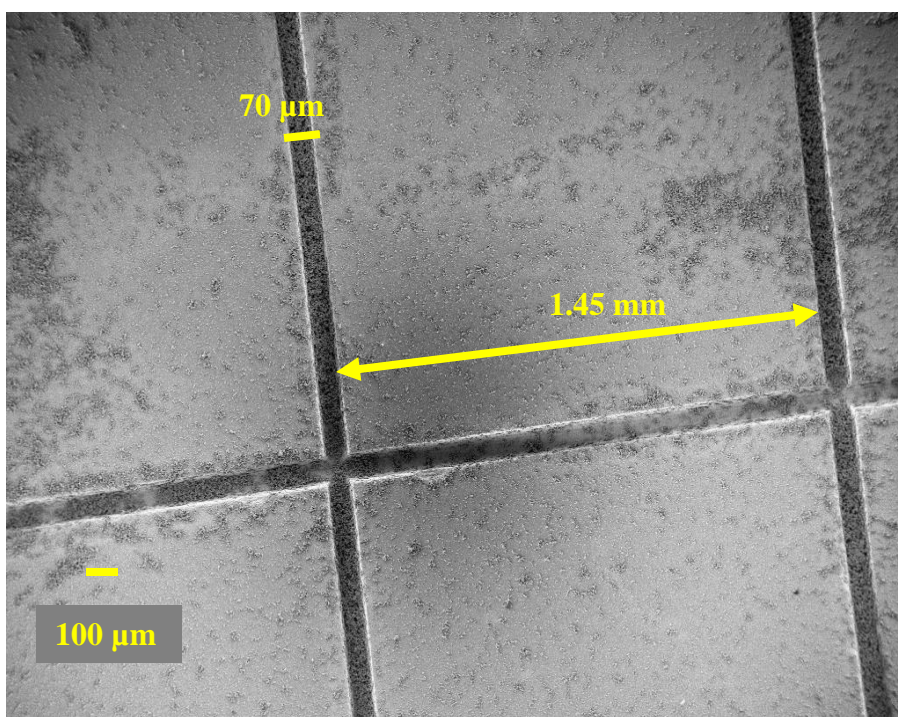


Figure 5.8: SEM image of CuO hybrid micro-nanostructured surface\_2

The Pt RTD provides simultaneous heating and temperature sensing capabilities. Since the resistance of the heater is a function of temperature, the chip surface temperature can be calculated by measuring the resistance. To determine this temperature – resistance relationship, the Pt RTD was calibrated using a hot plate heater. A T – type thermocouple was attached to the thermal test chip to measure the chip surface temperature. The test chip was placed on the hot plate heater and the heater was shielded from the surroundings by enclosing it in a chamber. The hot plate heater was set to different values of temperature (25 °C, 56 °C, 85 °C and 114 °C) and the chip surface temperature and resistance of the Pt RTD were recorded for each of these runs. A linear curve was fit through the data to obtain a relation between the surface temperature and the resistance. All the test chips used for the experiments were calibrated by the above method. A sample calibration curve is shown in Figure 5.9.

Each fluid mixture was tested on a different nanostructured surface to take into account the surface degradation/nanostructure ageing. Experiments were performed using pure HFE 7200 and the new fluid mixture on the same surface for comparison. As a result, the effect of nanostructures on the CHF enhancement would be the same for both the fluids. Any improvement in the heat transfer performance would therefore be due to the addition of new fluid to HFE 7200.

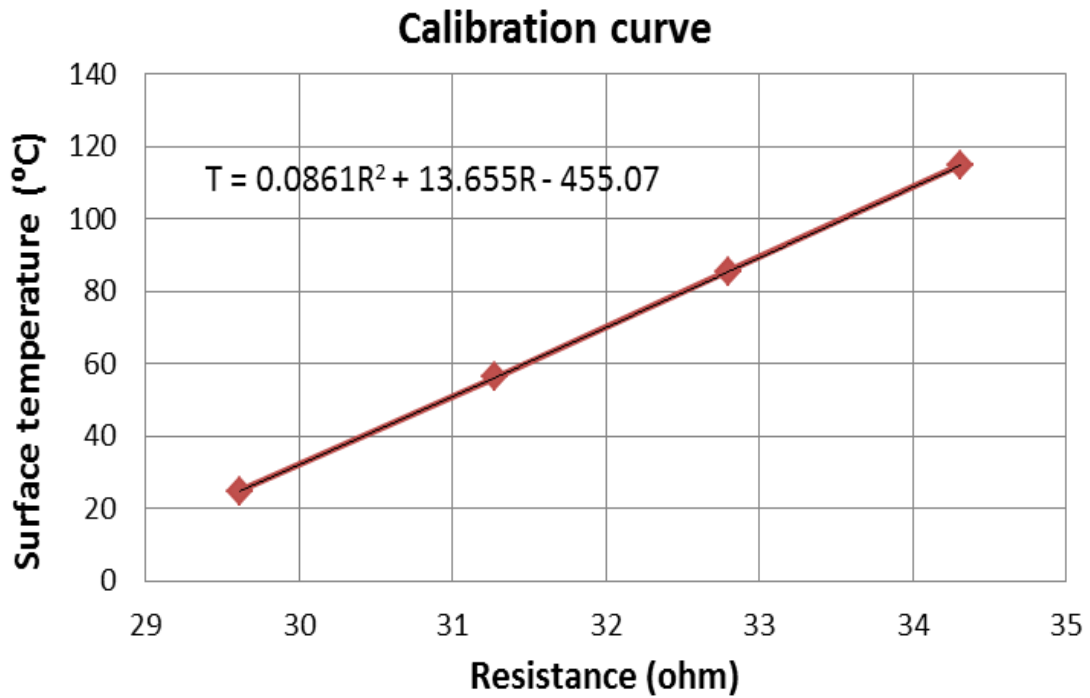


Figure 5.9: Temperature – resistance calibration curve for Pt RTD

### 5.3 Experimental Procedure

Pool boiling experiments were conducted at atmospheric pressure under both saturated and subcooled conditions. The liquid reservoir was initially filled with the test liquid. The inner glass chamber and the backside of the test chip were then maintained at vacuum conditions using a vacuum pump. The valve located immediately below the liquid reservoir was then opened. As the liquid reservoir is located vertically above the glass chamber, test liquid flows from the reservoir to the chamber because of gravity, and also due to the pressure difference between the liquid reservoir (atmospheric) and the inner glass chamber (vacuum). Before starting each experiment, the test fluid was degassed by vigorously boiling it for an hour. To measure the amount of air trapped in

the fluid, fluid samples were collected after vigorous boiling, in a sealed container and the air percentage was measured using Seaton Wilson Aire-ometer. The dissolved air percentage for pure HFE 7200, HFE 7200-methanol and HFE 7200-ethoxybutane mixtures were 34%, 31% and 32% respectively.

After degassing, the experiment was performed by supplying power to the test surface. The power to the test surface was varied by varying the voltage in increments of 1 V. At each power input, data were recorded once steady state conditions (temperature variation less than 0.5 °C over a 3 minute time period) were achieved. An average of at least one hundred readings was taken at each steady state for improved accuracy.

For the Pt RTD calibration, the test chip was shielded from the surroundings. However, during the experiments the test chip is immersed in the liquid bath and exposed to the surroundings. Since, the actual test conditions were different from the calibrated conditions of the heater, a corresponding offset was input to rectify the error in the calibrated data. To estimate the offset, the temperature value calculated from the resistance was subtracted from the actual temperature measured using the thermocouple immersed in the liquid bath. The same offset was then used for all the temperature readings of the test surface. All the measurements were monitored using LabVIEW<sup>TM</sup>. When the difference between two successive temperature measurements of the RTD was ~ 20 °C, it was considered that the boiling process was transitioning from fully developed nucleate boiling regime to film boiling regime. The CHF is calculated at the power input corresponding to the last observed steady state chip temperature, beyond which this sudden increase in temperature was observed. To prevent the burning of the test chip, its temperature limit was set at 125 °C. Power to the test chip was automatically cut-off, if

the chip temperature exceeded this value. Pool boiling experiments were performed at least twice at each setting to check for the repeatability of the results.

#### 5.4 Measurement Uncertainty

The uncertainty in the measurement of heat flux arises mainly due to the uncertainties in the measurement of voltage and current from the DC power supply; and uncertainty in the measurement of chip surface using a digital vernier calipers. Vacuum conditions were created on the backside of the chip to limit heat loss by conduction and convection. Therefore, heat loss from the bottom of the chip was assumed to be negligible. The effective heat flux ( $q''$ ) and the chip surface area ( $A$ ) are given by:

$$q'' = \frac{VI}{A} \quad (5.1)$$

$$A = L \times W \quad (5.2)$$

The uncertainties in the measurement of voltage, current; and the chip length and width are listed in Table 5.1. Following the procedure outlined by Kline and McClintock [54], the resulting uncertainty in the measurement of heat flux ( $w_{q''}$ ) is given by:

$$w_{q''} = \sqrt{\left(\frac{\partial q''}{\partial V} \cdot w_V\right)^2 + \left(\frac{\partial q''}{\partial I} \cdot w_I\right)^2 + \left(\frac{\partial q''}{\partial A} \cdot w_A\right)^2} \quad (5.3)$$

where,  $w_V$  is the uncertainty in voltage measurement,  $w_I$  is the uncertainty in current measurement, and  $w_A$  is the uncertainty in the measurement of chip surface area.

Table 5.1: Uncertainties in parameters

Parameter	Uncertainty (w)
Voltage (V)	$\pm (0.05\% + 5 \text{ mV})$
Current (I)	$\pm (0.15\% + 5 \text{ mA})$
Chip length (L)	$\pm 0.01 \text{ mm}$
Chip width (W)	$\pm 0.01 \text{ mm}$

The maximum uncertainty in the measurement of heat flux is 1.6% based on Equation 5.3. The uncertainty in the measurement of the chip surface temperature arises mainly due to the uncertainty in the measurement of chip resistance. The chip resistance (R) and the uncertainty in the resistance ( $w_R$ ) are given by:

$$R = \frac{V}{I} \quad (5.4)$$

$$w_R = \sqrt{\left(\frac{\partial R}{\partial V} \cdot w_V\right)^2 + \left(\frac{\partial R}{\partial I} \cdot w_I\right)^2} \quad (5.5)$$

The uncertainty in the measurement of chip surface temperature was estimated based on the temperature – resistance calibration curve for each test chip package. The maximum uncertainty in the chip temperature was estimated to be  $\pm 1.5 \text{ }^\circ\text{C}$ .



## 5.5 Experimental Results

### 5.5.1 Effect of Enhanced Surfaces

Pool boiling experiments were first performed using pure HFE 7200 on a bare chip (top layer is SiO<sub>2</sub>) and on various nanostructured surfaces to evaluate the heat transfer performance of these enhanced surfaces. The effect of these enhanced surfaces on pool boiling performance of HFE 7200 at saturation condition is shown in Figure 5.10.

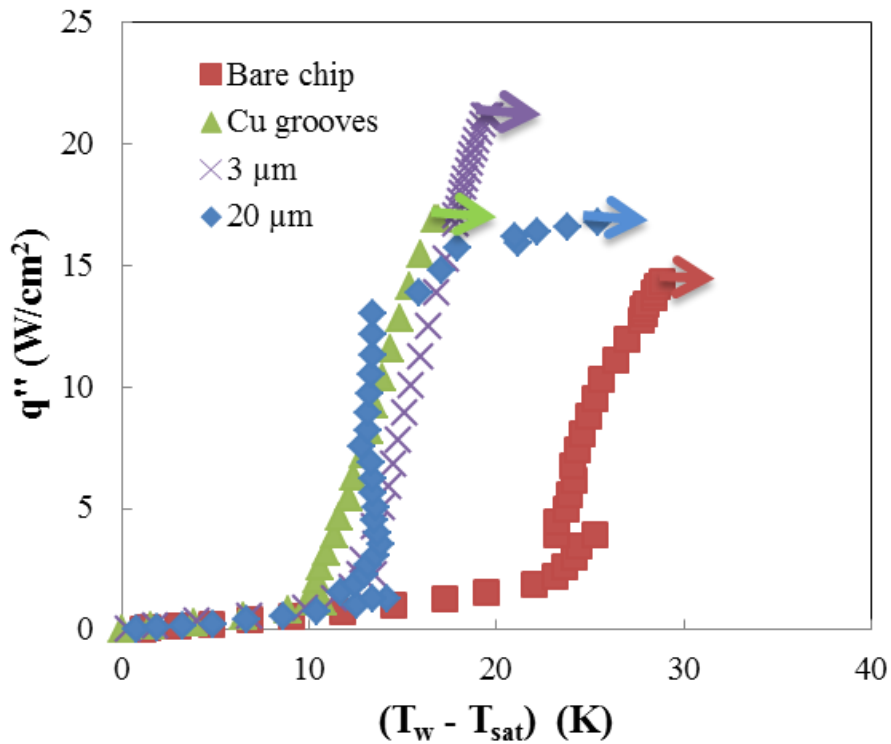


Figure 5.10: Pool boiling of HFE 7200 on a bare chip, Cu groove surface (width – 70 μm and depth – 70 μm), 3 μm tall and 20 μm tall Cu nanowire surfaces

It can be observed that these nanostructured surfaces increase the CHF and reduce the wall superheat at the onset of nucleate boiling (ONB), when compared to a bare substrate. This enhancement in heat transfer could be due to the increase in the number of

nucleation sites for boiling on enhanced surfaces [55]. Also, the nanowire height plays an important role in the CHF enhancement. It can be observed that the CHF for 3  $\mu\text{m}$  tall Cu nanowire surface was higher than that of 20  $\mu\text{m}$  tall nanowire surface. As the nanowire height increases, the capillary force that draws the liquid to the surface increases. However, taller structures restrict the movement of vapor by causing a large drag force and as a result, trap the vapor between the nanowires. This trapped vapor might lead to an early dryout and lower the CHF. Therefore, an optimum height exists at which the CHF is maximum, and this optimum height was around 3  $\mu\text{m}$  based on a study by Im [55].

Since these enhanced surfaces showed an improvement in the heat transfer performance, pool boiling experiments with various new fluid mixtures were performed on nanostructured surfaces.

### **5.5.2 Pool Boiling of HFE 7200 – Ethoxybutane and HFE 7200 - Methanol Mixtures**

Pool boiling experiments were performed using pure HFE 7200, 10 vol. % methanol + 90 vol. % HFE 7200 mixture, and 10 vol. % ethoxybutane + 90 vol. % HFE 7200 mixture on a surface coated with 4  $\mu\text{m}$  nanowire array. The SEM image of this surface is shown in Figure 5.5. The vapor liquid equilibrium (VLE) curves for the mixtures of HFE 7200 – ethoxybutane and HFE 7200 – methanol are shown in Figures 4.6 and 4.7 respectively. The mixture of HFE 7200 – ethoxybutane is assumed to be an azeotrope at 10 vol. % (molefraction of 0.1) as both the bubble point and dew point curves coincide at this concentration. The mixture of HFE 7200 – methanol is a non-azeotrope at 10 vol. % (molefraction of 0.4) wherein boiling occurs over a temperature range.

The boiling curves for the three fluids at saturation condition, 10K and 20K subcooled conditions are shown in Figures 5.11, 5.12 and 5.13 respectively. From these figures, it can be observed that the wall superheat for the ONB is lowest for the mixture of HFE 7200 – ethoxybutane among the three test fluids, for saturated condition and for 10K and 20K subcooling. Also, the CHF is highest for the mixture of HFE 7200 – methanol for saturated and subcooled conditions. The CHF of both the mixtures are higher than that of pure HFE 7200 for all cases. For pool boiling at saturated conditions, the enhancement in CHF for mixtures of HFE 7200 – methanol and HFE 7200 – ethoxybutane over pure HFE 7200 are 24% and 10.7%.

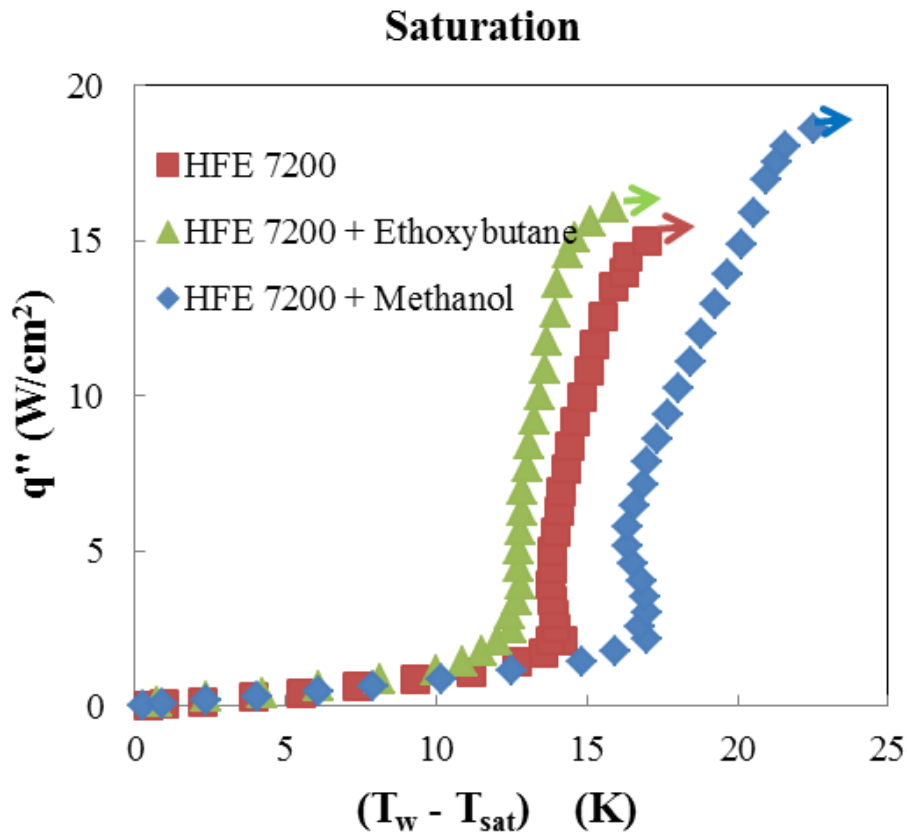


Figure 5.11: Pool boiling curves for HFE 7200, 10 vol. % mixtures of HFE 7200 – ethoxybutane and HFE 7200 – methanol at saturation condition on 4  $\mu\text{m}$  nanowire array

For pool boiling at 10K subcooled condition, the enhancement in CHF for mixtures of HFE 7200 – methanol and HFE 7200 – ethoxybutane over pure HFE 7200 are 34.2% and 18.6%. For pool boiling at 20K subcooled condition, the enhancement in CHF for mixtures of HFE 7200 – methanol and HFE 7200 – ethoxybutane over pure HFE 7200 are 16.7% and 9.8%. Also, there is no significant change in the boiling curves for these three fluids at 20K subcooling. These results indicate that addition of methanol and ethoxybutane to pure HFE 7200 brings about considerable changes in CHF and incipience temperature for pool boiling of these new mixtures.

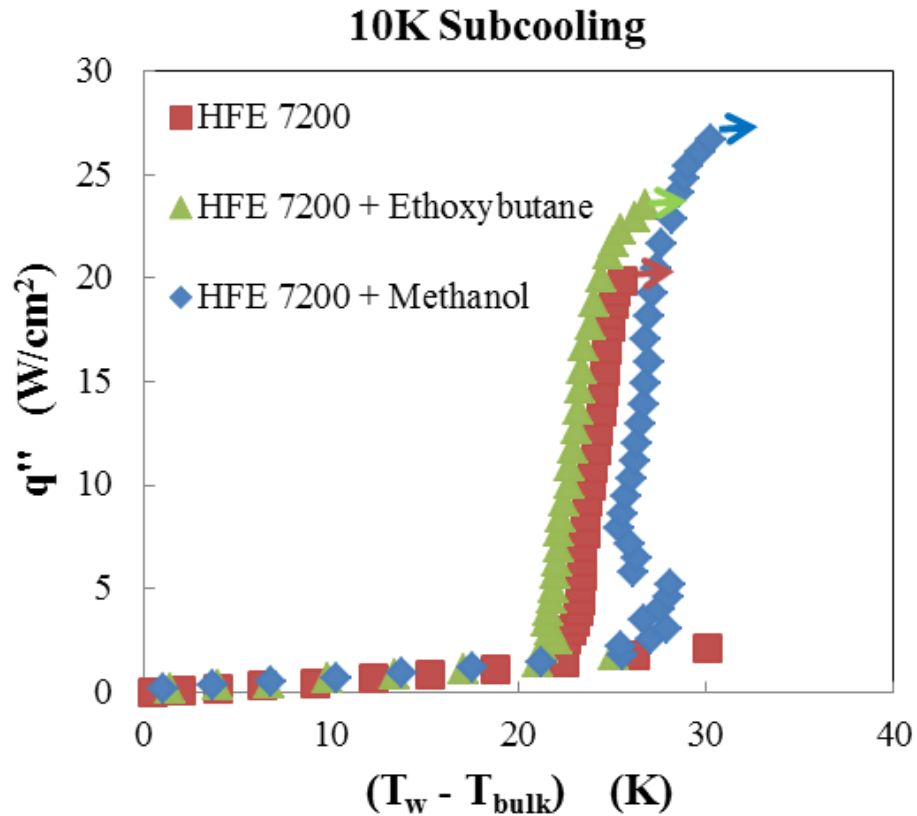


Figure 5.12: Pool boiling curves for HFE 7200, 10 vol. % mixtures of HFE 7200 – ethoxybutane and HFE 7200 – methanol at 10K subcooling on 4  $\mu$ m nanowire array

Also, from Figure 5.11, it can be observed that the heat transfer coefficient ( $h = q'' / (T_w - T_{sat})$ ) is higher for HFE – ethoxybutane mixture than the other two fluids at all heat fluxes. However, at 20K subcooled condition (Figure 5.13), the boiling curves for all three fluids closely match. Therefore, the heat transfer coefficients are the same for all the fluids.

The boiling points of pure HFE 7200, ethoxybutane and methanol are 76 °C, 92 °C and 65 °C respectively. The increase in the CHF of HFE 7200 – ethoxybutane mixture might be attributed to Marangoni effect. Although this mixture was assumed to be an azeotrope, this effect cannot be ruled out because of errors in the estimation of bubble point and dew point. A 10 vol. % mixture of HFE 7200 – ethoxybutane is a positive mixture wherein the more volatile liquid (HFE 7200) has a lower surface tension than the less volatile liquid (ethoxybutane). Surface tension gradients arising due to the preferential evaporation of HFE 7200 at the chip surface might act to enhance the flow of liquid from bulk to the surface. This could delay the dry out process and increase the CHF of the HFE 7200 – ethoxybutane mixture. However, the same mechanism cannot account for the increase in CHF of HFE 7200 – methanol mixture as it is a negative mixture [56], and as such should reduce the CHF. Hence it is clear that there are additional mechanisms which play an important role in the enhancement of CHF for binary mixtures. A significantly large latent heat of evaporation for HFE 7200 – methanol mixture could play an important role in enhancing the CHF of this negative mixture.

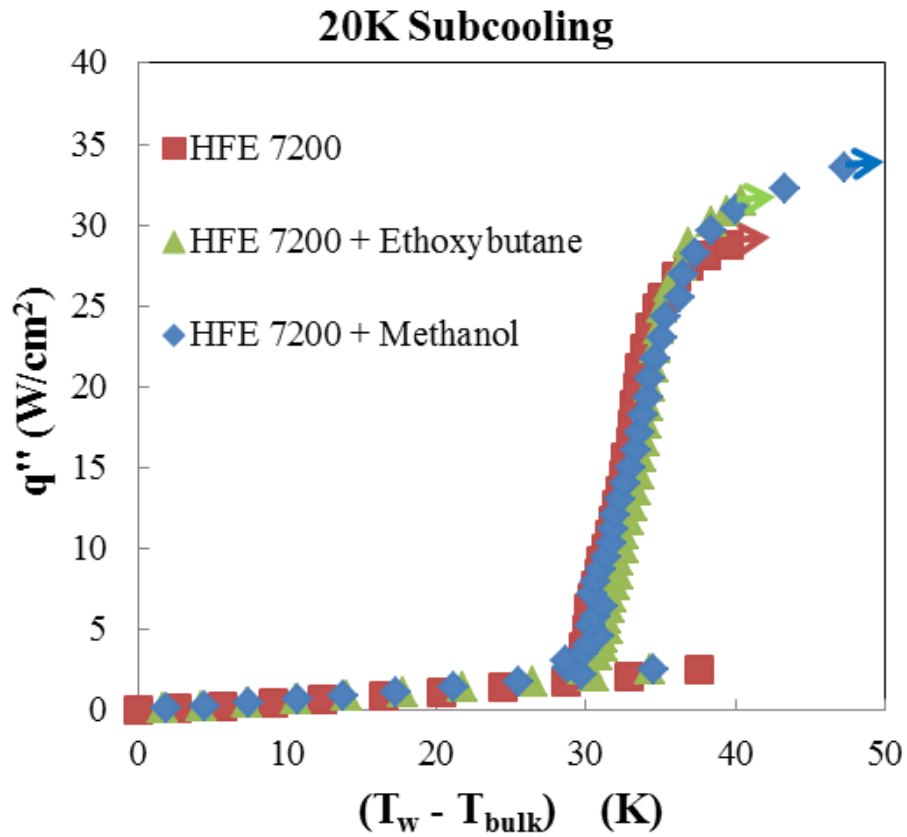


Figure 5.13: Pool boiling curves for HFE 7200, 10 vol. % mixtures of HFE 7200 – ethoxybutane and HFE 7200 – methanol at 20K subcooling on 4  $\mu$ m nanowire array

### 5.5.3 Pool Boiling of HFE 7200 – C<sub>6</sub>H<sub>11</sub>F<sub>3</sub> Mixture

Pool boiling experiments were performed using pure HFE 7200 and 7 wt. % C<sub>6</sub>H<sub>11</sub>F<sub>3</sub> + 93 wt. % HFE 7200 mixture at saturation condition on a hybrid micro-nanostructured surface. Grooves (width – 70  $\mu$ m, depth – 70  $\mu$ m ) were cut into the surface coated with Cu using an automated dicing saw. CuO nanostructures were then deposited on this surface using electrochemical deposition. More details on this nanostructured surface fabrication are available elsewhere [53]. The SEM image of this surface is shown in Figure 5.8. The vapor liquid equilibrium (VLE) curve for the mixture

of  $C_6H_{11}F_3$  – HFE 7200 is shown in Figure 4.8. The mixture of  $C_6H_{11}F_3$  – HFE 7200 is a non-azeotrope at 7 wt. % concentration.

The pool boiling curves for pure HFE 7200 and 7 wt. % mixture of  $C_6H_{11}F_3$  – HFE 7200 are shown in Figures 5.14 and 5.15 respectively. Experiments were performed thrice (Run 1, Run 2 and Run 3) for each fluid to check for the repeatability of the results. Pure HFE 7200 has a CHF of  $20.2 \text{ W/cm}^2$ , while the 7 wt. % mixture of  $C_6H_{11}F_3$  – HFE 7200 has a CHF of  $21.6 \text{ W/cm}^2$ . The enhancement in CHF over pure HFE 7200 was found to be 6.9%, whereas the wall superheat for the onset of nucleate boiling (ONB) was similar for both pure HFE 7200 and for the mixture of  $C_6H_{11}F_3$  – HFE 7200. This suggests that addition of larger amounts of  $C_6H_{11}F_3$  is likely to lead to further improvements in CHF. Therefore, the heat transfer performance of pure  $C_6H_{11}F_3$  is likely to be significantly better than that of HFE 7200.

## HFE 7200

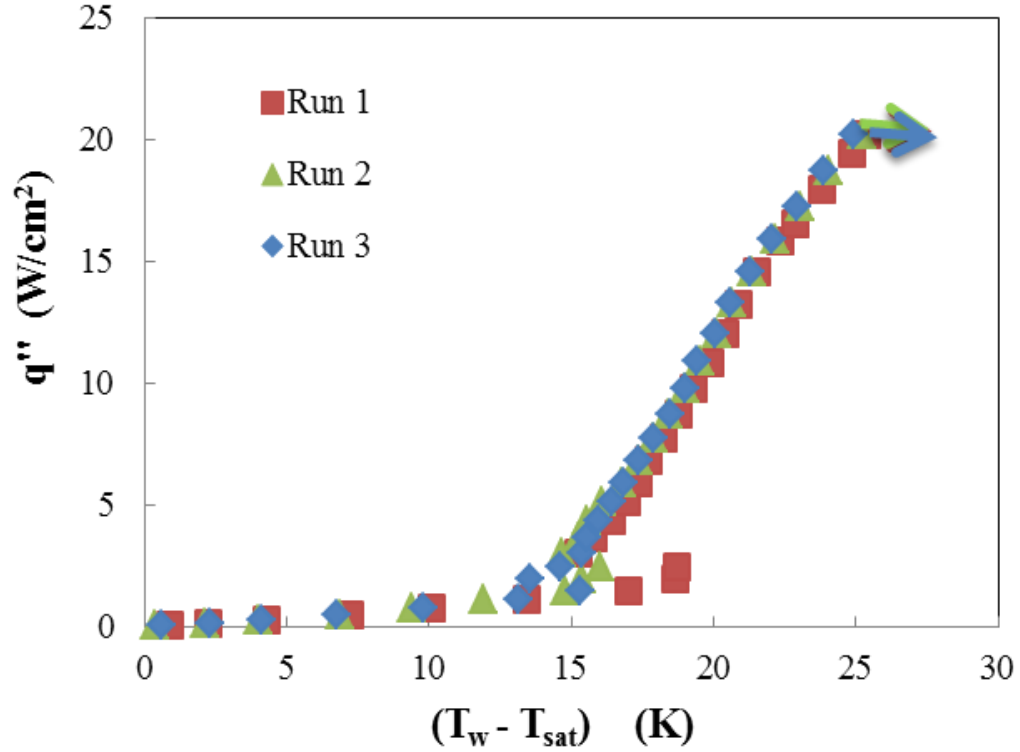


Figure 5.14: Pool boiling curves for HFE 7200 at saturation condition on hybrid micro-structured surface

The CHF is a function of the non-dimensional heater size  $L'$  ( $L' = L/L_c$ ) for  $L' < 20$  [57], where  $L$  is the length of the heater and  $L_c$  is the capillary length. The capillary length ( $L_c$ ), which is the ratio of surface tension and buoyancy forces, is defined as

$$L_c = \sqrt{\frac{\sigma}{g(\rho_l - \rho_v)}} \quad (5.6)$$

The non-dimensional heater size for pure HFE 7200, which has a capillary length of 0.99 mm, is  $L' = 10.1 (< 20)$ . Hence the CHF is heater size dependent. Therefore,



results from this work should not be compared with those involving infinite heater arrangements, but should be used only to compare the relative pool boiling performance of pure HFE 7200 with that of its mixture with new fluids. Since the pool boiling experiments for pure HFE 7200 and all fluid mixtures were performed on the same substrate, differences in the incipience superheat and the CHF can be attributed to differences in fluid properties.

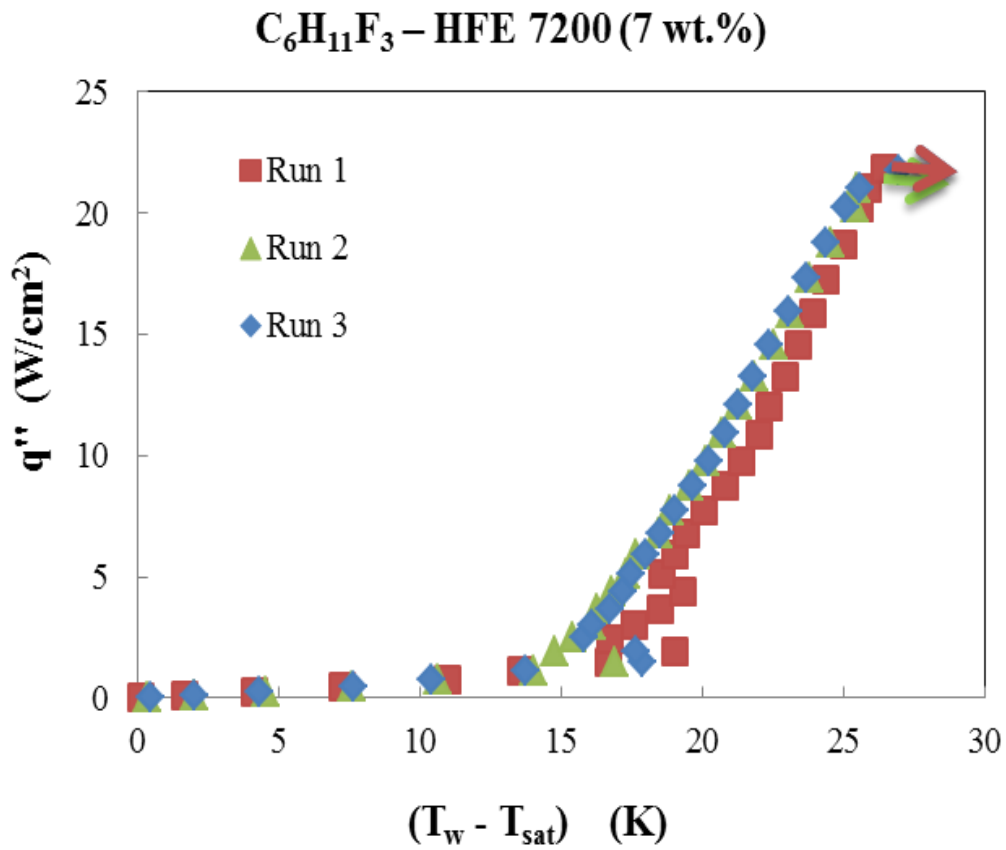


Figure 5.15: Pool boiling curves for 7 wt.% mixture of HFE 7200 –  $C_6H_{11}F_3$  at saturation condition on hybrid micro-nanostructured surface

### 5.5.4 Pool Boiling of HFE 7200 – C<sub>4</sub>H<sub>4</sub>F<sub>6</sub>O Mixture

Pool boiling experiments were performed using HFE 7200 and 10 wt. % C<sub>4</sub>H<sub>4</sub>F<sub>6</sub>O + 90 wt. % HFE 7200 mixture at saturation condition on a hybrid micro-nanostructured surface. The SEM image of this surface is shown in Figure 5.8. The vapor liquid equilibrium (VLE) curve for the mixture of C<sub>4</sub>H<sub>4</sub>F<sub>6</sub>O - HFE 7200 is shown in Fig. 4.9. The mixture of C<sub>4</sub>H<sub>4</sub>F<sub>6</sub>O – HFE 7200 is a non-azeotrope at 10 wt. % concentration.

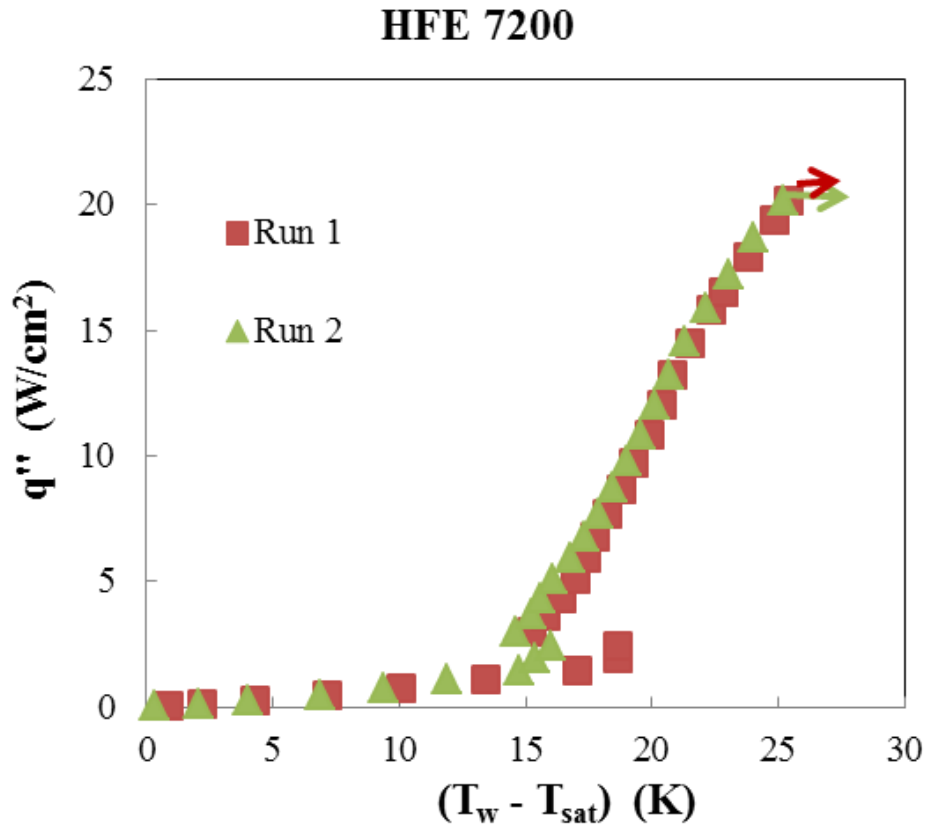


Figure 5.16: Pool boiling curves for HFE 7200 at saturation condition on hybrid micro-nanostructured surface

The pool boiling curves for pure HFE 7200 and 10 wt. % mixture of  $C_4H_4F_6O$  – HFE 7200 are shown in Figures 5.17 and 5.18 respectively. The experiments were performed at least twice (Run 1 and Run 2) to check the repeatability of the results. Pure HFE 7200 has a CHF of  $20.2 \text{ W/cm}^2$ , while the 10 wt. % mixture of  $C_4H_4F_6O$  – HFE 7200 has a CHF of  $21.9 \text{ W/cm}^2$ . The enhancement in the CHF for this fluid mixture over pure HFE 7200 is 8.4%. However, the mixture has a higher wall superheat ( $\Delta T = 22.2$  °C) at the onset of nucleate boiling than pure HFE 7200 ( $\Delta T = 18.7$  °C).

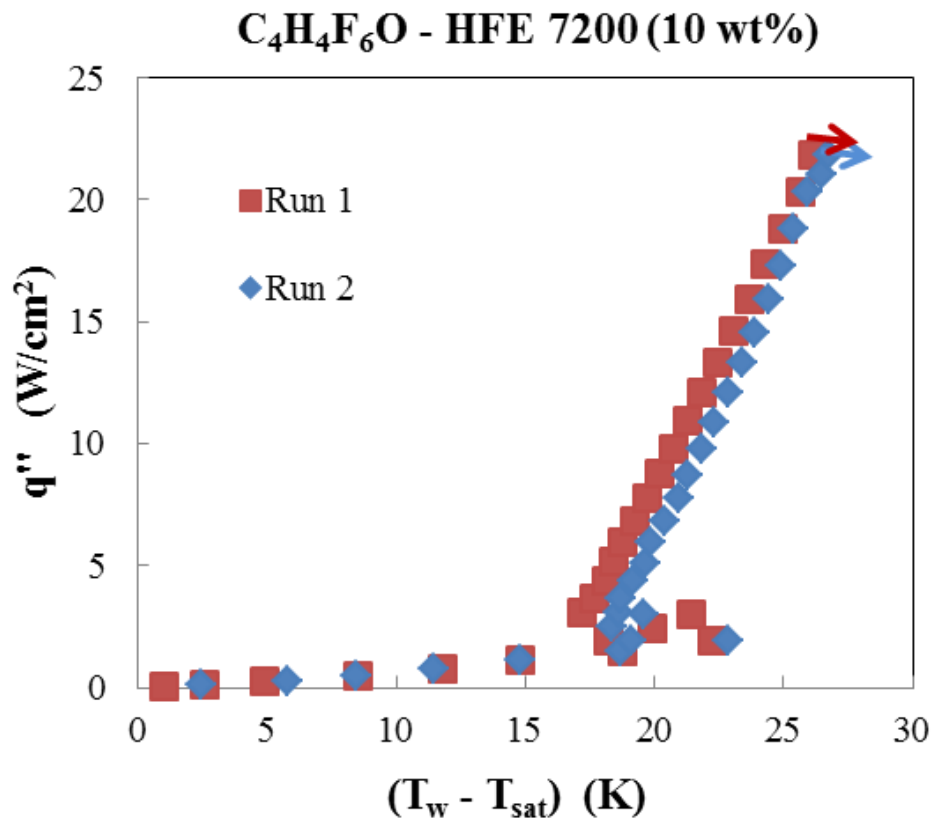


Figure 5.17: Pool boiling curve for 10 wt.% mixture of HFE 7200 –  $C_4H_4F_6O$  at saturation condition on hybrid micro-nanostructured surface

### 5.5.5 Pool Boiling of HFE 7200 – C<sub>4</sub>H<sub>5</sub>F<sub>3</sub>O Mixture

Pool boiling experiments were performed with HFE 7200 and 20 wt. % C<sub>4</sub>H<sub>5</sub>F<sub>3</sub>O + 80 wt. % HFE 7200 mixture on a hybrid micro-nanostructured surface at saturation condition. The SEM image of this surface is shown in Figure 5.7. The vapor liquid equilibrium (VLE) curve for the mixture of C<sub>4</sub>H<sub>5</sub>F<sub>3</sub>O - HFE 7200 is shown in Figure 4.10. The mixture of C<sub>4</sub>H<sub>5</sub>F<sub>3</sub>O – HFE 7200 is a non-azeotrope at 20 wt. % concentration.

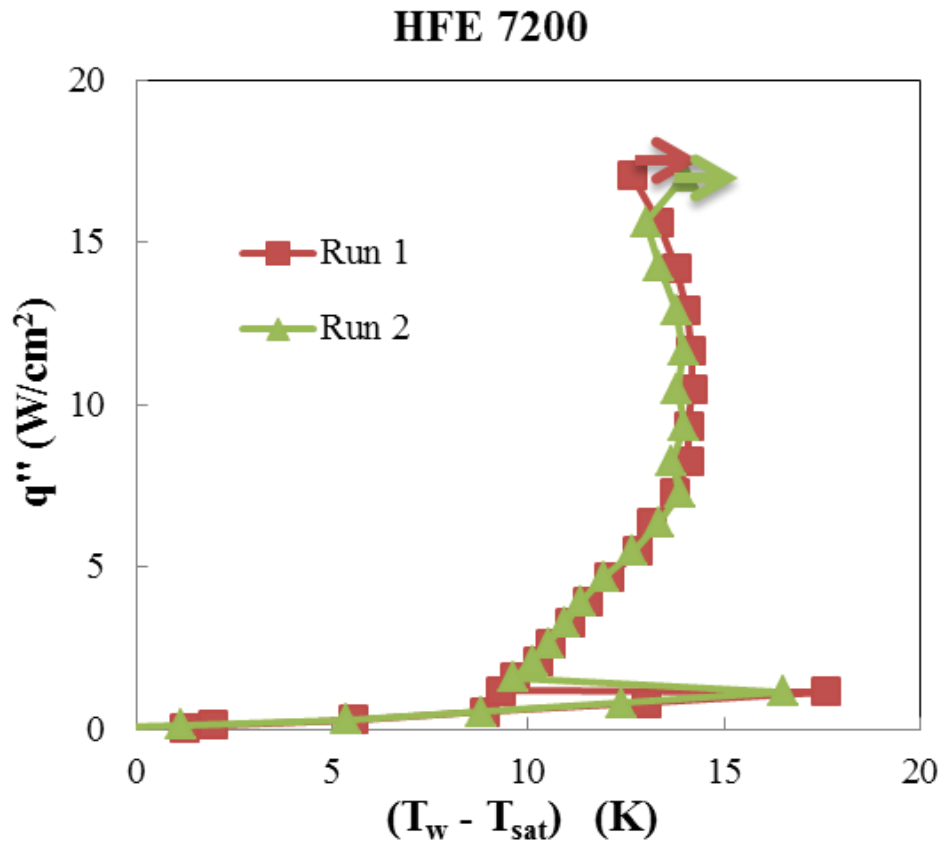


Figure 5.18: Pool boiling curves for HFE 7200 at saturation condition on hybrid micro-nanostructured surface

The boiling curves for pure HFE 7200 and 20 wt. % mixture of C<sub>4</sub>H<sub>5</sub>F<sub>3</sub>O – HFE 7200 are shown in Figures 5.18 and 5.19 respectively. The boiling experiments were performed at least twice (Run 1 and Run 2) for each fluid to check the repeatability of the

results. It can be observed from Figure 5.18 that the wall temperature drops at heat fluxes above  $12 \text{ W/cm}^2$ . From visual observation, it was noticed that certain areas on the chip were not active at low heat fluxes, and all these sites became active nucleation sites at heat fluxes above  $12 \text{ W/cm}^2$ . This could possibly be the reason for the observed drop in wall temperature. For pool boiling at saturated condition, the CHF for pure HFE 7200 and 20 wt. % mixture of  $\text{C}_4\text{H}_5\text{F}_3\text{O}$  – HFE 7200 was  $17.1 \text{ W/cm}^2$  and  $20 \text{ W/cm}^2$  respectively. The enhancement in the CHF of the mixture over pure HFE 7200 was 17%. The wall superheat at the onset of nucleate boiling was higher for the mixture ( $\Delta T = 18.4 \text{ }^\circ\text{C}$ ) than HFE 7200 ( $\Delta T = 17.6 \text{ }^\circ\text{C}$ ). It should be noted here that the bubble point temperature of the mixture ( $T_b = 60 \text{ }^\circ\text{C}$ ) is lower than the saturation temperature of HFE 7200 ( $T_b = 72 \text{ }^\circ\text{C}$ ).

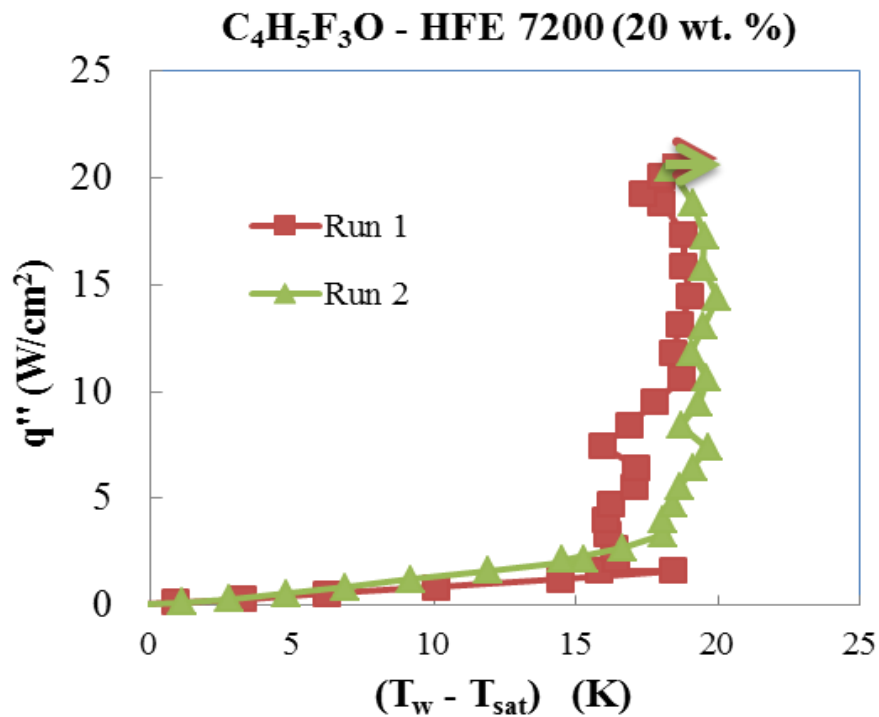


Figure 5.19: Pool boiling curve for 20 wt.% mixture of HFE 7200 –  $\text{C}_4\text{H}_5\text{F}_3\text{O}$  at saturation condition on hybrid micro-nanostructured surface

### 5.5.6 Pool Boiling of HFE 7200 – C<sub>4</sub>H<sub>12</sub>O<sub>2</sub>Si Mixture

Pool boiling experiments were performed with HFE 7200 and 10 wt. % C<sub>4</sub>H<sub>12</sub>O<sub>2</sub>Si + 90 wt. % HFE 7200 mixture on a hybrid micro-nanostructured surface, similar to the one shown in Figure 5.8, at saturation condition. The vapor liquid equilibrium (VLE) curve for the mixture of C<sub>4</sub>H<sub>12</sub>O<sub>2</sub>Si - HFE 7200 is shown in Figure 4.11. The mixture of C<sub>4</sub>H<sub>12</sub>O<sub>2</sub>Si – HFE 7200 is assumed to be an azeotrope at 10 wt. % concentration.

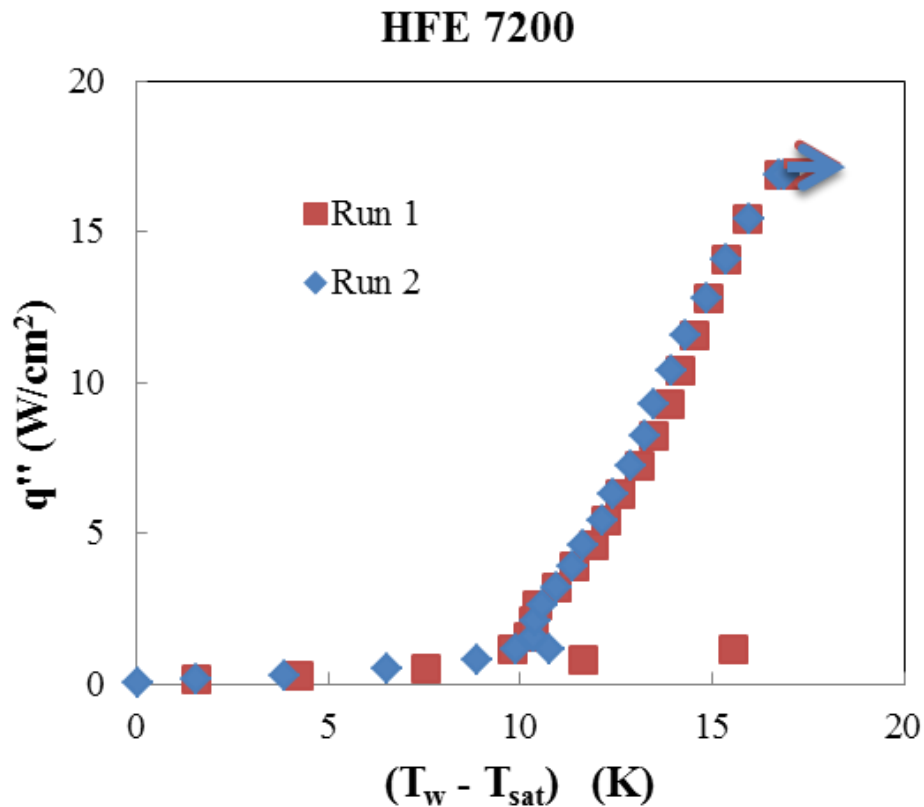


Figure 5.20: Pool boiling curves for HFE 7200 at saturation condition on hybrid micro-nanostructured surface

The boiling curves for pure HFE 7200 and 10 wt. % mixture of  $C_4H_{12}O_2Si$  – HFE 7200 are shown in Figures 5.20 and 5.21 respectively. The boiling experiments were performed atleast twice (Run 1 and Run 2) for each fluid to check the repeatability of the results. The boiling curves were similar for Run 1 and Run 2 for pure HFE 7200, however, there were differences in the boiling curves for the mixture. The wall superheat at the ONB was lower for Run 2 than Run 1 for the mixture. It is speculated that a large amount of vapor could have been trapped in the cavities after Run 1 for the mixture, which could have caused this decrease in wall superheat. As high speed visualization was not performed, it is not clear if the bubble departure parameters were significantly different for both the runs.

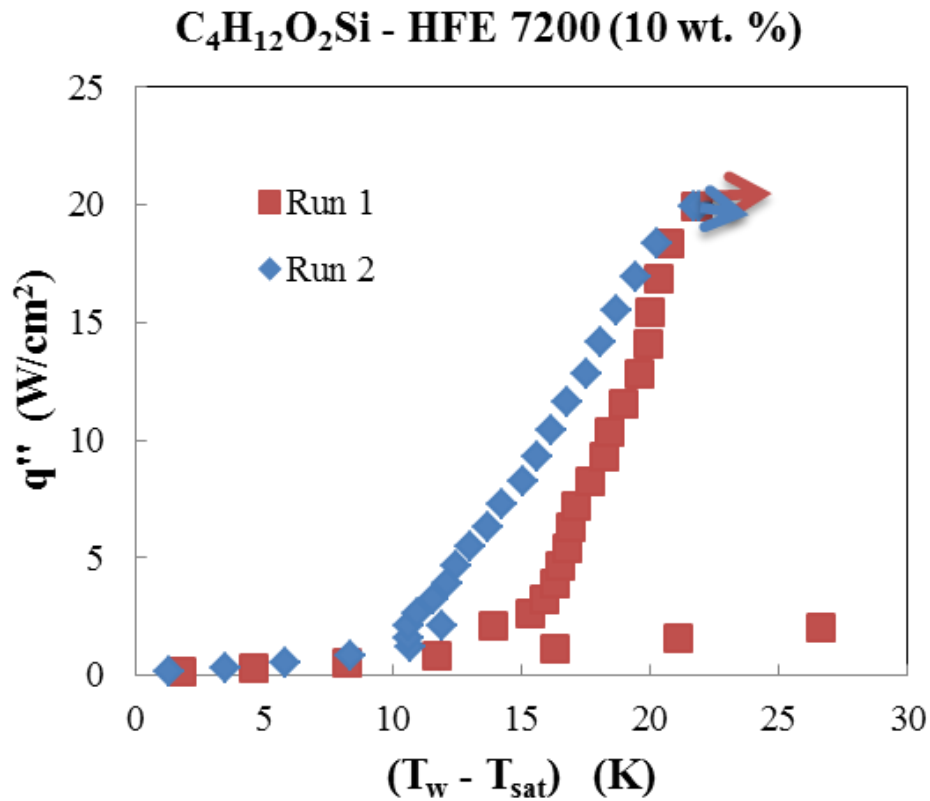


Figure 5.21: Pool boiling curves for 10 wt.% mixture of HFE 7200 –  $C_4H_{12}O_2Si$  at saturation condition on hybrid micro-nanostructured surface

For pool boiling at saturated condition, the CHF for pure HFE 7200 and 10 wt. % mixture of  $C_4H_{12}O_2Si$  – HFE 7200 was  $16.9 \text{ W/cm}^2$  and  $19.9 \text{ W/cm}^2$  respectively. The enhancement in the CHF of the mixture over pure HFE 7200 was 17.8%. In addition, the incipience temperature of the mixture was found to be lower than that of pure HFE 7200. The results indicate that addition of dimethoxydimethylsilane to HFE 7200 improves heat transfer performance.

### **5.5.7 Pool Boiling of HFE 7200 – $C_4H_{11}N$ Mixture**

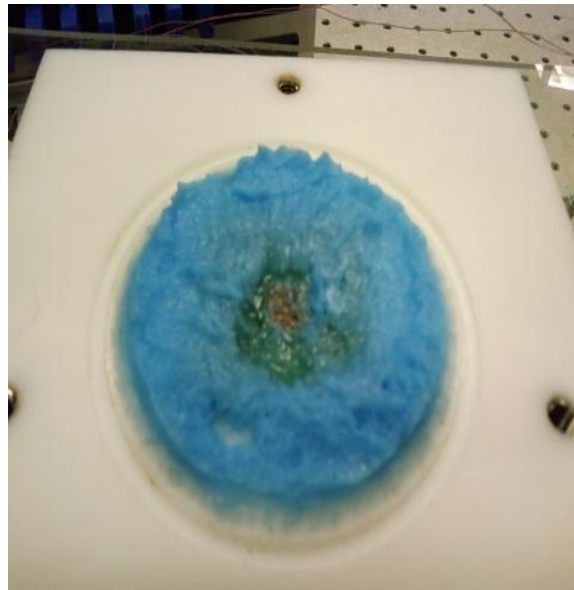
Pool boiling experiments were performed with 10 wt. %  $C_4H_{11}N$  + 90 wt. % HFE 7200 on a  $20 \mu\text{m}$  Cu nanowire array at saturation condition. The SEM image of this surface is shown in Figure 5.6. The FOM predictions show that  $C_4H_{11}N$  has the potential to enhance heat transfer better than HFE 7200. However, the 10 wt. % mixture deposited blue sediments on the test chip and the glass walls during the experiments.

To avoid further damage to the glass chamber walls and the Teflon block, the experiments were terminated. The sediments deposited on the glass walls and the test chip is shown in Figure 5.22. These sediments were observed to be forming at the glass walls. To perform saturated boiling experiments, the temperature of the water circulating on the periphery of the inner glass chamber was set to a value greater than the bubble point temperature of the mixture. As a result, the glass walls were also at a temperature greater than the bubble point temperature of the mixture. Boiling was observed at certain locations on the glass walls and these nucleation sites served as the source for the observed sediments.





(a)



(b)

Figure 5.22: Sediments deposited during saturated boiling of 10 wt. % mixture of  $C_4H_{11}N$  – HFE 7200 on a) glass walls, and b) test chip

## 5.6 CHF Prediction for Higher Mixture Concentrations

The new heat transfer fluids identified using the CAMD approach are designed to be applicable for direct immersion cooling on both small heaters and infinite heaters. The experimental results show a moderate improvement in the CHF of new fluid mixtures over pure HFE 7200. To evaluate the pool boiling performance of higher mixture concentrations, the CHF is predicted using Zuber's correlation [58] for infinite flat heater, and Lienhard and Dhir's correlation [59] for small flat heater. These correlations for infinite flat heater and small flat heater are shown in Equations 5.7 and 5.8 respectively. The predicted CHF values for different weight fractions of new fluids are plotted for an infinite heater and a small heater; and are shown in Figures 5.23 and 5.24 respectively.

$$q_{CHF\_Z}'' = \frac{\pi}{24} \sqrt{\rho_v} h_{fg} [\sigma g (\rho_l - \rho_v)]^{1/4} \quad (5.7)$$

$$q_{CHF}'' = q_{CHF\_Z}'' \left( \frac{1.14 \lambda_d^2}{A_{heater}} \right) \quad (5.8)$$

where  $\lambda_d$  is the Taylor wavelength ( $\lambda_d = 2\pi\sqrt{3L_c}$ ) and  $A_{heater}$  is the area of the heater ( $10 \times 10 \text{ mm}^2$ ).

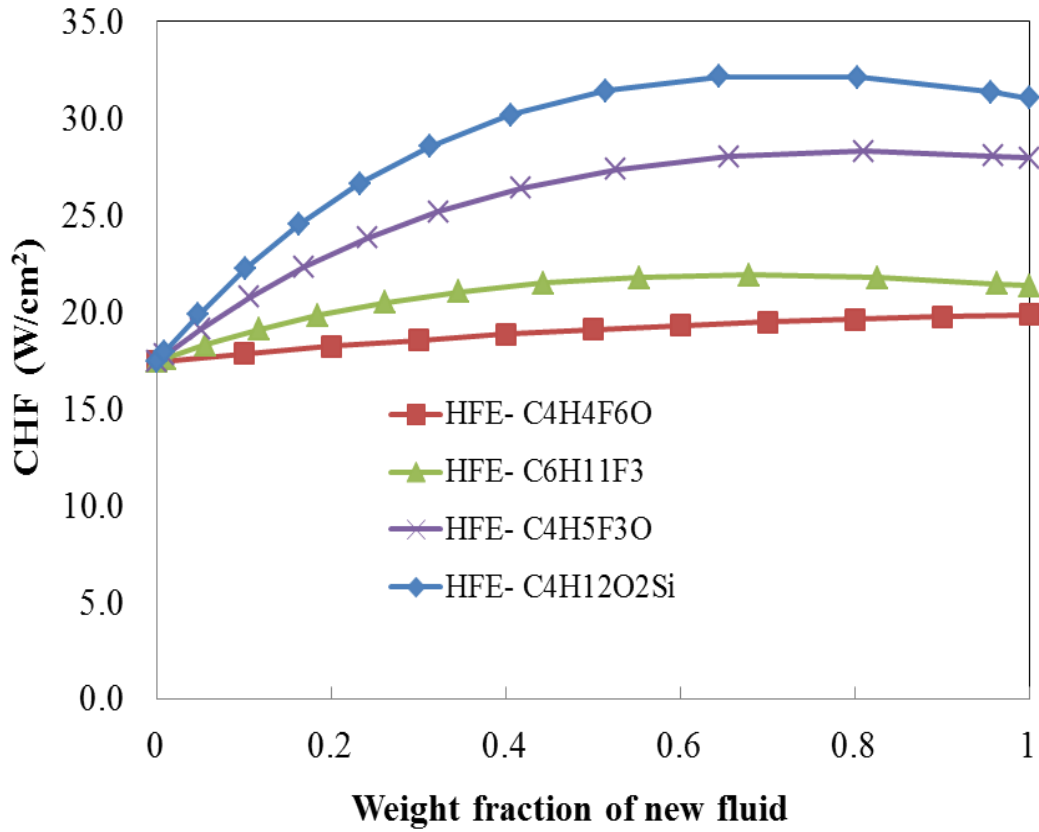


Figure 5.23: CHF prediction for different concentrations of new fluid – HFE 7200 mixtures on an infinite heater

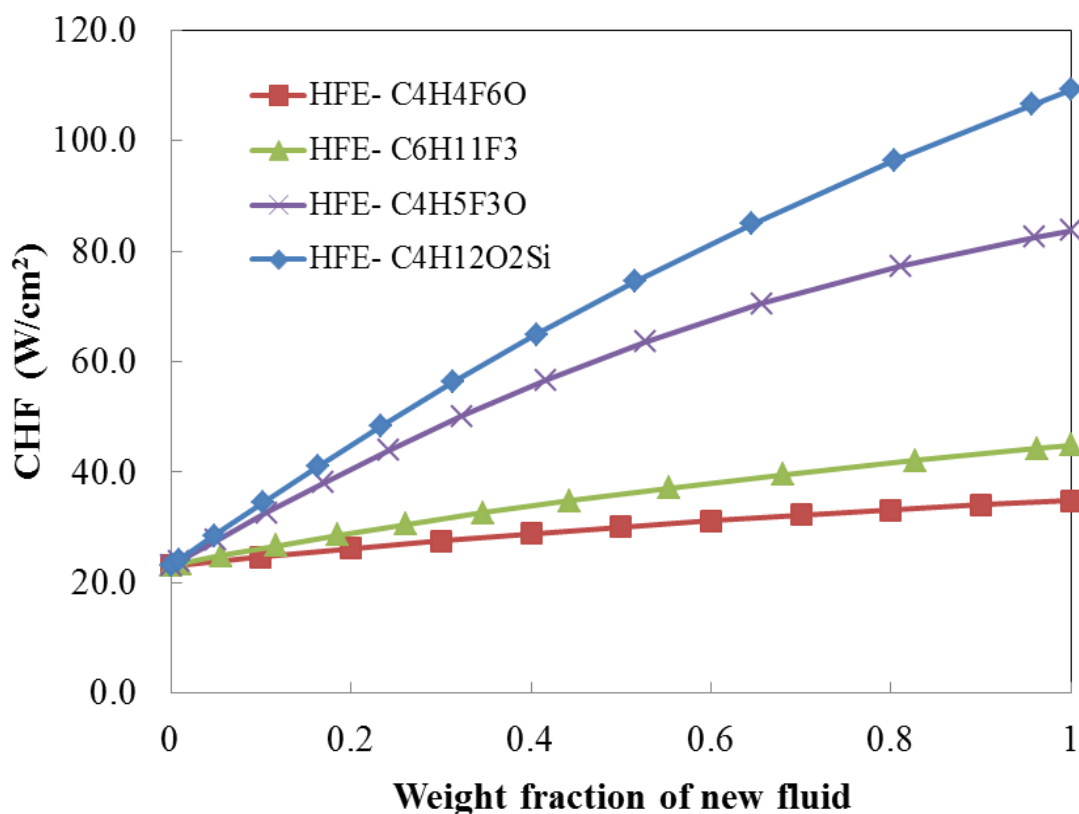


Figure 5.24: CHF prediction for different concentrations of new fluid – HFE 7200 mixtures on a small heater of area 10 x 10 mm<sup>2</sup>.

It should be noted that these correlations are applicable only for plain surface and cannot be used for the Cu nanowire/CuO hybrid micro-nanostructured surfaces used for the pool boiling experiments. However, these calculations show whether significant improvements to the CHF can be expected at higher mixture concentrations of new fluids with HFE 7200. It can be inferred from these plots that significant improvements in the heat transfer performance can be expected at higher mixture concentrations. Also, all the new fluids (weight fraction of 1) show better heat transfer performance than the base fluid, HFE 7200.

## 5.7 CHF Mechanism

The mechanism leading to CHF in pool boiling can be classified into two categories: a) Far field and b) Near field

**Far field:** Far field mechanisms deal with the fluid dynamics far away from the surface and the occurrence of CHF is because of hydrodynamic instabilities. As the heat flux increases, the velocity of the vapor columns increase, thereby increasing the velocity shear between the upward flowing vapor and the downward flowing liquid. Eventually these vapor columns become unstable and prevent the wetting of liquid on the surface. Zuber's CHF model [58] for a plain surface postulates that the radius of the vapor columns is  $\lambda_D/4$  and the spacing between the vapor columns is  $\lambda_D$ , where  $\lambda_D$  is the Taylor instability wavelength. The correlation for CHF based on Zuber's model is:

$$q_{CHF\_Z}'' = \frac{\pi}{24} h_{fg} \sqrt{\rho_v} [g\sigma(\rho_l - \rho_v)]^{1/4} \quad (5.9)$$

For a nanostructure coated surface, the cavities in the nanowire array could provide the least resistance path for the upward flowing vapor and thereby, alter the critical spacing between the vapor columns. Figure 5.25 shows the cavities on a nanowire coated surface. The modified Zuber CHF correlation [60] taking into account the modified vapor column spacing because of cavities in the porous structure is given by:

$$q_{CHF\_h}'' = q_{CHF\_Z}'' \sqrt{\frac{\lambda_D}{\lambda_\mu}} \quad (5.10)$$

and  $\lambda_{\mu} = \left[ \frac{\pi}{5.88\varepsilon^{2.28}} \right]^2 d_{br}$ , where  $\varepsilon$  is the porosity of the medium and  $d_{br}$  is the departure diameter of the bubbles.

The term  $\lambda_{\mu}$  represents the modified spacing between the vapor columns on a nanowire coated surface. In addition to this, for pool boiling of mixtures, surface tension gradients may exist along the liquid – vapor interface. There are two types of mixtures [15]: positive mixture and negative mixture. For a positive mixture, the surface tension of the more volatile component is less than the surface tension of the less volatile component. For a negative mixture, the surface tension of the more volatile component is more than the surface tension of the less volatile component. Depending on whether the mixture is positive or negative, the surface tension gradients might act to enhance or retard the flow of liquid from the bulk to the surface. Taking into account the surface tension gradients [15], the modified CHF correlation for pool boiling of mixtures on porous surface is given by:

$$q_{CHF\_f}'' = q_{CHF\_h}'' \left[ 1 + c_m \left( \frac{1}{\sigma} \right) \frac{\partial \sigma}{\partial x} (y_b - x_b) \right]^{1/4} \quad (5.11)$$

where  $c_m$  is a proportionality constant,  $\sigma$  is the liquid surface tension,  $x_b$  is the molefraction of more volatile fluid in the bulk in liquid phase,  $y_b$  is the molefraction of more volatile fluid in the bulk in vapor phase ( $x_b$  and  $y_b$  are obtained from the VLE diagrams). For a pure fluid the concentration of the more volatile component in the liquid and vapor phase is the same ( $y_b = x_b$ ). So the above equation reduces to Equation 5.10. To obtain the surface tension gradient, the mixture surface tension was plotted as a function

of the concentration. If it is assumed that because of preferential evaporation, the more volatile component completely evaporates at the heater surface, then the slope of the this curve at 100% concentration of the least volatile component would give the surface tension gradient. As experiments were performed at low mixture concentrations,  $y_b = x_b$  for azeotropes and as a result, the contribution of the surface tension gradient term in Equation 5.11 is zero.

## Nanowire Surface

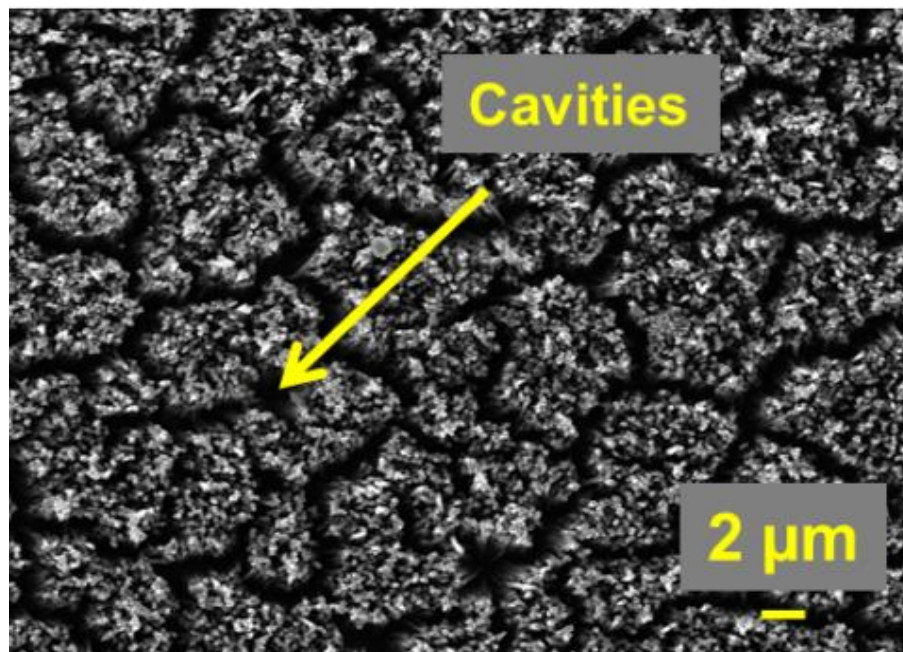


Figure 5.25: Cavities on a nanowire (200 nm diameter, 20  $\mu\text{m}$  tall) coated surface

**Near field:** The near field mechanism for CHF is due to the capillary pumping limit [61]. The nanostructures provide a large capillary force to bring the liquid back to the surface and delay the CHF. The CHF is estimated by the balance between the capillary pumping

force and the liquid viscous drag along its flow path. The CHF based on this mechanism is given by [61]:

$$\frac{q_{CHF-c}''}{0.53\varepsilon_s \left( \frac{\rho\sigma h_{fg}}{\mu} \right) \left( \frac{\sqrt{K\phi_s}}{D} \right)} = 1 - \frac{C_E}{(0.53\varepsilon_s^2)} \frac{D}{\sqrt{\phi_s}} \frac{(q_{CHF-c}'')^2}{\rho\sigma h_{fg}^2} \quad (5.12)$$

where K is the permeability of the porous structure,  $\phi_s$  is the porosity of the nanowire subarray,  $C_E$  is the Ergun coefficient (which is a function of  $\phi_s$  alone), D is the height of the nanostructures, representing each bundle of nanowires separated by the cavities;  $\varepsilon_s$  is the nanowire packing configuration.

The CHF values estimated using Zuber's correlation for a plain surface, near field and far field mechanisms on a nanowire (200 nm diameter, 8  $\mu$ m tall) coated surface are shown in Table 5.2 for a few mixtures. It is assumed that within the porous layer coating, the mixture behaves like a pure fluid with the same thermophysical properties as that of the mixture. Based on this assumption, for pool boiling of different fluids on the same enhanced surface, the enhancement in the CHF is only due to enhanced thermal properties of the fluid. From this table, it can be observed that the CHF based on near field mechanism is lower than the CHF based on far field mechanism and hence, near field mechanism is the dominant mechanism for the occurrence of CHF on nanowire coated surface. Also, it can be observed that all the fluid mixtures have a higher CHF than the base fluid (HFE 7200). Pool boiling experiments on different nanostructured surfaces showed a similar trend (where the mixture considered for the study had a higher CHF than HFE 7200) and CHF values comparable to the predictions.



Table 5.2: CHF Predictions

Fluid	$q''_{CHF_z}$ (W/cm <sup>2</sup> )	$q''_{CHF_f}$ (W/cm <sup>2</sup> )	$q''_{CHF_c}$ (W/cm <sup>2</sup> )
HFE 7200	17.6	455	27.6
HFE 7200 - Ethoxybutane	20.4	537	32.8
HFE 7200 - Methanol	51.3	1380	117.5
HFE 7200 - C <sub>6</sub> H <sub>11</sub> F <sub>3</sub>	18.5	483	31.3
HFE 7200 - C <sub>4</sub> H <sub>4</sub> F <sub>6</sub> O	17.8	461	27.6

### 5.8 Summary

In this chapter, the details of the pool boiling experimental setup were discussed. The important components of the test setup were identified and the test chip fabrication process was described in detail. The experimental procedure and the measurement uncertainty were discussed. Pool boiling experiments were performed using various fluid mixtures on enhanced surfaces. CHF was predicted for higher mixture concentrations using existing correlations. The CHF correlations for pool boiling of pure fluid on enhanced surface, and pool boiling of binary mixture on plain surface were grouped together to predict the CHF for far field mechanism. The important observations of this study are as follows:

- 1) All the enhanced surfaces tested showed an improvement in the CHF when compared to plain surface. Also, the wall superheat at the ONB was lower for the enhanced surfaces when compared to the plain surface.
- 2) All the mixtures considered for the pool boiling experiments (except  $C_4H_{11}N$ ) showed a significant improvement in the CHF when compared to pure HFE 7200. Both positive and negative mixtures showed an improvement which implies that there might be mechanisms other than Marangoni effect which might be responsible for this enhancement. CHF depends on several fluid properties and the improvement in the thermal properties of the mixture over pure HFE 7200 could also play a significant role in this enhancement.
- 3) Because of synthesis and economic constraints, the pool boiling performance of new fluids could not be evaluated at higher concentrations. However, the CHF predictions for pool boiling on an infinite heater and a small heater ( $10 \times 10 \text{ mm}^2$ ) show that the CHF increases as the mixture concentration increases. This improvement is significant for a small heater than an infinite heater.
- 4) The CHF predictions show that near field mechanism is the dominant mechanism leading to the CHF for pool boiling of liquid mixtures on porous surfaces.

## CHAPTER 6

### POOL BOILING SIMULATIONS

A computational model using the phase field method has been developed to simulate saturated pool boiling from artificial cavities on a horizontal surface. Simulations were carried out for two fluids: HFE 7200 and  $C_4H_4F_6O$ , using finite element based software COMSOL Multiphysics<sup>TM</sup>. The need for these numerical simulations, theory of the phase field method, computational model used for the simulations and the simulation results are discussed in this chapter.

#### 6.1 Need for Numerical Simulations

Pool boiling experimental results and the theoretical predictions show that new heat transfer fluids have the potential to significantly enhance heat transfer over pure HFE 7200. This enhancement could be due to the improved thermal properties of new fluids over HFE 7200. Fluid properties affect parameters including bubble departure diameter and departure frequency, which play a critical role in boiling heat transfer. High speed visualization is necessary to estimate these parameters experimentally, and this could aid in understanding the mechanism behind the heat transfer enhancement.

High speed visualization of the pool boiling process was performed using a Phantom v210 color camera. The images taken at heat fluxes close to the ONB and the CHF, for saturated boiling of pure HFE 7200 are shown in Figures 6.1 and 6.2 respectively. Although these images help visualize phenomena like bubble coalescence, vapor mushroom formation at high heat fluxes etc., it is not possible to accurately estimate the bubble departure diameters, departure frequency because of constraints

imposed by the experimental setup. Simulating the pool boiling process might be an alternative to estimate these parameters, provided these simulations are reliable and accurate. Some of the advantages these simulations might provide are:

- Supplement experimental observations by providing an insight into the critical boiling parameters including bubble departure frequency, bubble departure diameter, and bubble coalescence.
- Pool boiling performance of thousands of candidate fluids generated using the CAMD approach can be analyzed, which might not be possible through experiments because of synthesis, economic and time constraints.
- Pool boiling of mixtures can be analyzed, where surface tension gradients due to temperature differences and concentration differences are important.

For several years, two phase flows have been simulated using various methods such as the Level Set [62-67], Volume-of-fluid [68-72], front tracking [73-76], and Lattice Boltzmann [77-81]. Among these, Volume-of-fluid (VOF) and Level Set (LS) methods have been very popular and extensively employed because of their wide range of applicability. In the LS method, the interface is represented by a level set function, which is a signed distance function. This method is conceptually simple, can handle topological changes of the interface, and the curvature of the interface can be computed easily. However, one disadvantage of this method is that mass conservation is often violated. In the VOF method, the interface is represented by a volume fraction function for the liquid phase in each computational cell. Although the VOF method has excellent mass conservation properties, the interface reconstruction is difficult and lacks accuracy.

Hybrid methods [82-85] have been proposed to take advantages of both these methods, however, their implementation is not straightforward.

Phase field method (PFM) is an attractive alternative to the above methods for simulating two phase flows. PFM is a free energy based formulation in which the interface between two phases is represented by a finite thickness transition region. This method can handle moving interfaces easily, and also has good energy conservation properties. The advantages of PFM over other methods have been discussed in detail in the literature [86, 87]. Because of these attractive features, PFM was chosen for the pool boiling simulations.

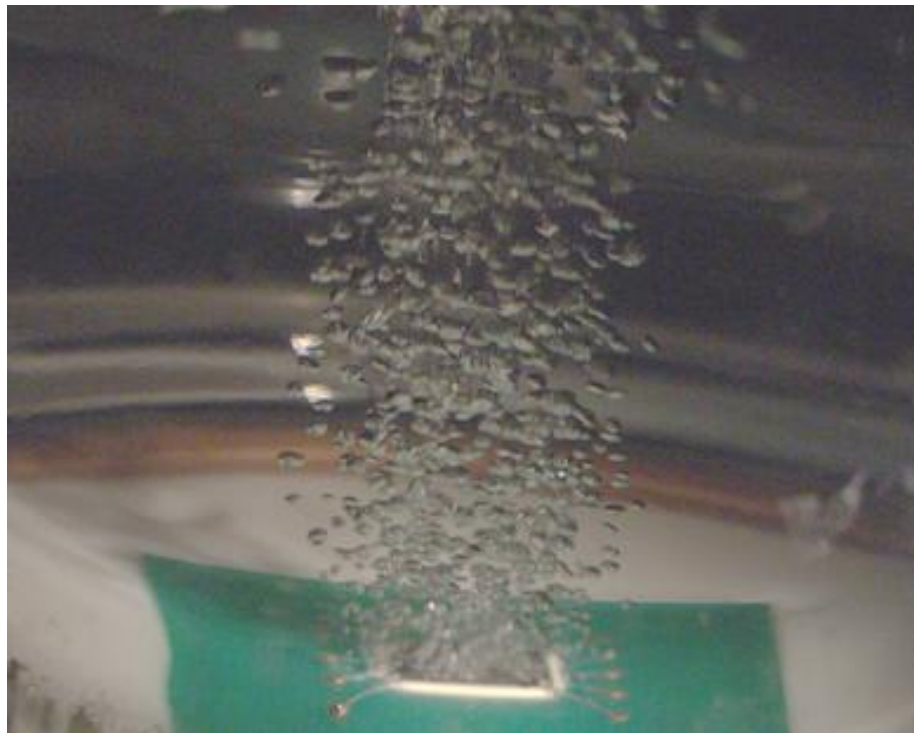


Figure 6.1: Saturated pool boiling of HFE 7200 at  $2.5 \text{ W/cm}^2$  (2000 fps)

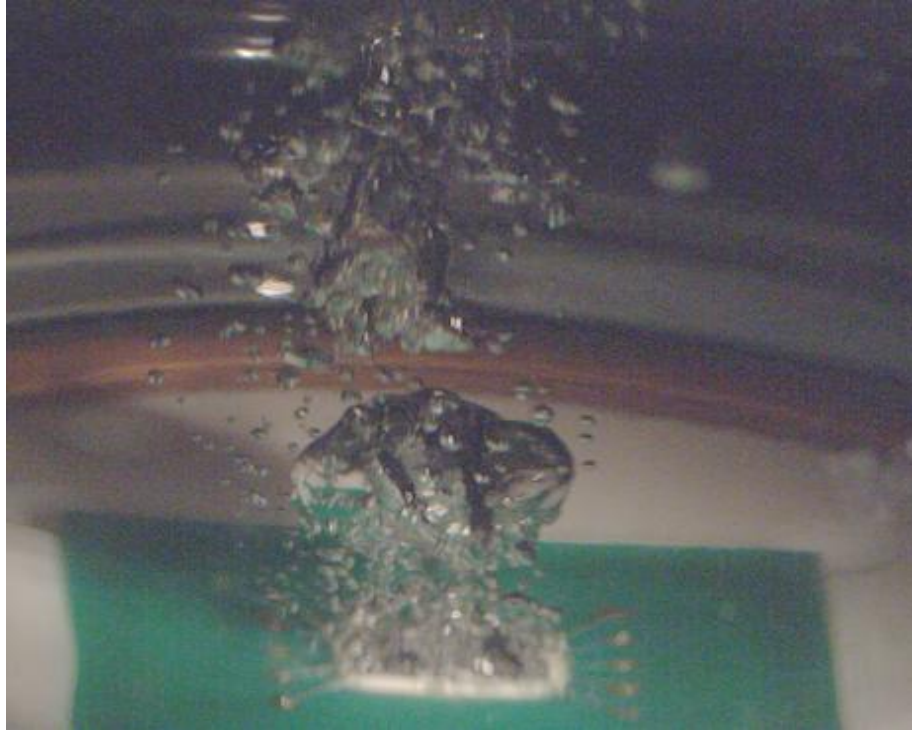


Figure 6.2: Saturated pool boiling of HFE 7200 at  $19.5 \text{ W/cm}^2$  (2000 fps)

## 6.2 Phase Field Method

PFM is a diffuse interface tracking method that simulates two-phase flows on a fixed Eulerian grid. The sharp interface between the two immiscible phases is replaced by a finite thickness region, across which the physical properties vary continuously. A non-conserved order parameter called the phase field ( $\phi$ ) is introduced to characterize the two phases. This dimensionless phase field variable assumes constant values in each of the bulk phases (+1 in one of the bulk phases and -1 in the other bulk phase), and is smoothly distributed across the interface ( $-1 \leq \phi \leq 1$ ). The system evolution is driven by a minimization of free energy. The equations governing the transport of the interface and the fluid dynamics are discussed below.

### 6.2.1 Interface Equations

The transport of the diffuse interface between two phases is governed by the convective – diffusive, Cahn – Hilliard equation [88, 89] and is given by Equation 6.1. This equation not only convects the interface but also ensures that the total free energy of the system is minimized.

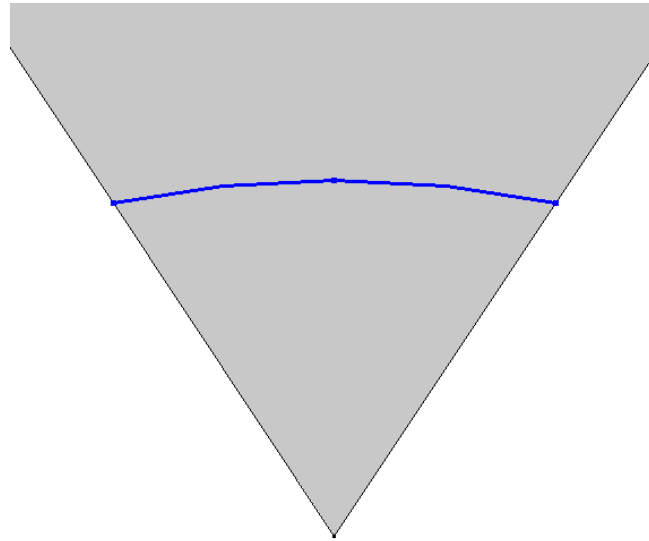
$$\frac{\partial \phi}{\partial t} + \mathbf{u} \cdot \nabla \phi - \dot{m} \delta \left( \frac{V_{f,v}}{\rho_v} + \frac{V_{f,L}}{\rho_L} \right) = \nabla \cdot \frac{\gamma \lambda}{\varepsilon^2} \nabla \psi \quad (6.1)$$

where  $V_{f,v}$  and  $V_{f,L}$  are the volume fractions of the vapor phase and the liquid phase respectively,  $\rho_v$  and  $\rho_l$  are the vapor and liquid densities respectively,  $\dot{m}$  is the mass flux due to phase change and  $\gamma$  is the mobility ( $\text{m}^3 \cdot \text{s}/\text{kg}$ ) that governs the stability of diffusive transport. This mobility value must be large enough so that the interfacial thickness remains constant, but small enough so that the convective terms are not overly damped. The quantity  $\delta$  is a smoothed representation of the interface between the two phases ( $0 \leq \delta \leq 1$ ) and is defined only at the interface. It assumes a constant value of zero in both the bulk phases. The quantity  $\lambda$  is the mixing energy density, and  $\varepsilon$  is a capillary width representative of the interface thickness (m). Both these terms are related to the surface tension by the equation [90],

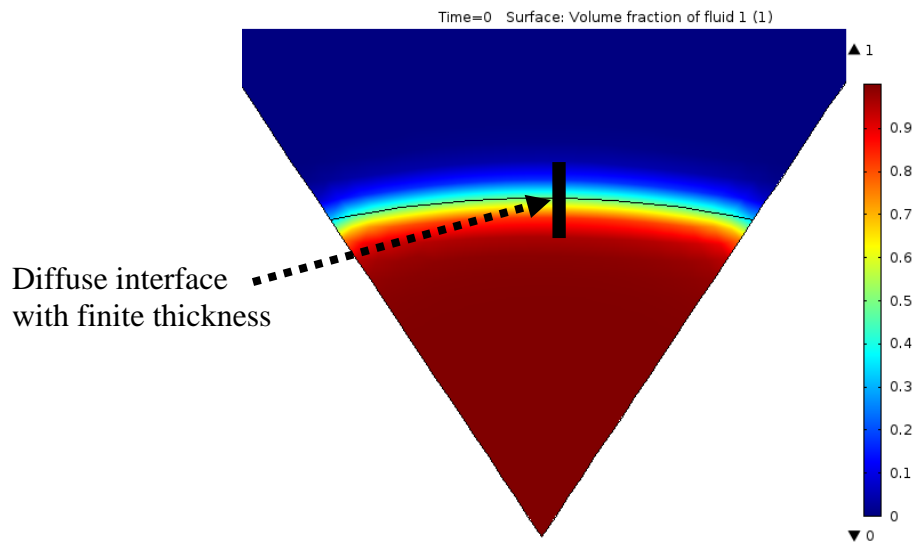
$$\sigma = \frac{2\sqrt{2}}{3} \frac{\lambda}{\varepsilon} \quad (6.2)$$

The variable  $\psi$ , in Equation 6.1 depends on the capillary width and the phase field variable and is given by,

$$\psi = -\nabla \cdot \epsilon^2 \nabla \phi + (\phi^2 - 1)\phi \quad (6.3)$$



(a)



(b)

Figure 6.3: Interface between two immiscible phases, a) Actual interface, and b) Diffuse interface in PFM



The actual interface and the diffuse interface in PFM are illustrated in Figure 6.3(a) and 6.3(b) respectively. It can be observed from Figure 6.3(b) that the thickness of the diffuse interface (shown by the solid black line) is greater than the actual interface thickness shown in Figure 6.3(a). The two phases and the interfaces between them are incorporated into the total free energy function of the system. For each time step, the total free energy ( $F$ ) of the system can be calculated in two different ways [89]:

a) The free energy function of the system is integrated over the entire computational domain to calculate the total free energy at any time instant.

$$F = \int \left( \frac{1}{2} \lambda |\nabla \phi|^2 + \frac{\lambda}{4\epsilon^2} (\phi^2 - 1)^2 \right) dV \quad (6.4)$$

b) The total free energy of the system can also be calculated by multiplying the surface tension coefficient with the total interface area ( $A_{\text{int}}$ ) at any time instant.

$$F = \sigma A_{\text{int}} \quad (6.5)$$

where the total interface area is given by

$$A_{\text{int}} = \int_V \delta dV \quad (6.6)$$

Any difference in the values of the total free energy calculated using the above two ways indicates a mass loss.

## 6.2.2 Conservation Equations

The mass conservation equation is given by,

$$\nabla \cdot \mathbf{u} = \dot{m} \delta \left( \frac{1}{\rho_v} - \frac{1}{\rho_L} \right) \quad (6.7)$$

The term on the right hand side accounts for phase change from liquid to vapor and is non-zero only at the interface. The fluid dynamics are governed by the Navier – Stokes equations,

$$\rho \frac{\partial \mathbf{u}}{\partial t} + \rho (\mathbf{u} \cdot \nabla) \mathbf{u} = \nabla \cdot \left[ -P \mathbf{I} + \eta \left( \nabla \mathbf{u} + (\nabla \mathbf{u})^T \right) \right] + \rho \mathbf{g} + G \nabla \phi \quad (6.8)$$

where  $\mathbf{u}$  is the fluid velocity field, P the pressure,  $\rho$  the density and  $\mathbf{g}$  the acceleration due to gravity. The surface tension force is introduced in the momentum equation as a body force by multiplying the chemical potential of the system by the gradient of the phase field variable [91]. The chemical potential (G) in the above equation is given by:

$$G = \lambda \left[ -\nabla^2 \phi + \frac{\phi(\phi^2 - 1)}{\varepsilon^2} \right] \quad (6.9)$$

The energy conservation equation is given by:

$$\rho c_p \frac{\partial T}{\partial t} + \rho c_p (\mathbf{u} \cdot \nabla) T = -\nabla \cdot \kappa \nabla T - \dot{m} \delta h_{fg} \quad (6.10)$$

where  $c_p$  is the specific heat and  $\kappa$  the thermal conductivity. Both these properties are computed in terms of the volume fraction of the two phases.

$$\kappa = (\kappa_l - \kappa_v) V_{f,l} + \kappa_v \quad (6.11)$$

$$C_p = (C_{p,l} - C_{p,v})V_{f,l} + C_{p,v} \quad (6.12)$$

The temperature of the interface is fixed at the saturation temperature for the simulations and as a result, the energy equation is solved only in the vapor phase. Neglecting the kinetic energies and work due to viscous forces, the mass flux leaving the interface can then be evaluated from the conductive heat flux [92]:

$$\dot{m} = -h_{fg} \mathbf{n} \cdot \kappa_v \nabla T_v \approx C \rho_l \frac{(T - T_{sat})}{T_{sat}} \quad (6.13)$$

where C is a constant (m/s). The value of C is arbitrary [89] and should be large enough so that the temperature at the interface remains at the saturation temperature. Choosing a low value of C might lead to numerical instabilities.

### 6.3 Pool Boiling Model

The computational model, and its boundary and initial conditions are described in this section. All the simulations were carried out on a cluster using 10 processors and 50 GB memory. ‘Boiling Water’ model [89], available in COMSOL library, was used as the reference for the implementation of PFM. These simulations require two physics modules in COMSOL [93]:

- **Laminar Two-Phase Flow, Phase Field (LTPF):** It is used to model laminar two-phase flow of two immiscible fluids separated by a moving interface. The velocity field, pressure and the phase field variables are the outputs of this module.

- **Heat Transfer in Fluids (HTF):** It is used to model heat transfer in fluid materials. Temperature is the output of this module.

### 6.3.1 Computational Model

The computational model consists of a 1 cm x 1 cm square enclosure with two artificial cavities at the bottom. The schematic of this model along with some key dimensions are shown in Figure 6.4. Each cavity has entrapped vapor to begin with, which serves as the nucleus for boiling incipience. The domains occupied by the liquid phase and the vapor phase initially are shown in Figure 6.5. The bottom wall of the enclosure is considered to be the heater surface.

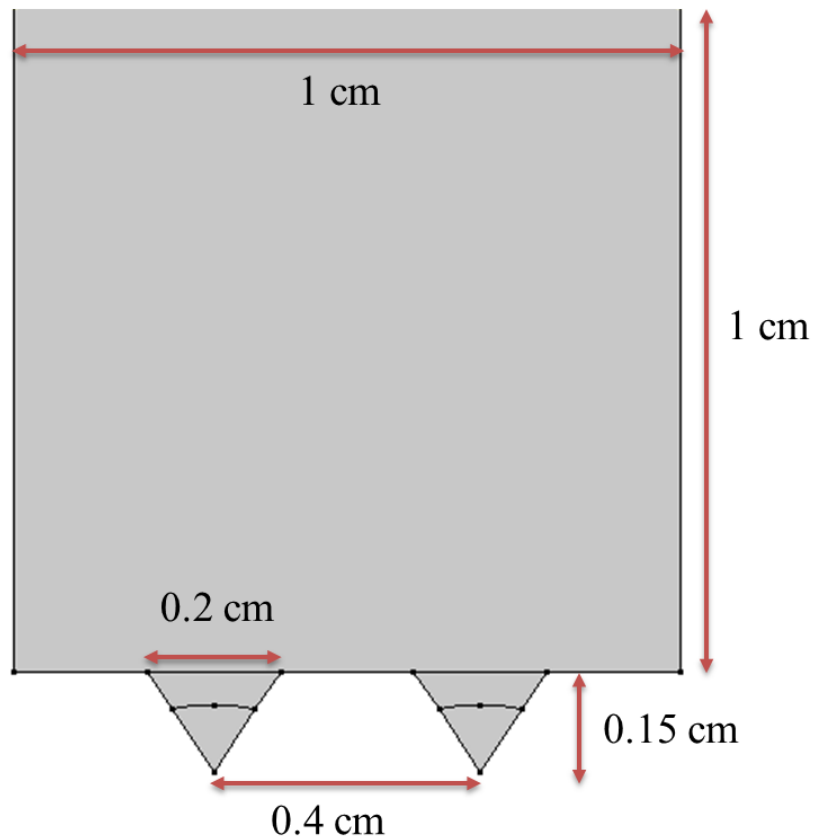


Figure 6.4: Computational model with key dimensions

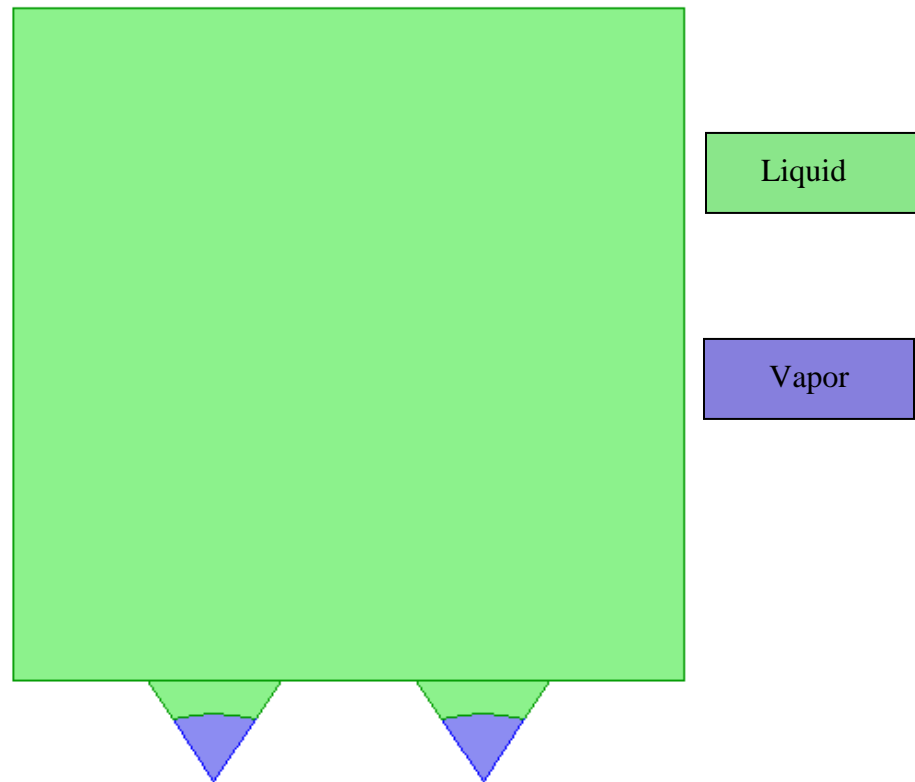


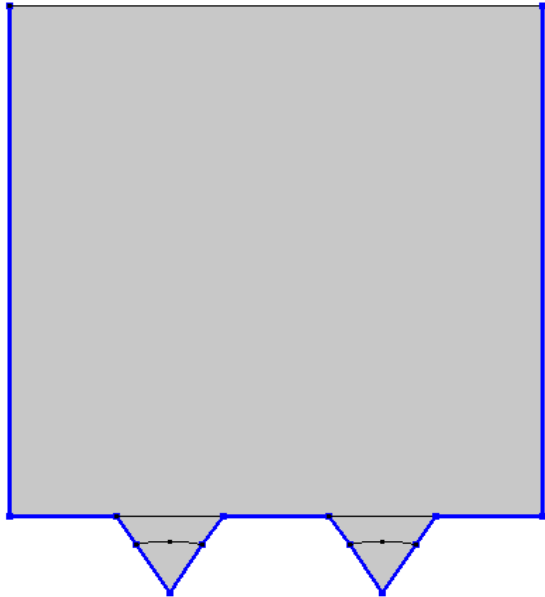
Figure 6.5: Domains occupied by the liquid and vapor phases initially

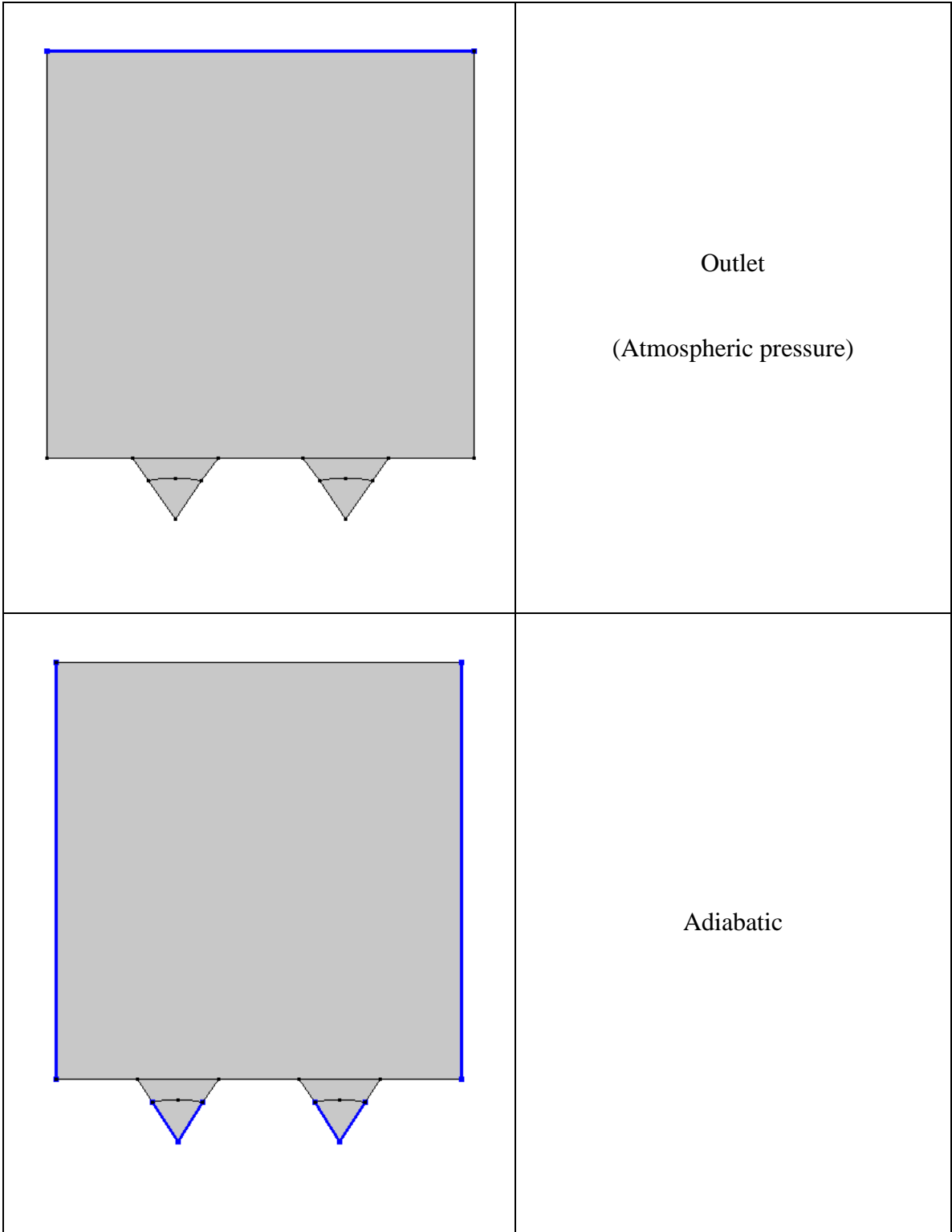
In general, the cavities on a real surface are smaller (few micrometers) than the ones shown in Figure 6.4. However, reducing the cavity size further would require higher mesh resolution within the cavities to capture the interface and is computationally intensive. Also, the simulations were numerically unstable and failed to converge at lower cavity sizes. This is because the solutions are grid-size dependent as will be discussed in section 6.4.1. Since the departure parameters are compared for two fluids, the same surface was used for simulations involving both the fluids.

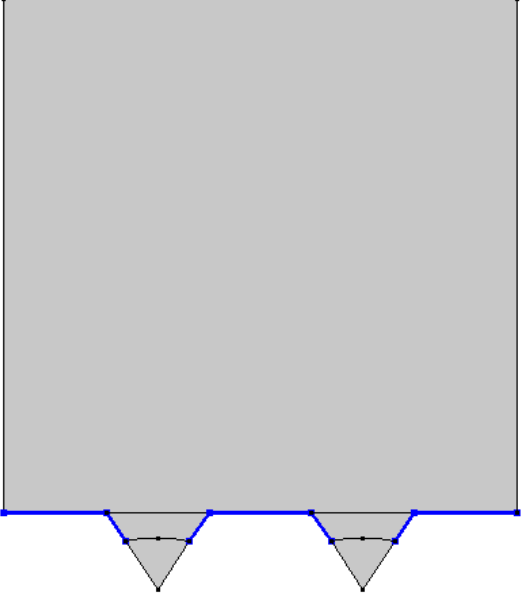
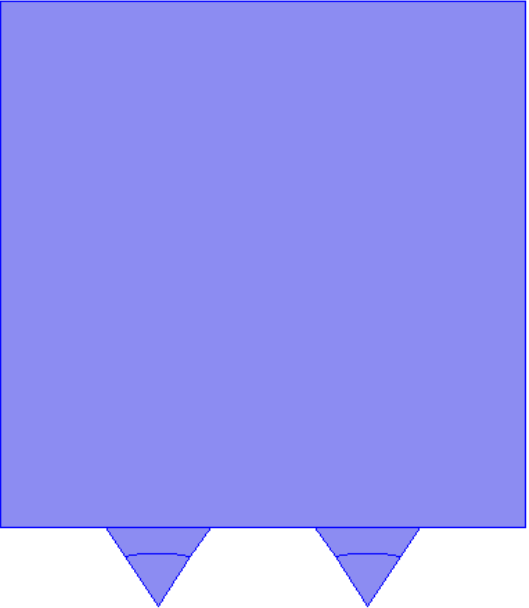
### 6.3.2 Boundary conditions

The boundary conditions and the initial conditions for the model are graphically shown in Table 6.1. The solid lines represent the boundaries where that particular boundary condition is applied. The shaded regions represent the domains where that particular initial condition is applied.

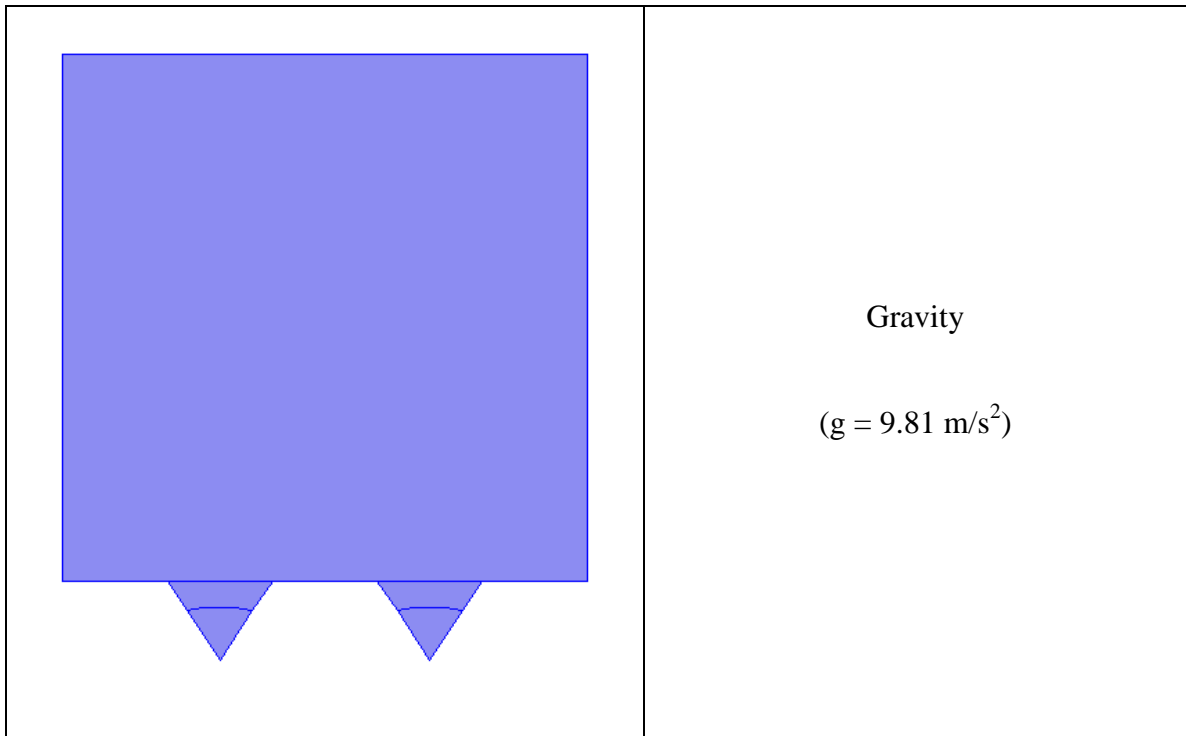
Table 6.1: Boundary conditions and initial conditions for the computational model

Domains/Boundaries	Boundary/Initial Conditions
	No-slip



	<p>Constant heat flux</p>
	<p><math>T = T_{\text{sat}}</math></p>



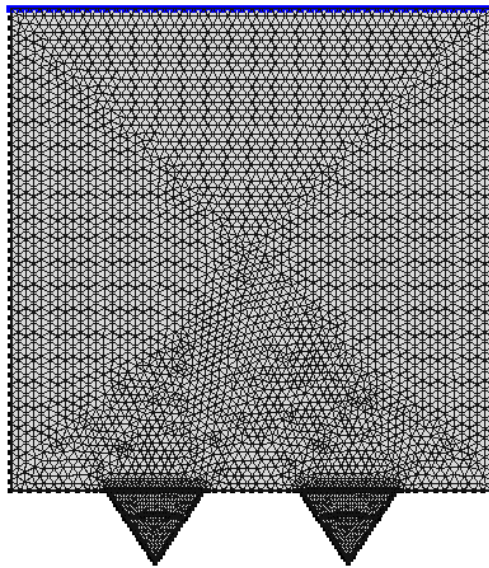


The vapor in the cavity reaches relatively high temperatures (exceeding 1000 K) if a constant heat flux boundary condition is prescribed for the entire heater surface. Hence, an adiabatic boundary condition was prescribed for the heater surface underneath the vapor bubble to limit the maximum temperature to 450 K. The liquid and the vapor have significantly different thermal properties, and as a result, the heat flux would not be uniform over the entire heater surface. The heater surface underneath the liquid would experience a significantly higher heat flux than the heater surface underneath the vapor. Although this heat flux under the vapor is non-zero and depends on the fluid properties, an adiabatic boundary condition was prescribed so as to be consistent for all the fluids. More accurate results can be obtained if a solid heater domain is incorporated in this model.

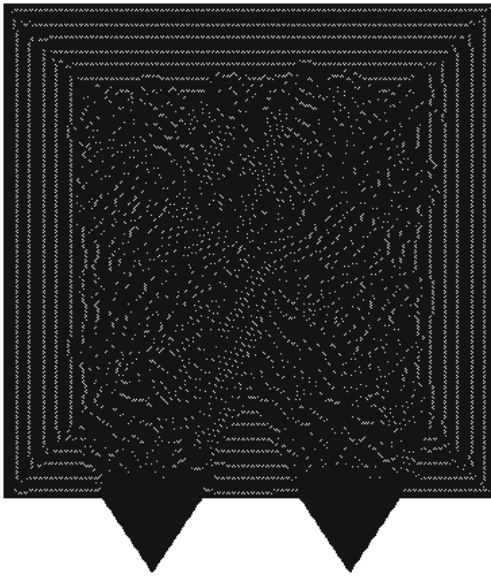
## 6.4 Simulation Results

### 6.4.1 Effect of Grid Size

Saturated pool boiling simulations were performed using pure HFE 7200 at two different mesh settings (Case 1 and Case 2) to evaluate the grid size dependence of the simulation results. Triangular elements were used to mesh the entire computational domain. The meshed model for Case 1 and Case 2 are shown in Figure 6.6. The cavities were meshed finer than the bulk enclosure as the initial interface lies within the cavity. Also, since the area of the bulk enclosure is significantly larger than the cavity area, meshing the bulk region coarser would reduce the computational time. The boiling process was simulated for 0.5 seconds with a time step of 0.01 seconds. The boundary and initial conditions shown in Table 6.1 were applied for these simulations. The heat flux was constant at  $10 \text{ W/cm}^2$ . The mesh statistics and the solution time are shown in Table 6.2.



(a)



(b)

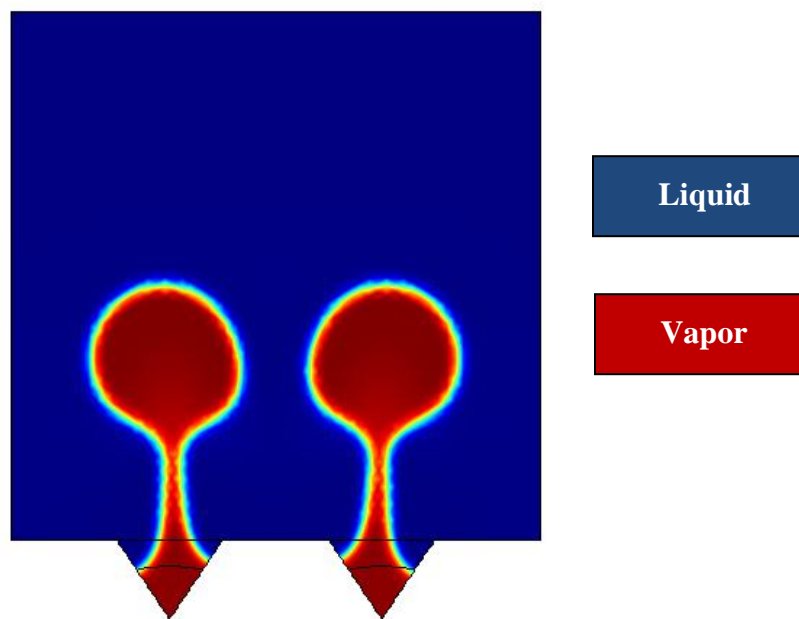
Figure 6.6: Mesh settings for a) Case 1, and b) Case 2

Table 6.2: Mesh statistics and solution time for grid size dependence study

	Triangular elements	Nodes	Solution time (hh:mm:ss)
Case 1	7,960	3,980	02:29:27
Case 2	53,719	26,860	33:20:34

The bubble departure diameter and departure frequency were compared for these models from the simulation results. The fluid volume fraction at each time step was stored as an image (frame). The Image Processing toolbox available in MATLAB was

used to measure the bubble departure diameter from these fluid volume fraction images. First, the images had to be calibrated to obtain a correlation between the pixels and the length. The mouth diameter of the cavity was used as the reference to obtain this correlation. The bubble departure frequency was calculated by counting the number of frames between successive bubble departures. The bubble departure diameters for Case 1 and Case 2 were 2.90 mm and 2.95 mm respectively. The bubble departure frequencies for Case 1 and Case 2 were 2.44 Hz and 2.86 Hz respectively. From these results it can be inferred that the grid settings did not have a significant impact on the bubble departure diameter, but there is a considerable difference in the bubble departure frequency. The fluid volume fraction images captured just before the bubble departure are shown in Figure 6.7 for both the cases. It can be observed from these images that there is no significant change in the bubble departure diameter. However, the interface representation is smooth for Case 2 because of higher mesh resolution. Also, the computation time is significantly higher (13 times) for Case 2 than Case 1.



(a)

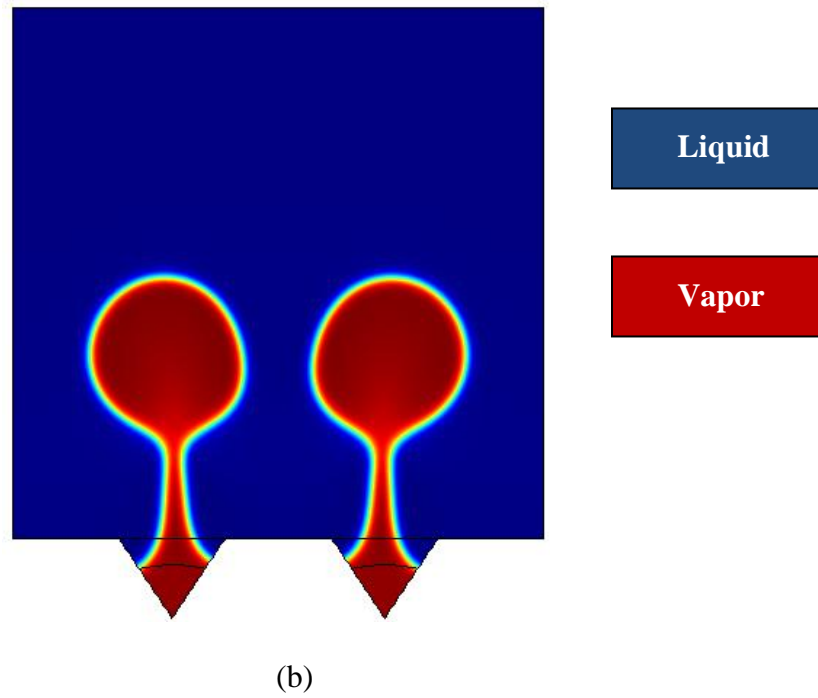


Figure 6.7: Fluid volume fraction plots before bubble departure for a) Case 1, and b) Case 2

#### 6.4.2 Simulations using HFE 7200 and $C_4H_4F_6O$

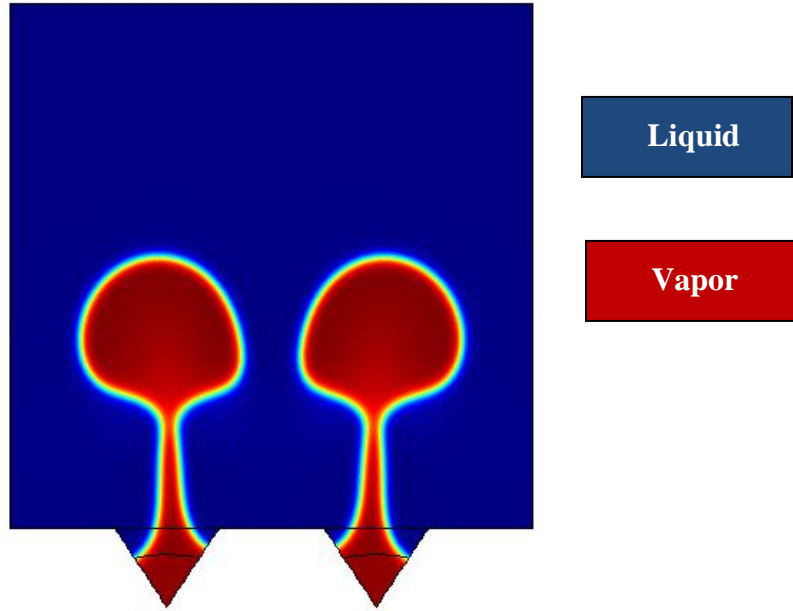
Saturated pool boiling simulations were performed using HFE 7200 and  $C_4H_4F_6O$  to compare the bubble departure parameters for these fluids. The fluid properties used for these simulations are shown in Table 6.3. Triangular elements were used to mesh the entire computational domain. The cavities were meshed finer than the bulk enclosure as the initial interface lies within the cavity. The simulation was performed for 0.5 seconds with a time step of 0.01 seconds. The boundary and initial conditions shown in Table 6.1 were applied for these simulations. The heat flux was constant at  $10 \text{ W/cm}^2$ . The mesh statistics and the solution time are shown in Table 6.4

Table 6.3: Properties of heat transfer fluids considered for simulations

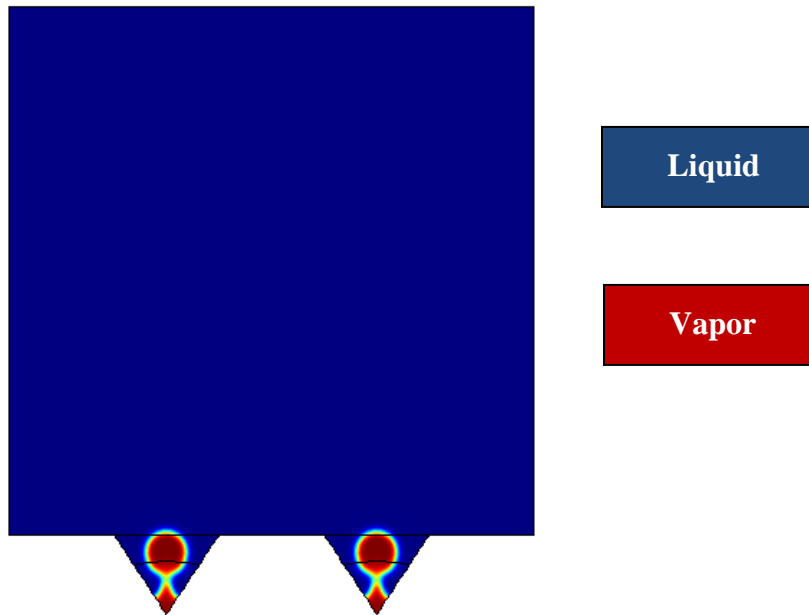
Property	HFE 7200	C <sub>4</sub> H <sub>4</sub> F <sub>6</sub> O
T <sub>b</sub> (K)	349	335.7
h <sub>fg</sub> (kJ/kg)	119	137.8
ρ <sub>l</sub> (kg/m <sup>3</sup> )	1420	1404
k <sub>l</sub> (W/m-K)	0.069	0.083
k <sub>v</sub> (W/m-K)	0.01097	0.01264
c <sub>p,l</sub> (J/kg-K)	1220	1252.4
c <sub>p,v</sub> (J/kg-K)	876.8	887.5
μ <sub>l</sub> (kg/m-s)	0.000629	0.00056
μ <sub>v</sub> (kg/m-s)	0.000009	0.0000101
σ (mN/m)	13.6	17.8

Table 6.4: Mesh statistics and solution time for different fluids

Fluid	Triangular elements	Nodes	Solution time (hh:mm:ss)
HFE 7200	28,073	14,037	11:02:18
C <sub>4</sub> H <sub>4</sub> F <sub>6</sub> O	28,073	14,037	14:12:21



(a)



(b)

Figure 6.8: Fluid volume fraction plots before bubble departure for a) HFE 7200, and b)  $C_4H_4F_6O$

The bubble departure diameter and departure frequency were compared for both the fluids from the simulation results. The bubble departure diameters for pure HFE 7200 and pure C<sub>4</sub>H<sub>4</sub>F<sub>6</sub>O were 2.95 mm and 0.80 mm respectively. The bubble departure frequencies for pure HFE 7200 and pure C<sub>4</sub>H<sub>4</sub>F<sub>6</sub>O were 2.8 Hz and 20 Hz respectively. The fluid volume fraction images captured just before the bubble departure for both the cases are shown in Figure 6.8. From these results it can be inferred that the bubble departure diameter is significantly lower for C<sub>4</sub>H<sub>4</sub>F<sub>6</sub>O than HFE 7200. Also, the departure frequency was higher for C<sub>4</sub>H<sub>4</sub>F<sub>6</sub>O than HFE 7200. Another interesting thing to note is that, for pool boiling of C<sub>4</sub>H<sub>4</sub>F<sub>6</sub>O, the entrapped vapor serves as the nucleus for vapor bubbles for only two cycles. Thereafter, boiling was not observed from the cavities, as there was no entrapped vapor to form the vapor bubbles.

The bubble departure diameter calculated from the simulations was compared to correlations of bubble departure diameter given by Fritz [94], and Cole and Rohsenow [95]. The bubble departure frequency calculated from the simulations was compared to correlations of bubble departure frequency given by Zuber [58] and Malenkov [96]. These comparisons for the bubble departure diameter and departure frequency are shown in Tables 6.5 and 6.6 respectively.

Fritz correlation [94] for bubble departure diameter

$$D_d = 0.0208\theta \sqrt{\frac{\sigma}{g(\rho_l - \rho_v)}} \quad (6.14)$$

where  $\theta$  is the contact angle measured in degrees. The contact angle was measured from the images shown in Section 4.2 using MATLAB.



Cole and Rohsenow [95] correlation for bubble departure diameter

$$D_d = 4.65 \times 10^{-4} \left( \frac{\rho_l c_{p,l} T_{sat}}{\rho_v h_{fg}} \right)^{5/4} \sqrt{\frac{\sigma}{g(\rho_l - \rho_v)}} \quad (6.15)$$

Zuber correlation [58] for bubble departure frequency

$$fD_d = 0.59 \left[ \frac{\sigma g(\rho_l - \rho_v)}{\rho_l^2} \right]^{1/4} \quad (6.16)$$

Malenkov correlation [96] for bubble departure frequency

$$fD_d = \frac{V_d}{\pi \left( 1 - \frac{1}{1 + V_d \rho_v h_{fg} / \dot{q}} \right)} \quad (6.17)$$

where 
$$V_d = \left[ \frac{D_d g(\rho_l - \rho_v)}{2(\rho_l + \rho_v)} + \frac{2\sigma}{D_d(\rho_l + \rho_v)} \right]^{1/2}$$

Table 6.5: Comparison between theoretical predictions and simulations for the bubble departure diameter

Fluid	Bubble departure diameter (mm)		
	Fritz Correlation	Cole and Rohsenow Correlation	Simulation
HFE 7200	0.454	0.928	2.95
C <sub>4</sub> H <sub>4</sub> F <sub>6</sub> O	0.522	1.42	0.80

Table 6.6: Comparison between theoretical predictions and simulations for the bubble departure frequency

Fluid	Bubble departure frequency (Hz)		
	Zuber Correlation	Malenkov Correlation	Simulation
HFE 7200	62.4	54.16	2.8
C <sub>4</sub> H <sub>4</sub> F <sub>6</sub> O	43.8	35.2	20

It can be observed from Tables 6.5 and 6.6 that the bubble departure diameter and departure frequency calculated from the simulations were almost of the same order of magnitude as the theoretical predictions, for C<sub>4</sub>H<sub>4</sub>F<sub>6</sub>O. However, the simulation results and the theoretical predictions do not match for HFE 7200. Possible reasons for this discrepancy are discussed in the next section.

### 6.4.3 Possible Reasons for Discrepancy

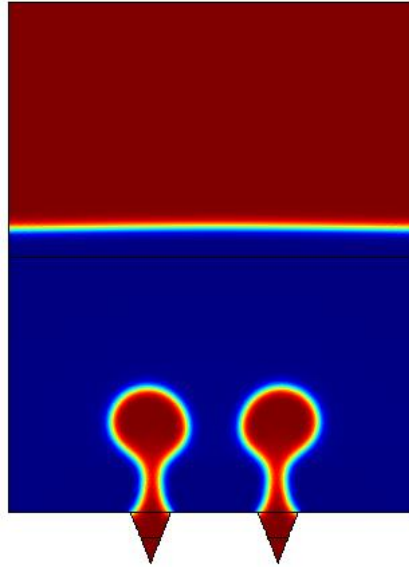
The large deviation between the simulation results and the theoretical predictions for HFE 7200 could be because of several reasons listed below:

- The constant 'C' in the equation for mass flux has been calibrated in the literature for only water. As there are no experimental results available in the literature for HFE 7200 and  $C_4H_4F_6O$ , this constant could not be calibrated and the same value (0.01 m/s) was used for simulations of both the fluids. This could possibly be one reason for the deviation between the theoretical and simulation results.
- Several stabilization parameters for maintaining interfacial thickness, isotropic diffusion constant etc. could play an important role in the simulation results. At present, the values for these parameters are chosen arbitrarily to provide a numerically stable solution. Also, the solutions are grid size dependent.
- This model does not take into account the heat transfer in the microlayer, which plays an important role in boiling heat transfer. This microlayer region is very thin and high mesh resolution would be required to capture these effects. This microlayer heat transfer sub-model could be incorporated into the present model to obtain accurate results.
- Adiabatic boundary condition has been prescribed for the heater surface under the vapor bubble. In reality, this heat flux is non-zero and depends on the fluid thermal properties. A solid heater domain has to be incorporated in this model to accurately estimate the heat flux distribution under the vapor bubble and the liquid.

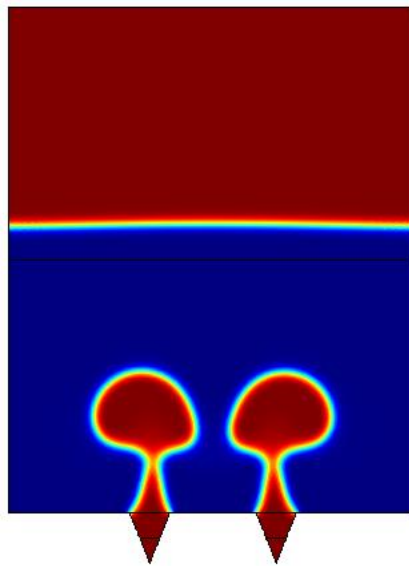
#### 6.4.4 Effect of Constant ‘C’ on Simulation Results

To determine the effect of constant  $C$  on the simulation results, pool boiling simulations were performed for different values of  $C$  at saturation condition. This constant has been calibrated in the literature for water [89] and therefore, simulations were carried out using water as the test fluid. The heat flux was constant at  $10 \text{ W/cm}^2$ . The boundary and initial conditions shown in Table 6.1 were applied for these simulations. The fluid volume fraction images captured just before the bubble departure are shown in Figure 6.9.

The bubble departure parameters were compared for two different cases (Case 1:  $C = 0.005 \text{ m/s}$ , and Case 2:  $C = 0.1 \text{ m/s}$ ). The bubble departure diameters for Case 1 and Case 2 were  $0.80 \text{ cm}$  and  $1.05 \text{ cm}$  respectively. The bubble departure frequency for Case 1 and Case 2 were  $3.7 \text{ Hz}$  and  $6.25 \text{ Hz}$  respectively. It can be observed from these results that the bubble departure diameter increases as  $C$  increases. The mass flux is directly proportional to the constant  $C$ , and therefore the vapor production rate increases as  $C$  increases. This could possibly be the reason for the increase in the bubble departure frequency and bubble departure diameter, as  $C$  increases. These results show that the constant  $C$  plays a significant role in the simulation results. The value of  $C$  has to be calibrated for each fluid by comparing the simulation results with the experimental observations for the bubble departure parameters.



(a)

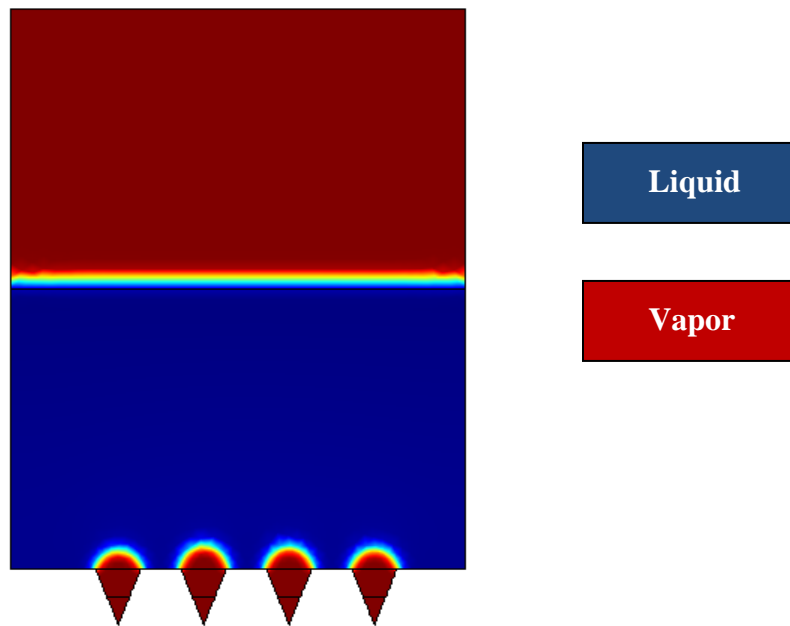


(b)

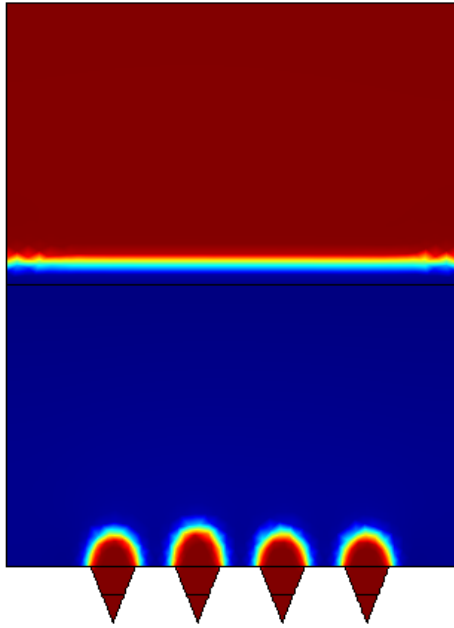
Figure 6.9: Fluid volume fraction plots before bubble departure for a)  $C = 0.005$  m/s and b)  $C = 0.1$  m/s

## 6.5 Validation with Experimental Results

Pool boiling simulations were carried out using water as the test fluid to validate the simulation results with experimental results. Simulations were carried out at different heat fluxes ( $1 \text{ W/cm}^2$ ,  $4 \text{ W/cm}^2$ ,  $6 \text{ W/cm}^2$  and  $8 \text{ W/cm}^2$ ), and the heat flux corresponding to the ONB was compared to the values observed experimentally in the literature for pool boiling of water on plain surface. The computational model consists of four artificial cavities with entrapped vapor. The boundary and initial conditions shown in Table 6.1 were applied for these simulations. The fluid volume fraction images captured just before the bubble departure are shown in Figure 6.10.



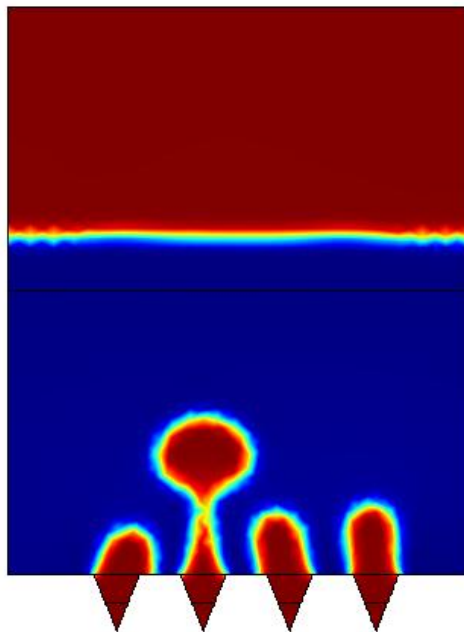
(a)



Liquid

Vapor

(b)



Liquid

Vapor

(c)

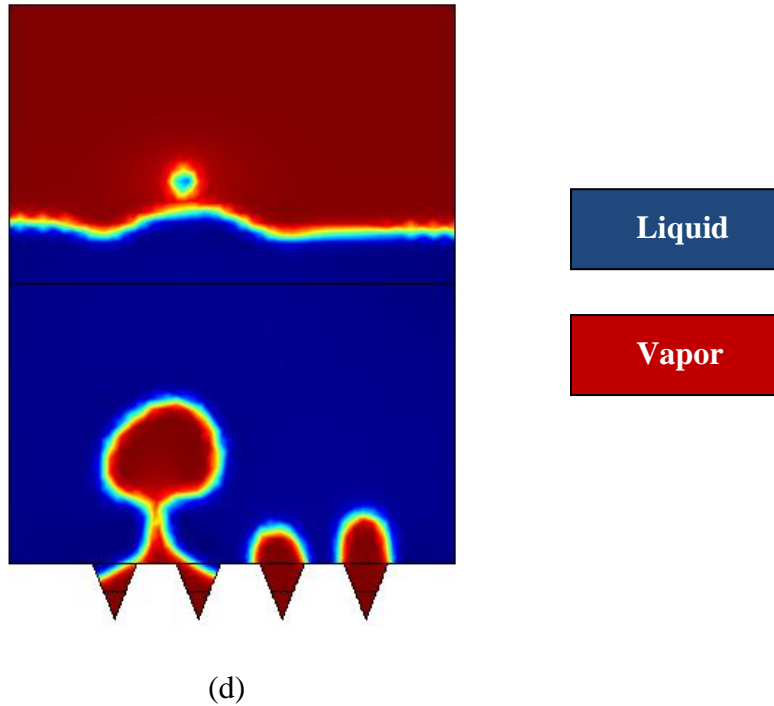


Figure 6.10: Fluid volume fraction plots before bubble departure for a)  $q'' = 1 \text{ W/cm}^2$ , b)  $q'' = 4 \text{ W/cm}^2$ , c)  $q'' = 6 \text{ W/cm}^2$ , and d)  $q'' = 8 \text{ W/cm}^2$

From the above images, it can be observed that for heat fluxes of  $1 \text{ W/cm}^2$  and  $4 \text{ W/cm}^2$ , bubbles do not depart from the heater surface. Although the bubbles grew in size, the buoyancy forces might not have been sufficient to overcome the surface tension forces holding the bubble against the heater surface. The bubbles first depart from the heater surface at a heat flux of  $6 \text{ W/cm}^2$ . It can be concluded from these simulations that the heat flux corresponding to the ONB could be between  $4 - 6 \text{ W/cm}^2$ . This heat flux is of the same order of magnitude as the experimental values reported in the literature [97-101].



## 6.6 Summary

In this chapter, pool boiling model developed using the phase field method was discussed. The effect of grid size on the simulation results was investigated. Pool boiling simulations were performed using pure HFE 7200 and  $C_4H_4F_6O$ , and the simulation results are discussed. The main observations from this study are listed below:

- 1) Increasing the grid size did not have any effect on the bubble departure diameter, but there was a considerable change in the bubble departure frequency.
- 2) The simulation results were comparable to the theoretical predictions for  $C_4H_4F_6O$ . However, for HFE 7200 the deviation between the simulation results and the theoretical predictions were significant.
- 3) The discrepancy between the simulation results and theoretical predictions could be because of several reasons, and were discussed in detail. They have to be addressed in order to use this model as a supplement to experimental observations.
- 4) The constant  $C$  could play a significant role in the simulation results. Parametric study showed an increase in the bubble departure frequency and bubble departure diameter as  $C$  increases.

## **CHAPTER 7**

### **FLOW BOILING EXPERIMENTS**

Pool boiling experiments with various fluid mixtures showed an improvement in the heat transfer performance when compared to HFE 7200. The FOM predictions show that all these fluids would improve the heat transfer under flow boiling conditions as well. To investigate this, flow boiling experiments were performed using HFE 7200 and 20 wt. % mixture of HFE 7200 – methanol. An experimental system was designed and constructed to perform flow boiling experiments in a microgap channel. The details of the flow boiling experimental setup, microgap channel test section and experimental results using two fluids are discussed in this chapter.

#### **7.1 Experimental Setup**

The flow boiling experimental setup consists of a liquid reservoir, gear pump, flow meter, inline filter, preheater, microgap channel test section and a condenser. The schematic of the experimental setup is shown in Figure 7.1. A Borosilicate glass 3.3 of 1000 ml capacity, fitted with a Schott GL 45 cap was used as the liquid reservoir. The cap had four ports out of which two ports were used to monitor the pressure and liquid temperature in the reservoir. The other two ports served as the inlet and outlet for fluid flow. The reservoir served as a constant pressure reference for the flow loop. The liquid temperature in the reservoir was monitored using a T-type thermocouple (Omega™ TMQSS-062G-6) and the reservoir pressure was monitored using an analog pressure gauge (Omega™ PGC-25L-30V/30). The reservoir was placed on a hot plate heater and

the liquid temperature in the reservoir was controlled by adjusting the hot plate heater temperature settings.

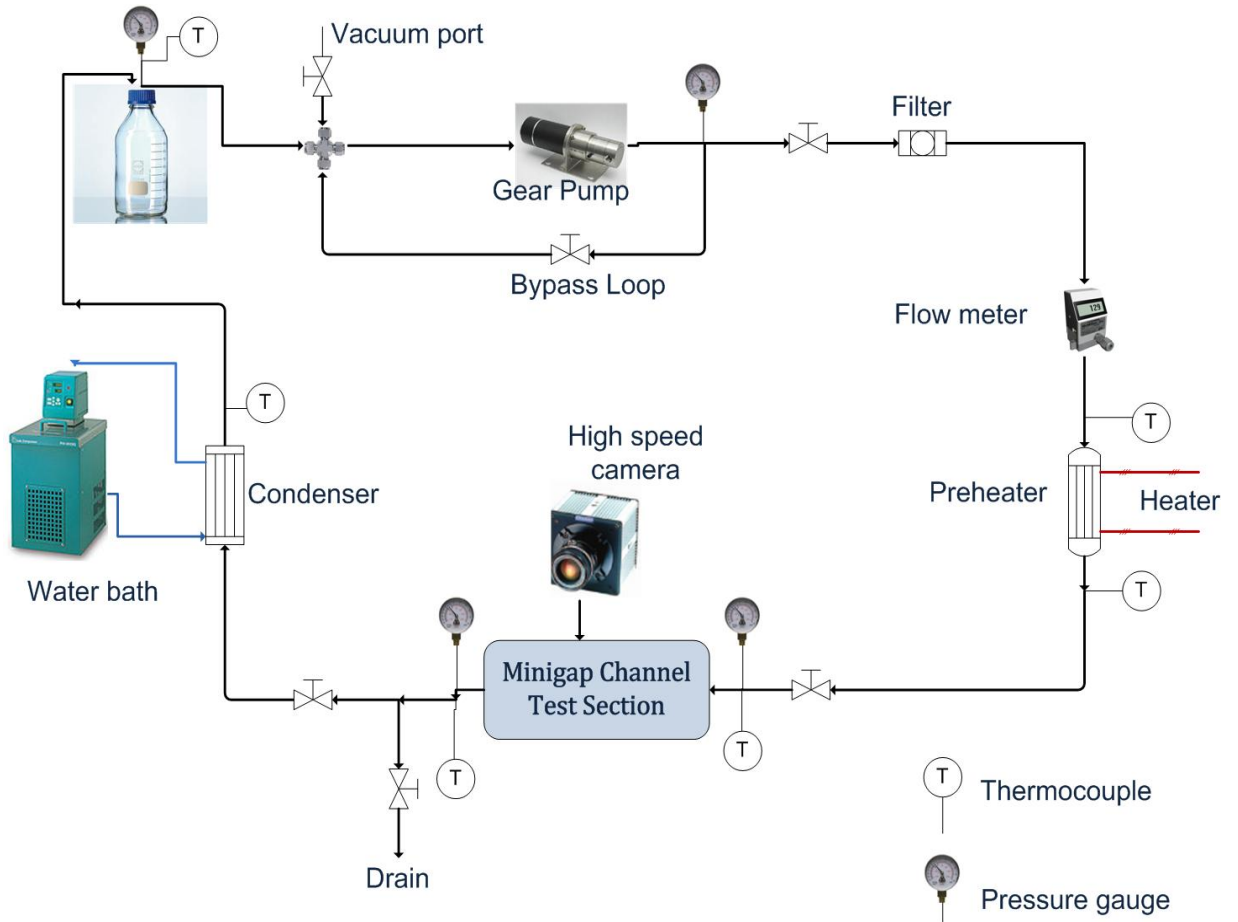


Figure 7.1: Schematic of the flow boiling experimental setup

The test fluid was pumped from the reservoir and circulated through the flow loop using a magnetic gear pump (Micropump, Model: L21836). The pressure at the exit of the pump was monitored using a pressure gauge (Omega™ PX209). A Swagelok in-line particulate filter (7  $\mu\text{m}$  pore size) located downstream from the pump was used to remove any contaminants present in the test fluid. The flow rate of the fluid in the loop was

monitored using a flow meter (McMillan S-112). The flow rate can be controlled precisely during the experiments using the bypass loop. A resistance wire (Hyndman 1/16X.0031N6RIB) wound around the copper tube served as the preheater. A DC power supply (Agilent E3645) connected to this resistance wire was used to control the liquid temperature exiting the preheater. Two T-type thermocouples located immediately before and after the preheater were used to monitor the fluid temperature.

Since the test fluids are very volatile, bellow valves were chosen for the flow loop so that the fluid does not seep along the valve stem and escape. Two control valves located upstream and downstream of the test section were used to regulate the flow during the experiments. The vapor in the two-phase mixture exiting the test section was condensed using a liquid-to-liquid heat exchanger (Lytron LL520G12). Water circulated from a constant temperature bath, was used as the coolant in the heat exchanger. The temperature of the test fluid exiting the condenser was monitored using a T-type thermocouple. The test fluid exiting the condenser then entered the reservoir, forming a closed flow loop.

A vacuum port is also provided in the flow loop. This port was used to evacuate air from the flow loop before charging it with the test liquid. A drain valve located immediately after the test section was used to calibrate the flow meter for different fluids, without having to disassemble it from the flow loop. This valve can also be used to evacuate test fluid from the loop in case of an emergency.

## **7.2 Microgap Channel Test Section**

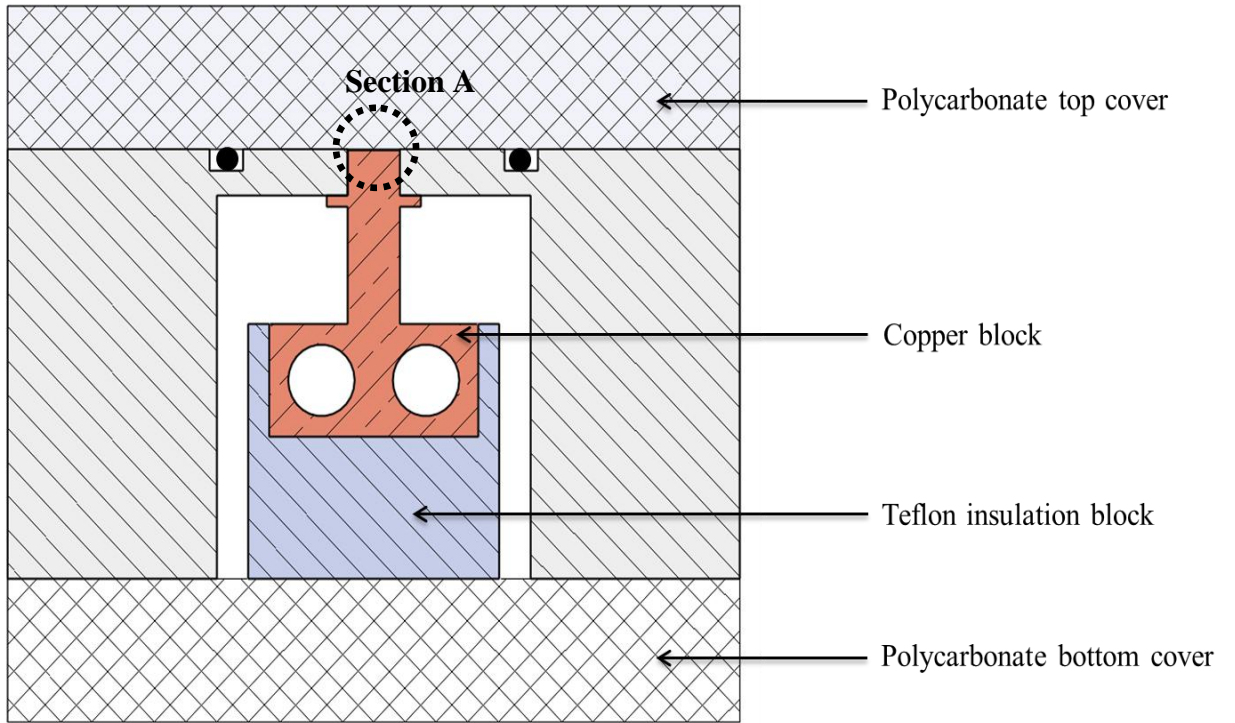
The test section assembly consists of a center housing, top cover, bottom cover, copper block and Teflon block. The center housing is made of Garolite (G-10). Garolite

was chosen because of its good insulating properties and its ability to withstand high temperatures (max. 265 °F) [102]. The copper block was machined from an ultra-pure (99.99%) oxygen-free, high-conductivity copper. The top and bottom covers are made of polycarbonate plastic. Polycarbonate was chosen because it is transparent and provides clear access to the top surface of the copper block for high speed visualization. The copper block was mounted on a Teflon insulation block to minimize heat loss to the surroundings. The cross-sectional view of this assembly and the microgap channel are shown Figure 7.2.

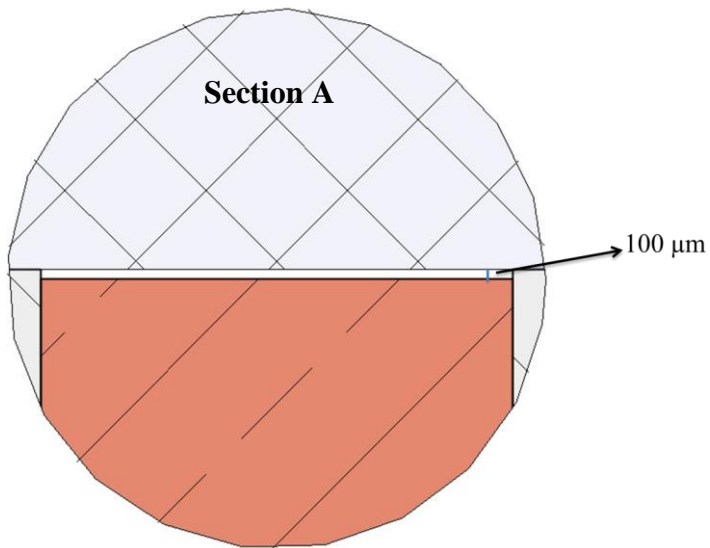
The top surface of the copper block measured 25.22 mm long and 5.06 mm wide. Two 6.35 mm diameter holes were drilled into the copper block to accommodate cartridge heaters (Watlow E1A53-L12). Power to the cartridge heaters was regulated using Agilent 6634B DC power supply. These cartridge heaters provide a maximum power input of 300 W. A high thermal conductivity paste (OmegaTherm® 201) was applied to the cartridge heaters to minimize the thermal resistance between the heater surface and the copper block. Five 1.59 mm diameter holes were drilled on the side wall of the copper block up to the center plane, to measure the stream wise temperature of the copper block. These holes were located at a distance of 6.40 mm below the top surface. Two more holes were drilled below the center hole at 3 mm interval, to measure the temperature of the copper block close to the heaters. T-type thermocouples (Omega™ TMQSS-062G-6) were inserted into these holes to measure the temperature of the copper block. The surface temperature at these locations was extrapolated from the thermocouple readings.

A small protruding platform was provided 4 mm below the top surface. This platform was used to facilitate accurate positioning of the copper block in the center housing. A silicone sealant (Momentive RTV 118) was applied along the vertical walls of the copper block above this protruding platform, to prevent leakage. The front view and the side view of the copper block, along with key dimensions are shown in Figure 7.3.

The center housing contained plenums both upstream and downstream the microgap channel. The temperature and pressure of the fluid, at the inlet and outlet plenums were monitored using absolute pressure transducers (Omega<sup>TM</sup> PX219) and T-type thermocouples. A 100  $\mu\text{m}$  deep cut was made in the center housing between the inlet and outlet plenum. The top surface of the copper block was flush with the bottom surface of this cut when assembled. The center housing served as the vertical walls of the channel; and the top cover served as the other horizontal wall of the channel. The top surface of the copper block served as the base of the channel. The microgap channel is shown in Figure 7.2(a). An O-ring was placed between the center housing and the top cover to ensure a leak – tight seal.

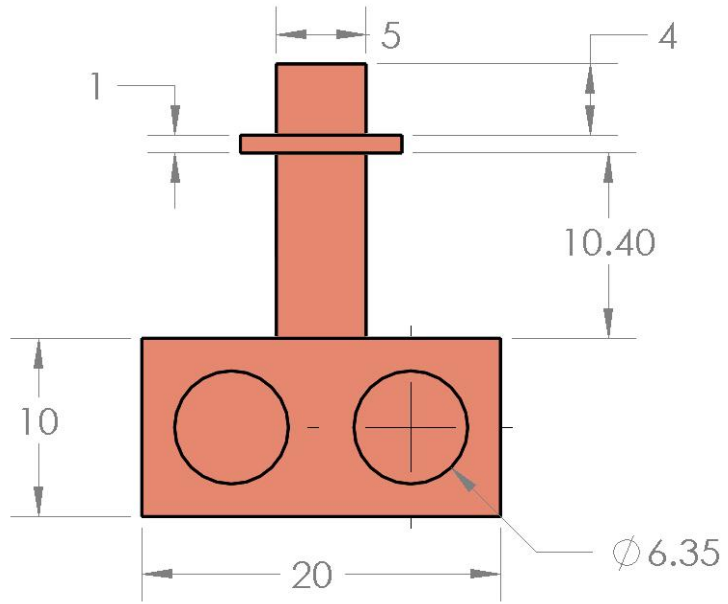


(a)

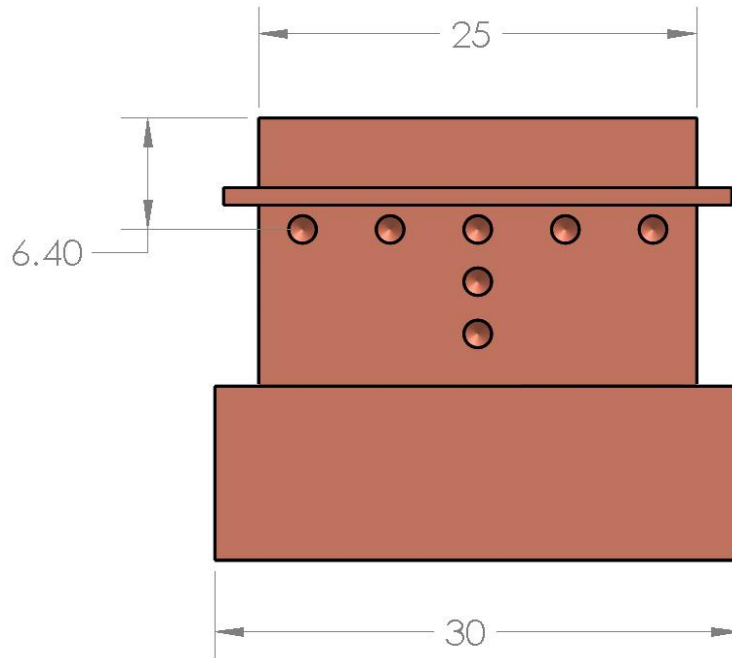


(b)

Figure 7.2: a) Cross-sectional view of test section assembly, and b) exploded view of the microgap channel



(a)



(b)

Figure 7.3: Copper block a) Front view, and b) Side view (all dimensions in mm)



### **7.3 Leak Test and Degassing**

From the contact angle measurements, it was observed that all the test fluids are volatile when exposed to ambient conditions. Any leaks in the flow loop might go unnoticed as these fluids quickly evaporate. Hence, extensive leak tests were performed at both high pressure, and vacuum conditions to ensure that the flow loop was leak free. First, the flow loop was filled with nitrogen gas at a high pressure (138 kPa absolute) and left at this state for at least 18 hours. The flow loop pressure was monitored using the pressure transducers in the loop. Next, the entire loop was evacuated and maintained at vacuum conditions (32 kPa absolute pressure). The loop pressure was monitored for 2 hours. The flow loop is said to be leak free if the pressure variation is less than  $\pm 1$  kPa for both the cases. Before performing the experiments, the test fluid was degassed by vigorously boiling it for over 2 hours on a hot plate heater. The liquid was then transferred to the reservoir.

### **7.4 Experimental Procedure**

Before running the experiment, the entire flow loop was flushed with nitrogen gas to remove any traces of liquid in the flow loop. The flow loop was then maintained at vacuum conditions and kept at this state for two hours. Once the flow loop was determined to be leak – free, the valves located immediately at the reservoir inlet and outlet were opened, and the test fluid was circulated in the flow loop using the gear pump. For all the experiments, the liquid flow rate, liquid temperature at the test section inlet and the pressure at the test section exit were fixed. Power to the cartridge heaters was switched on and the flow loop components were adjusted to yield the desired operating conditions. At each power input, data were recorded once the system reached

steady state (temperature variation less than  $\pm 0.2$  °C). It took approximately 30 – 60 minutes to reach steady state. An average of at least 100 readings was taken for all the parameters at steady state. Power to the heaters was then incremented in steps of 2.5 V and the same procedure was followed. Experiments were terminated when a sudden increase in the wall temperature was observed ( $\Delta T > 10$  °C). The CHF is calculated at the power input corresponding to the last observed steady state wall temperature, beyond which this sudden increase in temperature was observed.

After the experiments, the test liquid was evacuated from the flow loop using a vacuum pump. The drain valve was then opened and the flow loop was left at this state for a day. Since the fluids used in this study are volatile, this step ensures that any traces of liquid present in the loop vaporizes before performing experiments with another test fluid.

### 7.5 Data Reduction

Prior to performing the two phase experiments, single phase experiments were performed to estimate the heat loss from the copper block. The sensible heat gained by the liquid is given by,

$$\dot{Q} = \rho \dot{V} c_p (T_{out} - T_{in}) \quad (7.1)$$

where  $\rho$ ,  $c_p$  are the density and specific heat of the fluid respectively,  $\dot{V}$  is the volumetric flow rate of the fluid,  $T_{out}$  and  $T_{in}$  are the outlet and inlet temperatures of the fluid measured at the outlet and inlet plenums respectively. The power supplied to the heaters is calculated by measuring the voltage (V) and current (I) directly from the DC power supply. A multimeter was also used to measure the current and the voltage across

the terminals of the cartridge heaters. There were no losses in the load lines and the multimeter readings exactly matched the readings on the power supply display. The input power to the heaters is given by,

$$\dot{Q}_{in} = VI \quad (7.2)$$

The difference between the input power ( $\dot{Q}_{input}$ ) to the heaters and the sensible heat gained by the liquid is denoted as the heat loss.

$$\dot{Q}_{loss} = \dot{Q}_{input} - \dot{Q}_{sensible} \quad (7.3)$$

Three thermocouples were used to measure the stream wise temperature of the copper block. The top surface (wall) temperature was extrapolated from these thermocouple measurements. The wall temperature ( $T_w$ ) is given by,

$$T_{w,i} = T_{TC,i} - \dot{Q}R_{tot} \quad (7.4)$$

where  $T_{w,i}$  is the surface temperature at location  $i$ ,  $T_{TC,i}$  is the reading of the thermocouple at location  $i$ , and  $R_{tot}$  is the total thermal resistance between the thermocouple location and the wall. This thermal resistance includes the spreading resistance due to the presence of the protruding platform. The average wall temperature was calculated by averaging the wall temperatures at these three locations. The average wall temperature and the effective wall heat flux are given by,

$$T_w = \frac{T_{w,1} + T_{w,2} + T_{w,3}}{3} \quad (7.5)$$

$$q'' = \frac{(\dot{Q}_{input} - \dot{Q}_{loss})}{A} \quad (7.6)$$

The calculated heat loss was plotted against the average wall temperature and a correlation was obtained for the heat loss in terms of the wall temperature. For two phase experiments, the heat loss was estimated at each power input based on this correlation using an iterative approach.

### 7.6 Calibration and Measurement Uncertainty

The pressure transducers were calibrated using a pressure calibrator (Omega™ DPI620). The calibrator measures the gage pressure. So atmospheric pressure was added to all the readings to obtain the absolute pressure. A precision barometer (Robert W. White Instruments) was used to measure the atmospheric pressure in the room. The uncertainty in the measurement of pressure is 0.25% of the full scale value (30 psi). All the thermocouples were calibrated using a thermocouple calibrator (Omega™ CL122). NIST Traceable calibrated thermometer was used as the reference for the calibration. The uncertainty in the measurement of temperature is ±0.2 °C. The flow meter was calibrated for all the fluids using the standard bucket – stop watch method and the uncertainty in the measurement of flow rate is 1% of the full scale value (100 ml/min).

The uncertainty in the measurement of voltage and current from the DC power supply are ±24 mV and ±0.252 mA respectively. The uncertainty in the measurement of effective heat flux was calculated using Equation 7.6. Following the procedure outlined by Kline and McClintock [54], the resulting uncertainty in the measurement of effective heat flux is 5.4%.

## 7.7 Experimental Results

Flow boiling experiments were performed to investigate the heat transfer performance of pure HFE 7200 and 20 wt. % mixture of HFE 7200 – methanol. The fluid temperature at the test section inlet remained the same for both the fluids and hence, the degree of subcooling is different for each fluid because of differences in the saturation/bubble point temperature. The operating conditions for flow boiling experiments on both the surfaces are shown in Table 7.1. The flow velocity corresponding to a flow rate of 38 ml/min is 1.28 m/s. The flow Reynolds number for pure HFE 7200 and 20 wt. % mixture of HFE – methanol in the microgap channel are 579 and 554 respectively. It was observed while performing single phase experiments that the mixture was flowing in layers. This probably could be occurring if methanol was not completely miscible in HFE 7200.

Table 7.1: Flow boiling experimental conditions

Parameter	Value
Fluid inlet temperature	23 °C
Flow rate	38 ml/min
Test section outlet pressure	1.1 bar

High speed movies and images of boiling from the copper surfaces were recorded using Photron 1024 PCI camera. The test section area was illuminated using a fiber optic light source. All the images were captured at 1000 fps at a resolution of 1024 x 1024 pixels. At any time instant, it was not possible to visualize boiling from the entire length

of the channel because of constraints imposed by the lens resolution. Hence, the microgap channel was divided into three regions (inlet, middle and outlet) and high speed videos were recorded at all three regions for various power inputs. The inlet, middle and outlet regions on the microgap channel are shown in Figure 7.4.

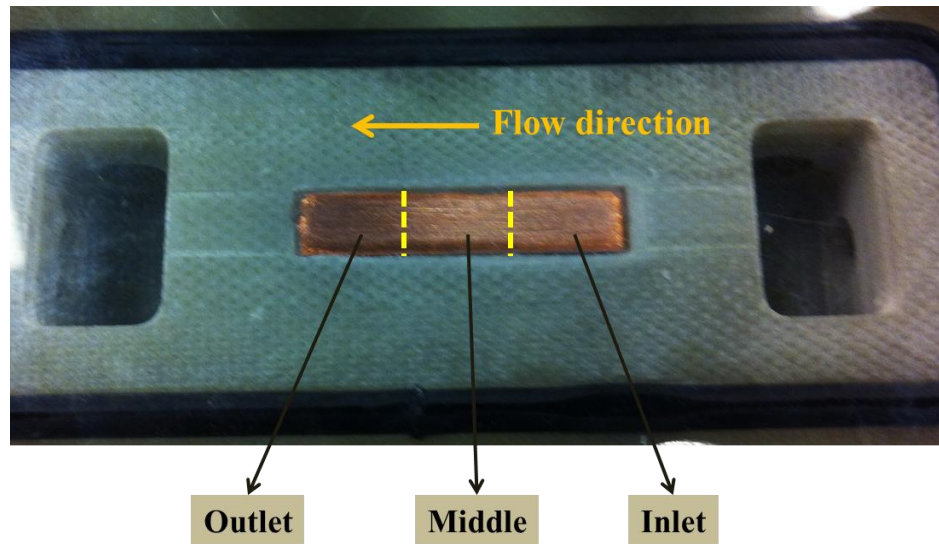


Figure 7.4: Three regions of the microgap test section used for high speed visualization

### 7.7.1 Flow Boiling on Polished Surface

Flow boiling experiments were performed using pure HFE 7200 and 20 wt. % mixture of methanol – HFE 7200 on a polished copper surface. The top surface of the copper block was polished using a 220 grit sandpaper. The root mean square surface roughness of the polished surface, measured using a 3D confocal microscope, was 1.143  $\mu\text{m}$ . The SEM images of the top surface are shown in Figures 7.5 and 7.6. The flow boiling curves for pure HFE 7200 and 20 wt. % mixture of HFE 7200 - methanol are shown in Figures 7.7 and 7.8 respectively. In these curves, the effective heat flux is plotted against the difference between average wall temperature and the fluid inlet temperature.

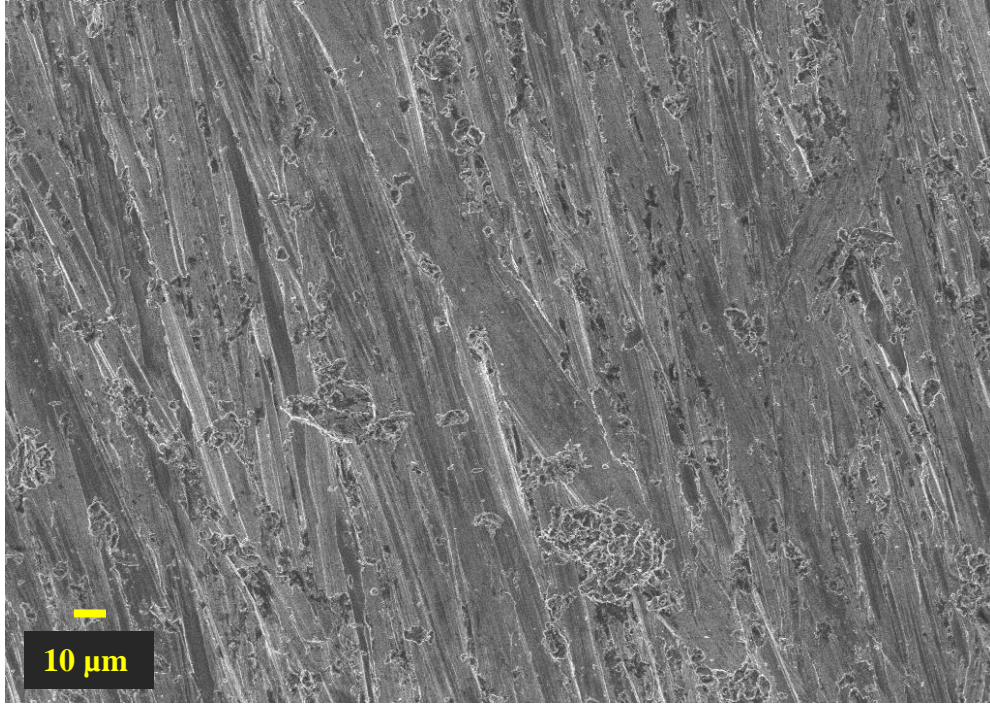


Figure 7.5: SEM image of the polished copper surface (top view)

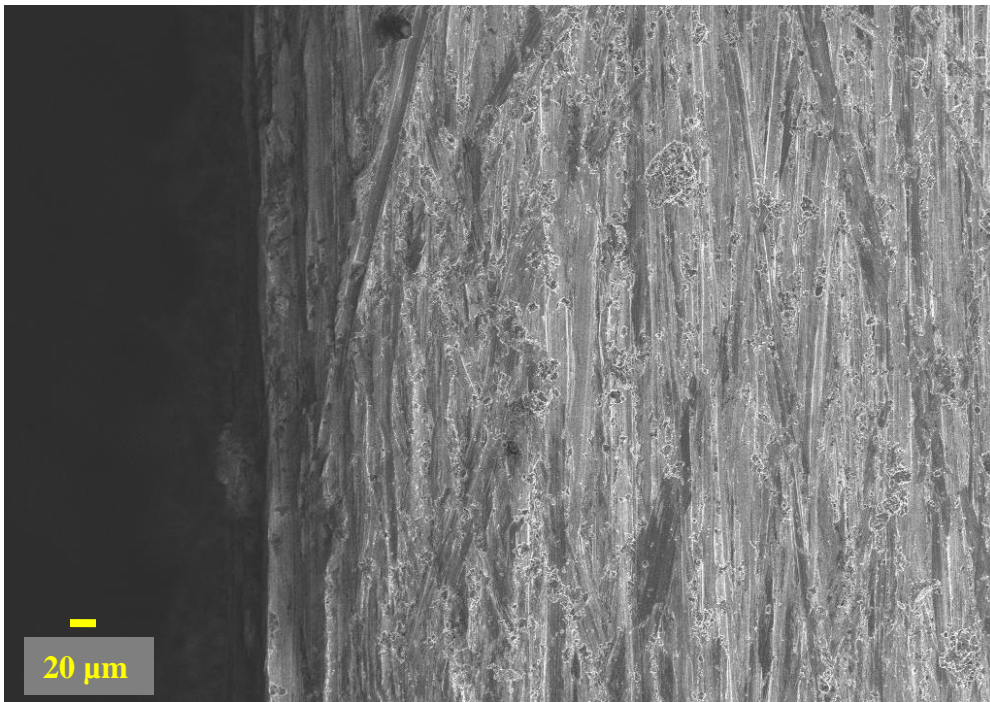


Figure 7.6: SEM image of the edge of the polished copper surface (top view)

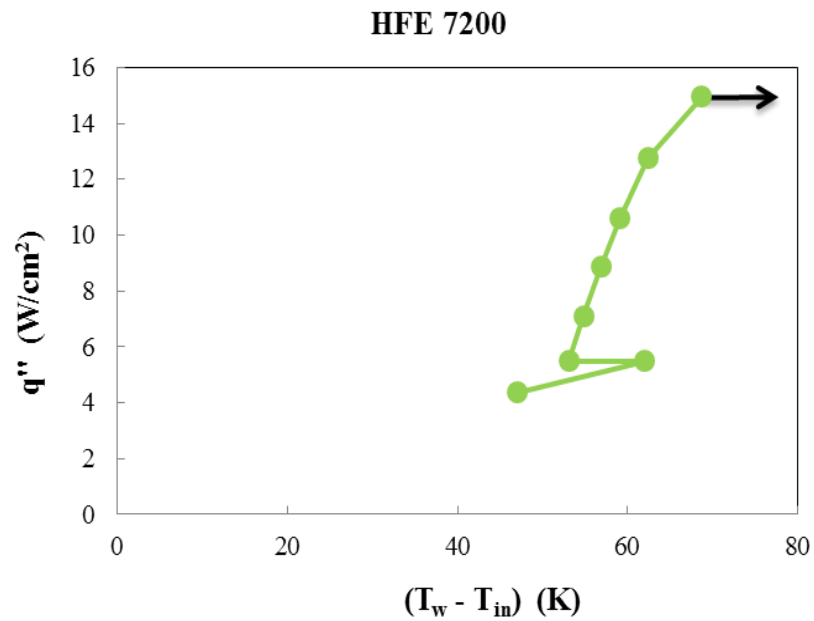


Figure 7.7: Flow boiling curve for HFE 7200 at subcooled condition on a polished Cu surface

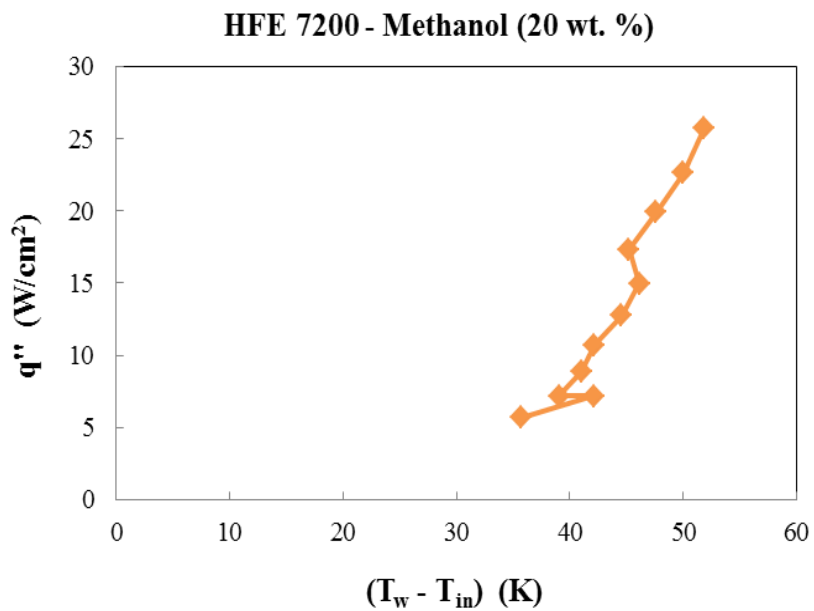


Figure 7.8: Flow boiling curve for 20 wt. % mixture of HFE 7200 - methanol at subcooled condition on a polished Cu surface



At low heat fluxes, the slope of the boiling curve was fairly constant indicating single phase heat transfer. As the heat flux increased, the slope of the boiling curve increased significantly, indicating the ONB. With further increase in the heat flux, a moderate increase in the wall temperature was observed. Also, temperature overshoot at the ONB which is a characteristic of highly wetting fluids, was larger for HFE 7200 than the fluid mixture. The heat flux corresponding to the ONB for pure HFE 7200 and the mixture were  $5.48 \text{ W/cm}^2$  and  $7.19 \text{ W/cm}^2$  respectively.

The CHF for flow boiling of pure HFE 7200 is  $15 \text{ W/cm}^2$ . The flow boiling experiment using HFE 7200 – methanol mixture had to be terminated because of limitations imposed by the DC power supply. Hence, the CHF could not be quantified for the mixture. The CHF is a strong function of the flow velocity and increases as the flow velocity increases. The low CHF for pure HFE 7200 could be due to the low flow rate employed in this study. However, it can be inferred from these boiling curves and also through high speed visualization images of the flow regime, that the mixture can handle higher heat fluxes than pure HFE 7200. The pressure drop between the inlet and outlet plenums was less than 1.2 kPa for both the fluids. This observed pressure drop is comparable to the pressure drop reported in the literature for microgap channels of the same size [103, 104].

The high speed images captured at three different heat fluxes for pure HFE 7200 and 20 wt. % mixture of HFE 7200 – methanol are shown in Figures 7.9 – 7.14. A graphical representation of the flow regime, based on the high speed videos captured at the inlet, middle and outlet regions of the channel, is also shown for each case. The white

circles represent the vapor phase and the blue regions represent the liquid phase. The solid white lines on the images represent the microgap channel boundaries.

From these images, it can be inferred that the bubble dynamics for flow boiling of pure HFE 7200 is very different from that of 20 wt. % mixture of HFE 7200 – Methanol. The bubble departure diameters were lower for the mixture than HFE 7200 at all heat fluxes. At the heat flux corresponding to CHF for pure HFE 7200, the mixture still exhibited bubbly flow regime. This is evident from Figure 7.14. For both the fluids, several nucleation sites were active along the entire length of the channel at all heat fluxes. The bubbles originating at the inlet region coalesced with several other bubbles on the way downstream to form large diameter bubbles. The bubbles could be clearly visualized for pure HFE 7200. The mixture however, was turning translucent when heated at the copper surface and hence, it was difficult to visualize the bubbles.

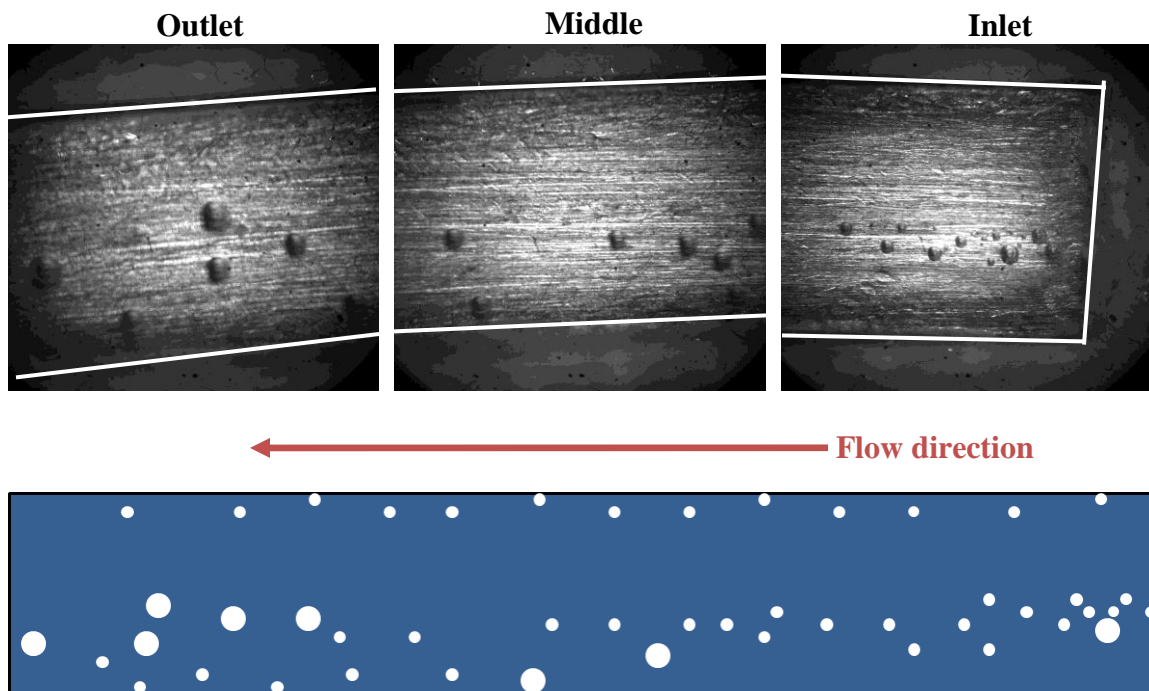


Figure 7.9: Flow boiling of HFE 7200 at subcooled condition on a polished Cu surface at  $6 \text{ W/cm}^2$

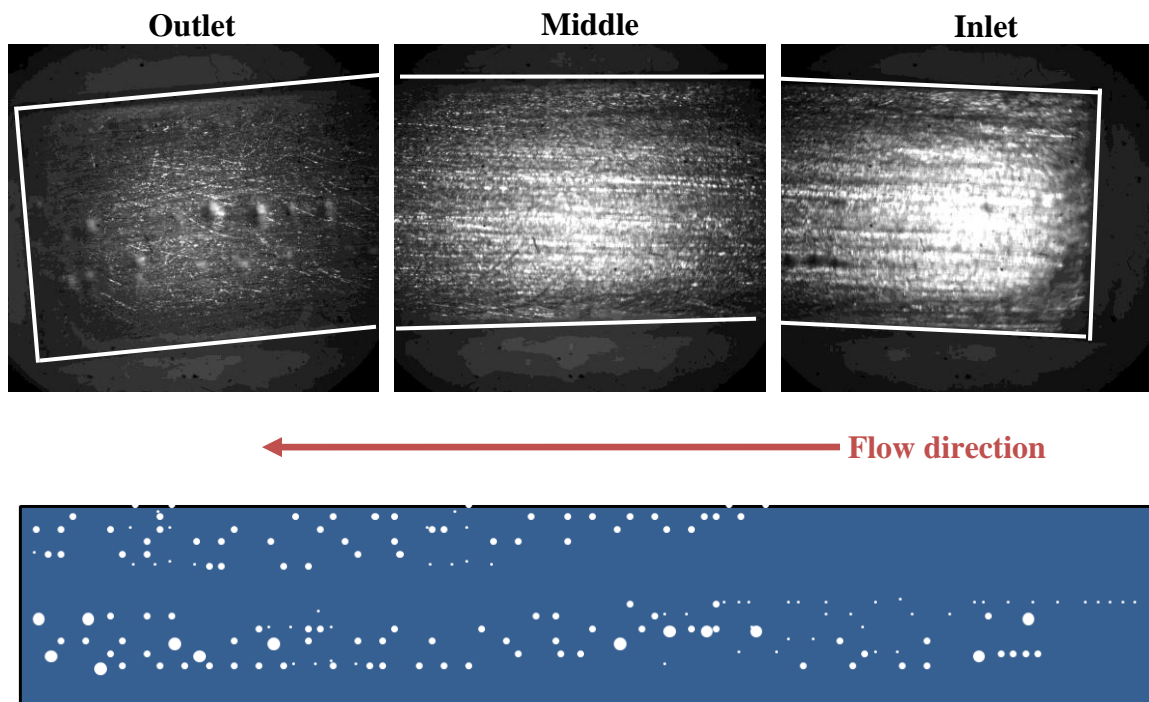


Figure 7.10: Flow boiling of 20 wt. % HFE 7200 – methanol mixture at subcooled condition on a polished Cu surface at  $7 \text{ W/cm}^2$

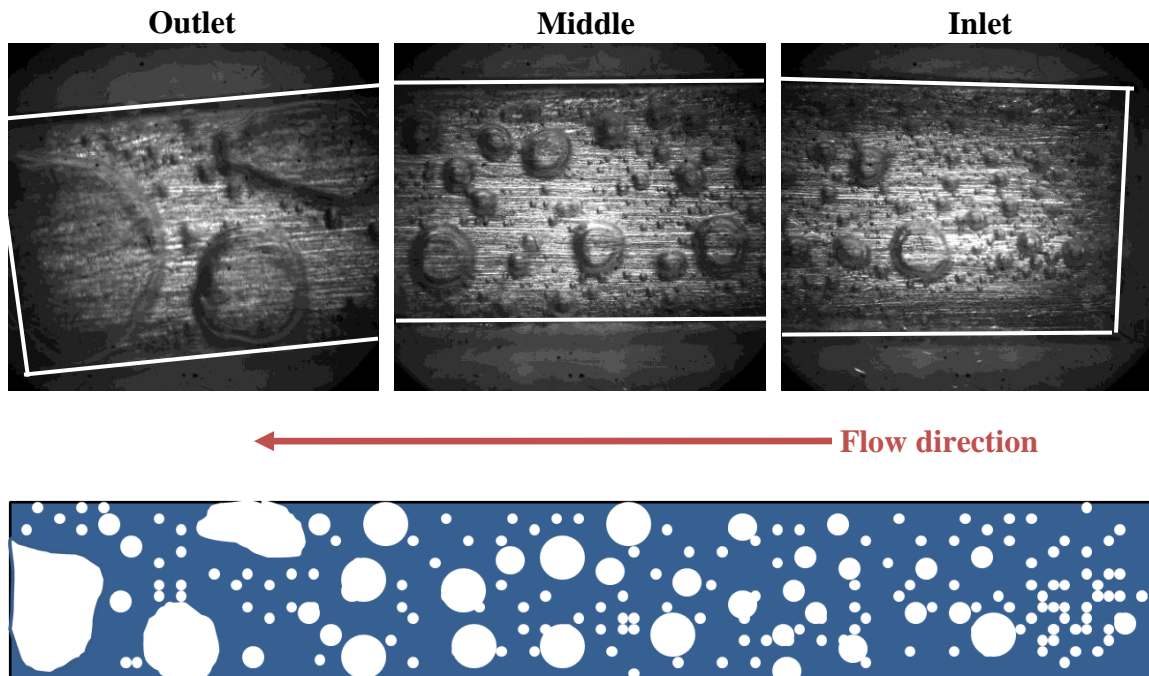


Figure 7.11: Flow boiling of HFE 7200 at subcooled condition on a polished Cu surface at  $11 \text{ W/cm}^2$

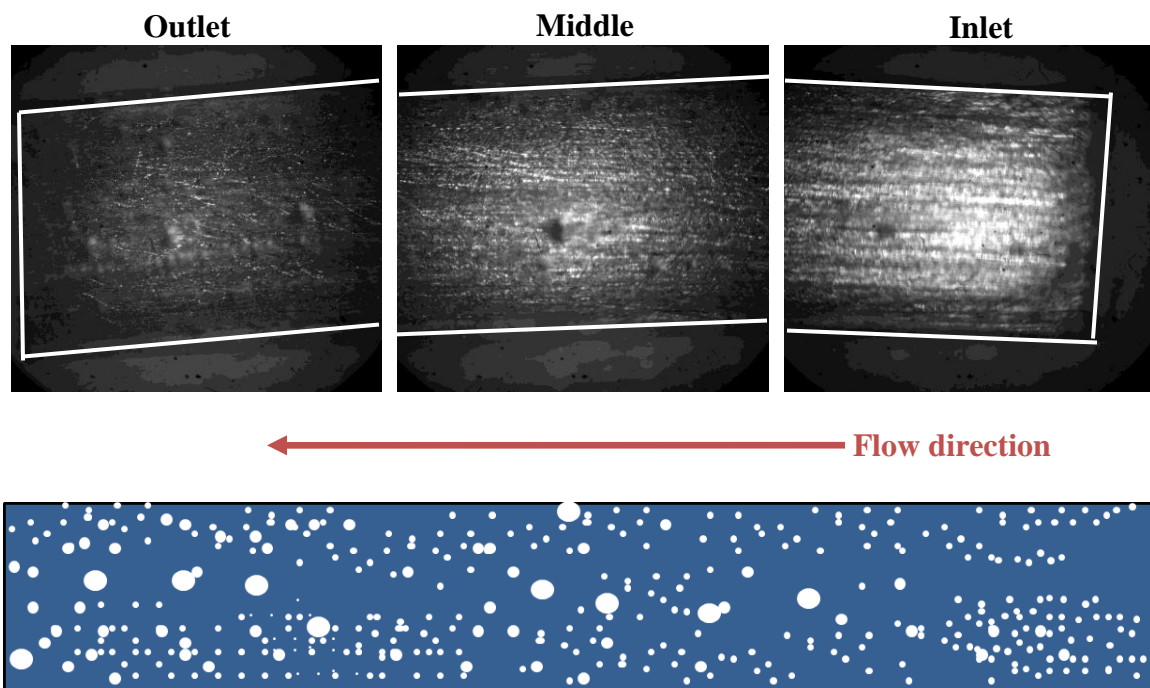


Figure 7.12: Flow boiling of 20 wt. % HFE 7200 – methanol mixture at subcooled condition on a polished Cu surface at  $11 \text{ W/cm}^2$

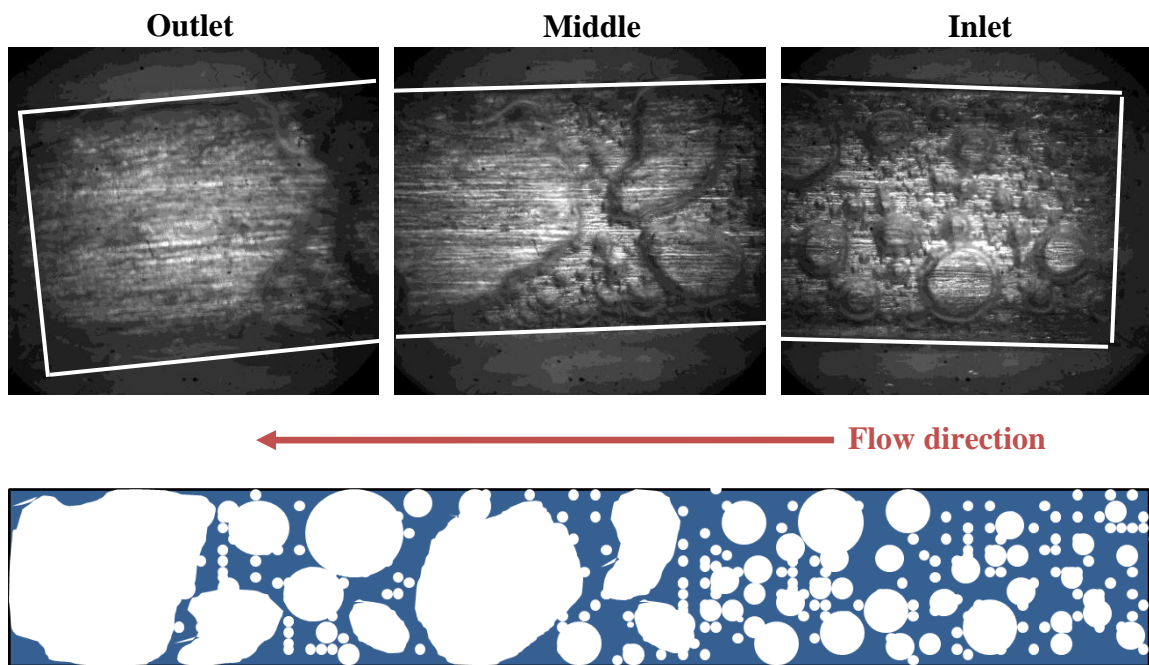


Figure 7.13: Flow boiling of HFE 7200 at subcooled condition on a polished Cu surface at  $15 \text{ W/cm}^2$

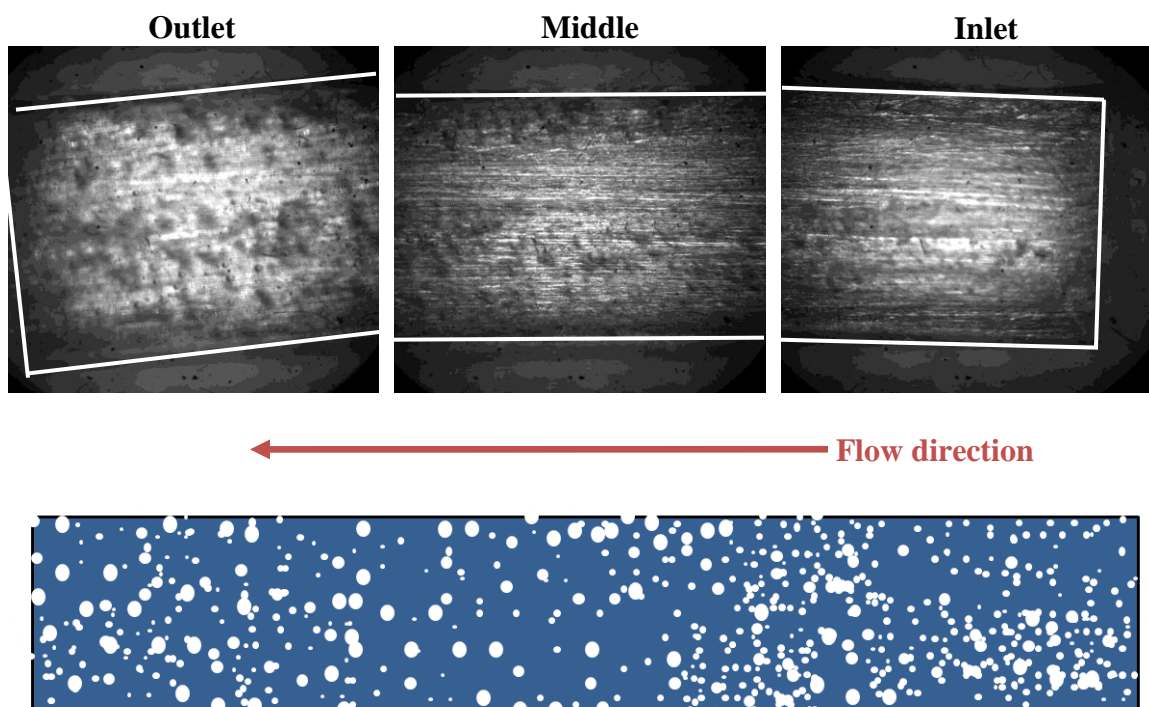


Figure 7.14: Flow boiling of 20 wt. % HFE 7200 – methanol mixture at subcooled condition on a polished Cu surface at  $15 \text{ W/cm}^2$

### 7.7.2 Flow Boiling on Unpolished Surface

The flow boiling curves for pure HFE 7200 and 20 wt. % mixture of HFE 7200 - methanol are shown in Figures 7.15 and 7.16 respectively. It can be observed from these boiling curves that temperature overshoot at the ONB was larger for HFE 7200 than the fluid mixture. The heat flux corresponding to the ONB was  $5.76 \text{ W/cm}^2$  for pure HFE 7200. The mixture however, started boiling at two different heat fluxes ( $7.26 \text{ W/cm}^2$  and  $8.97 \text{ W/cm}^2$ ) which resulted in small temperature overshoots at these heat fluxes. The CHF for flow boiling of pure HFE 7200 is  $17.1 \text{ W/cm}^2$ . The CHF could not be quantified for the mixture because of power supply limitations. However, it can be observed from these boiling curves that the mixture has the potential to handle higher heat fluxes than pure HFE 7200.

The pressure drop between the inlet and outlet plenums was less than 1 kPa for both the fluids. The high speed images captured at three different heat fluxes for pure HFE 7200 and 20 wt. % HFE 7200 – methanol mixture are shown in Figures 7.17 – 7.22. A graphical representation of the flow regime, based on the high speed images captured at the inlet, middle and outlet regions of the channel, is also shown for each case.

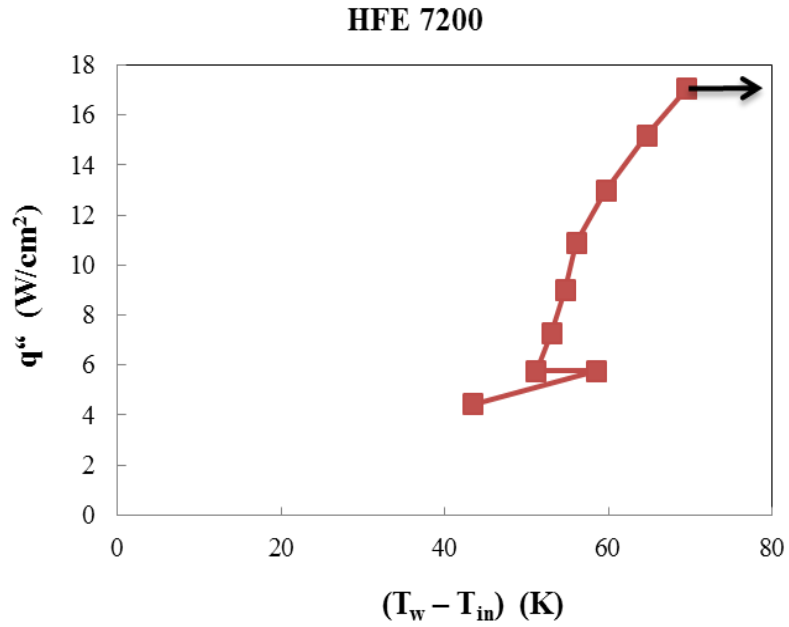


Figure 7.15: Flow boiling curve for HFE 7200 at subcooled condition on an unpolished Cu surface

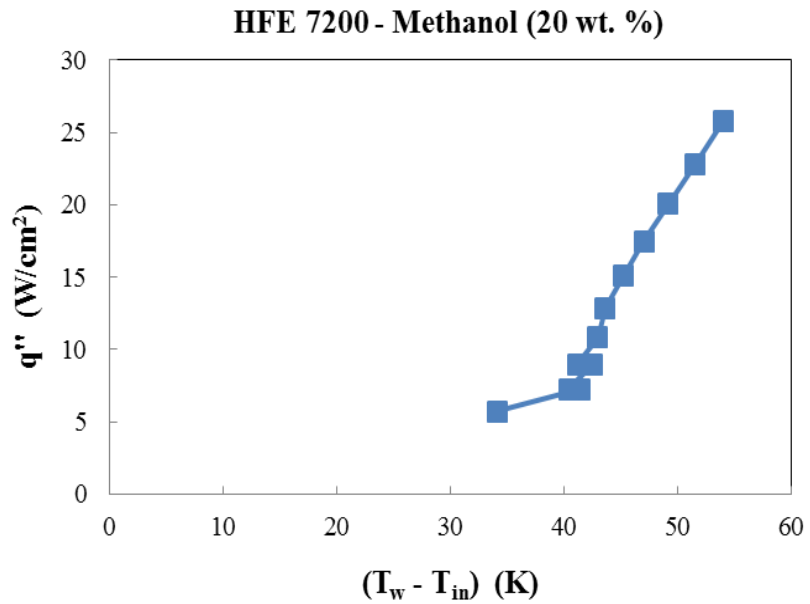


Figure 7.16: Flow boiling curve for 20 wt. % mixture of HFE 7200 - methanol at subcooled condition on an unpolished Cu surface

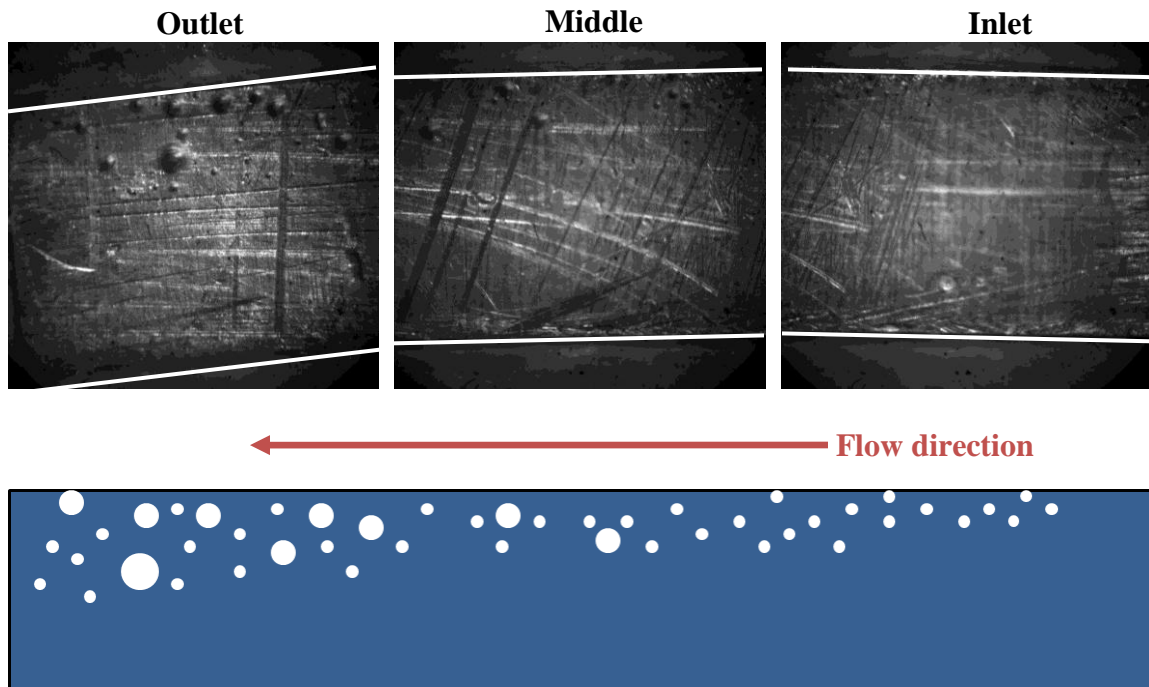


Figure 7.17: Flow boiling of HFE 7200 at subcooled condition on an unpolished Cu surface at  $6 \text{ W/cm}^2$

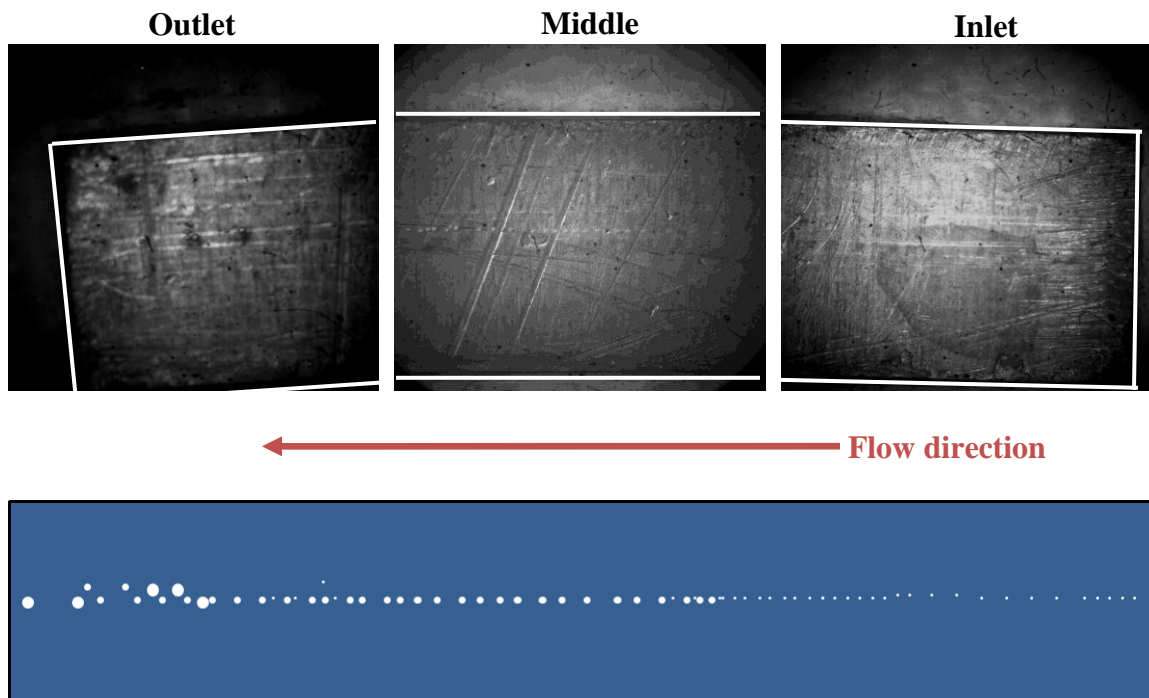


Figure 7.18: Flow boiling of 20 wt. % HFE 7200 – methanol mixture at subcooled condition on an unpolished Cu surface at  $7 \text{ W/cm}^2$



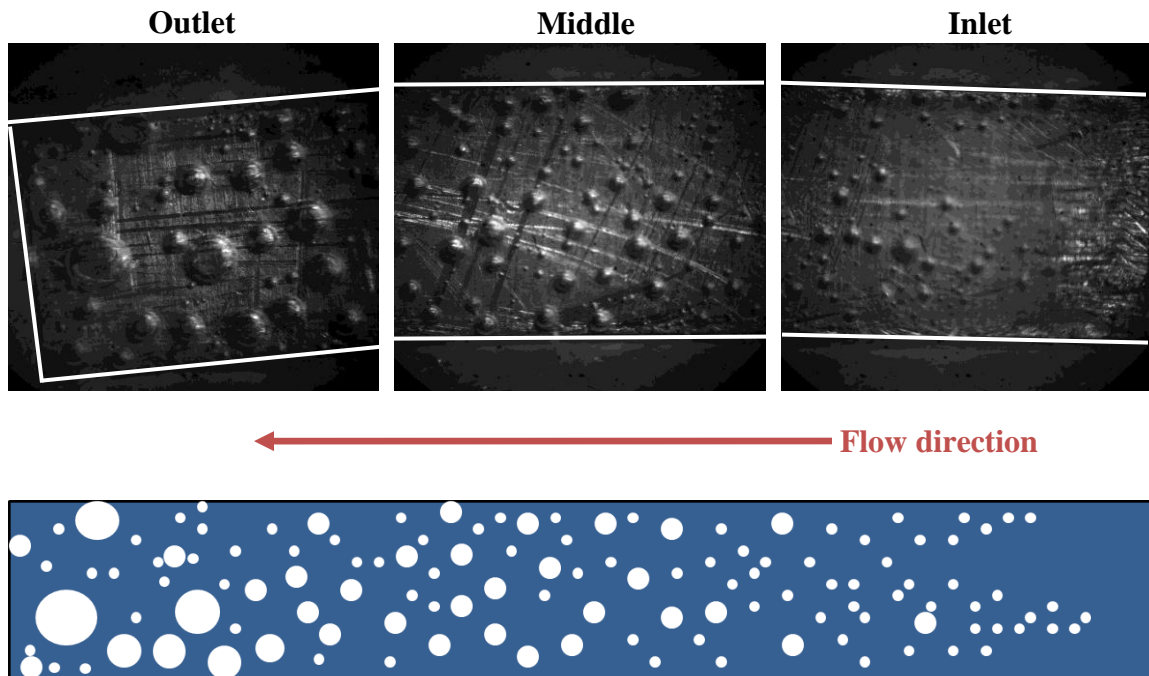


Figure 7.19: Flow boiling of HFE 7200 at subcooled condition on an unpolished Cu surface at  $11 \text{ W/cm}^2$

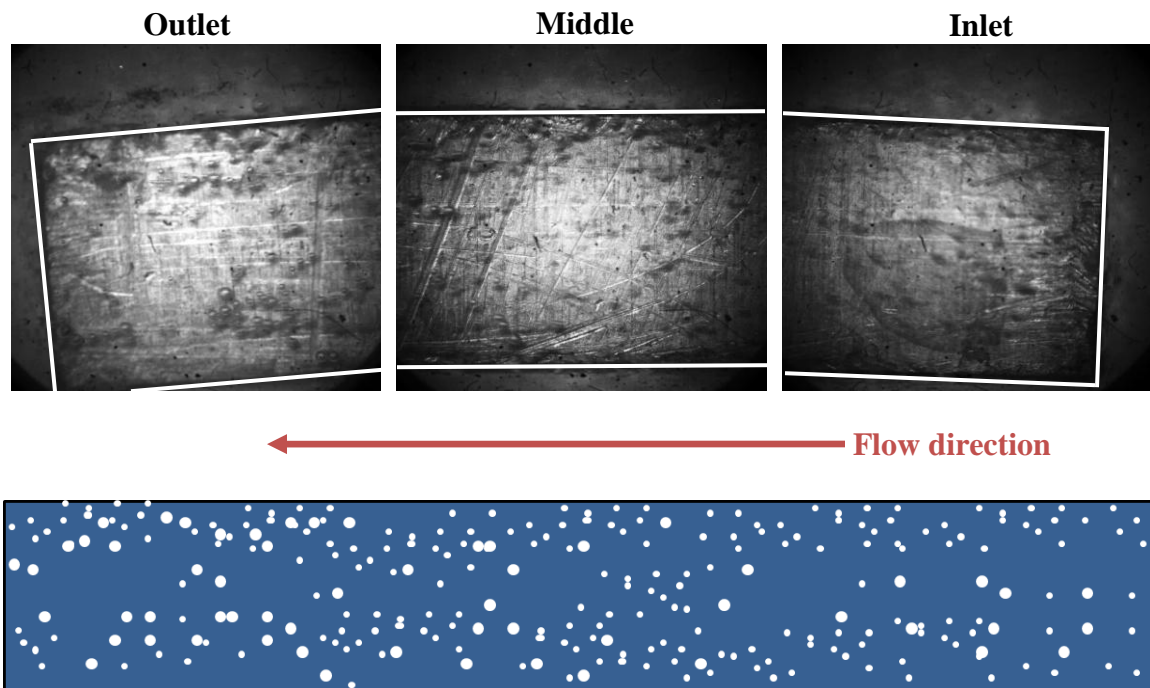


Figure 7.20: Flow boiling of 20 wt. % HFE 7200 – methanol mixture at subcooled condition on an unpolished Cu surface at  $11 \text{ W/cm}^2$

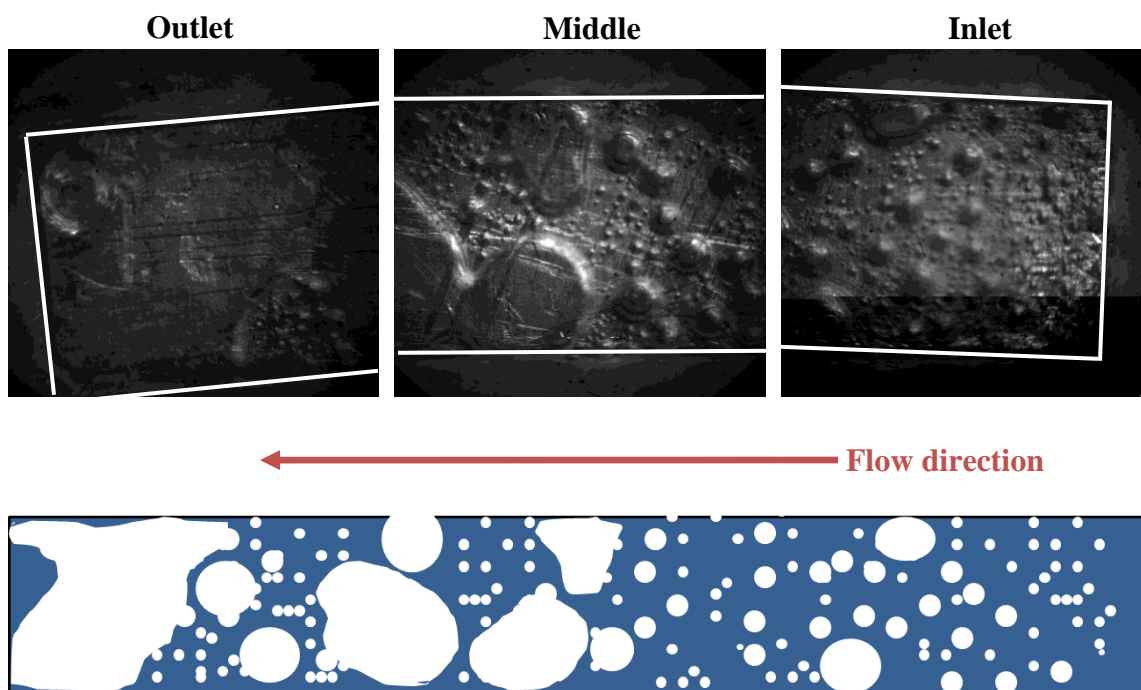


Figure 7.21: Flow boiling of HFE 7200 at subcooled condition on an unpolished Cu surface at  $15 \text{ W/cm}^2$

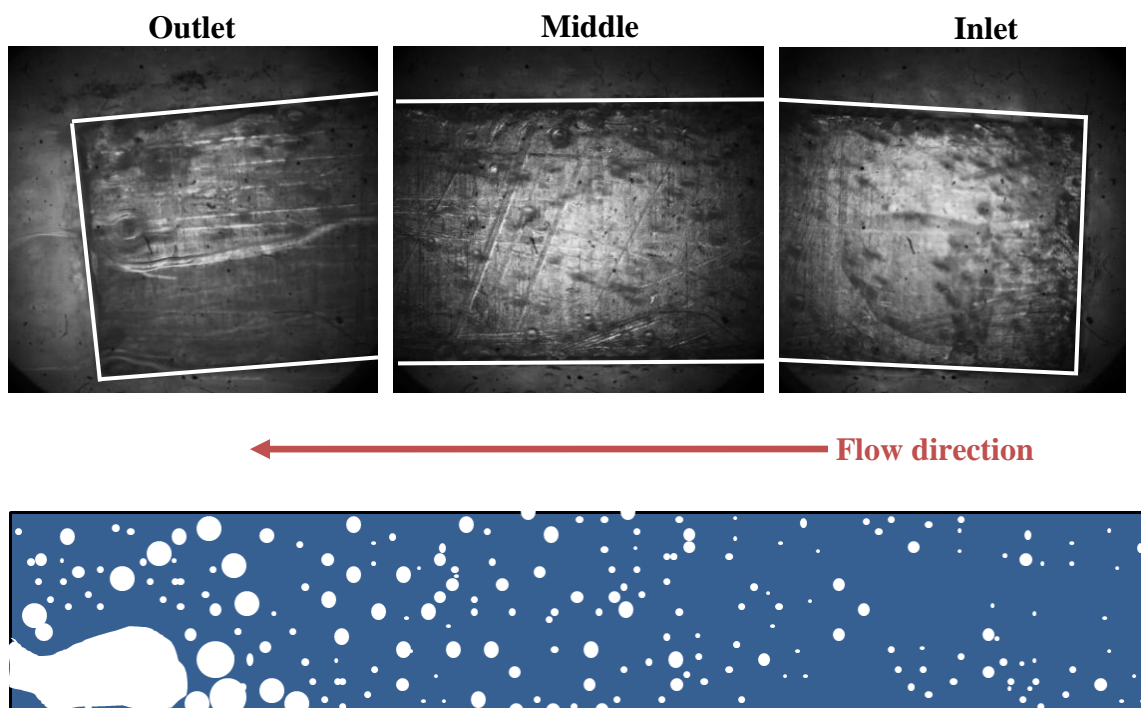


Figure 7.22: Flow boiling of 20 wt. % HFE 7200 – methanol mixture at subcooled condition on an unpolished Cu surface at  $15 \text{ W/cm}^2$

From the above images, it can again be observed that the bubble dynamics were different for HFE 7200 and the mixture. Similar to the polished surface, the bubble departure diameters were significantly lower for the mixture than HFE 7200 at all heat fluxes. From Fig 7.22, it can be observed that the mixture still exhibited bubbly flow regime, at a heat flux close to CHF for pure HFE 7200. This could potentially be the reason for the mixture's ability to handle higher heat fluxes than pure HFE 7200.

### **7.8 Summary**

In this chapter, the details of the flow boiling experimental setup and the microgap channel test section were discussed. The experimental procedure, data reduction and measurement uncertainty were presented. Flow boiling experiments were performed using two fluids on polished and unpolished copper surfaces. The experimental results and high speed visualization images comparing the bubble departure diameters for fluids were presented. The main observations from this study are listed below:

- 1) Although the CHF could not be quantified for the 20 wt. % mixture of HFE 7200 – methanol, the experimental results showed that the mixture had the potential to handle higher heat fluxes than HFE 7200, on both polished and unpolished surfaces.
- 2) The bubble departure diameters were significantly lower for the mixture when compared to HFE 7200 at all heat fluxes. At the heat flux corresponding to CHF for HFE 7200, the mixture still exhibited bubbly flow regime. This could probably be one of the reasons for the mixture's ability to handle higher heat fluxes.

## CHAPTER 8

### CONCLUSIONS AND FUTURE WORK

#### 8.1 Conclusions

This dissertation addresses the task of identifying new coolants for direct immersion phase change cooling applications. CAMD approach was used to systematically design novel heat transfer fluids that have superior thermal properties than existing coolants. Molecules were generated by combining more than 25 functional groups including alcohol, ketone, ester, ether, methyne, methylene, methyl and fluorine groups. The maximum number of groups in a molecule was restricted to 10, because boiling points of molecules having more than ten groups are likely to be too high. The thermophysical properties of the candidate fluids were estimated using group contribution methods.

Heat transfer considerations and reliability of group contribution methods led to the selection of three properties: boiling point, latent heat of vaporization and thermal conductivity for screening thousands of candidate fluids generated using the CAMD approach. The shortlisted candidates were further screened using FOM analysis. The FOM's were derived from existing heat transfer correlations relevant to pool and flow boiling. Four new heat transfer fluids ( $C_4H_5F_3O$ ,  $C_4H_4F_6O$ ,  $C_6H_{11}F_3$ , and  $C_4H_{12}O_2Si$ ), which were never before considered for electronics cooling, were selected for experimental evaluation based on commercial availability and knowledge of synthesis steps. Two existing fluids (methanol and ethoxybutane) were also selected for experimental evaluation using knowledge based approach.

The thermophysical properties of new fluids were experimentally evaluated and found to have superior thermal properties, when compared to the base fluid, HFE 7200. The wetting characteristics of the new fluids were investigated through contact angle measurements. All the new fluids exhibited wetting characteristics similar to HFE 7200. The heat transfer performance of these fluids was analyzed through pool and flow boiling experiments. Pool boiling experiments were performed on both plain and nanostructured surfaces, using mixtures of new fluids with HFE 7200. All the fluid mixtures tested showed a significant improvement in the CHF when compared to HFE 7200. Also, the CHF predictions for pool boiling on infinite and small heaters showed that the CHF increases as the concentration of the new fluid in the mixture increases.

A pool boiling model was developed using the phase field method in COMSOL, to supplement the experimental results. Simulations were first performed using HFE 7200 to evaluate the grid size dependence of results. The grid settings did not have any effect on the bubble departure diameters, but there was a considerable difference in the bubble departure frequency. Next, simulations were performed using HFE 7200 and  $C_4H_4F_6O$ . Although the simulation results were comparable to the theoretical predictions for  $C_4H_4F_6O$ , there was a significant deviation for HFE 7200. The reasons for this discrepancy were discussed. The constant  $C$  in the equation for mass flux plays a significant role in the simulation results.

Flow boiling experiments were performed using HFE 7200 and 20 wt. % mixture of HFE 7200 – methanol, on polished and unpolished copper surfaces. The experimental results showed that the mixture had the potential to handle higher heat fluxes than HFE 7200 on both surfaces. High speed visualization performed during the flow boiling

experiments revealed that the bubble departure diameters were significantly smaller for the mixture than pure HFE 7200 at all heat fluxes, on both surfaces. This reduction in bubble departure diameter could possibly be one reason for the enhancement in CHF using the mixture.

## **8.2 Recommendations for Future Work**

This work has demonstrated the successful application of CAMD approach in identifying new heat transfer fluids for direct immersion cooling applications. All the new fluids identified showed improvement in the heat transfer performance and therefore, merit further investigation. The following are some of the recommendations for future work:

### **8.2.1 New Fluid Synthesis**

Synthesis and economic constraints prevented us from evaluating the heat transfer performance of new fluids either by themselves or at higher mixture concentrations. Hence, the fluid synthesis has to be scaled up so that pool and flow boiling experiments can be performed using pure fluids.

### **8.2.2 Pool Boiling Experiments**

The bubble departure parameters play an important role in boiling heat transfer. Because of constraints imposed by the test chamber, bubble departure parameters could not be experimentally measured through high speed visualization. By modifying the glass chamber design, these parameters can be experimentally determined and this could shed more light on the mechanisms responsible for heat transfer enhancement using new fluid mixtures.

### **8.2.3 Pool Boiling Modeling**

A basic pool boiling model was developed using the phase field method. However, the simulation results show discrepancy with the theoretical predictions for HFE 7200. Possible reasons for this discrepancy were discussed and all those comments have to be addressed, before this model can be used to evaluate heat transfer fluids.

### **8.2.4 Flow Boiling Experiments**

The CHF was not measured for the HFE 7200 – Methanol mixture because of power supply limitations. Hence, the current investigation should be extended to quantify the CHF.

## REFERENCES

- [1] F. P. Incropera, *Liquid Cooling of Electronic Devices by Single-Phase Convection*, 1 ed.: Wiley InterScience, 1999.
- [2] R. R. Tummala and M. Swaminathan, *Introduction to system-on-package (SOP) : miniaturization of the entire system*. New York: McGraw-Hill, 2008.
- [3] M. E. Poniewski and J. R. Thome, *Nucleate Boiling on Micro-structured Surfaces*. College Station, TX: Heat Transfer Research, Inc., 2008.
- [4] S. C. Mohapatra, "An Overview of Liquid Coolants for Electronics Cooling," *Electronics Cooling*, vol. 12, pp. 1-6, 2006.
- [5] P. M. Harper, R. Gani, P. Kolar, and T. Ishikawa, "Computer-aided molecular design with combined molecular modeling and group contribution," *Fluid Phase Equilibria*, vol. 158–160, pp. 337-347, 1999.
- [6] G. Rafiqul, "Chemical product design: challenges and opportunities," *Computers & Chemical Engineering*, vol. 28, pp. 2441-2457, 2004.
- [7] R. Gani, C. Jiménez-González, and D. J. C. Constable, "Method for selection of solvents for promotion of organic reactions," *Computers & Chemical Engineering*, vol. 29, pp. 1661-1676, 2005.
- [8] E. C. Marcoulaki and A. C. Kokossis, "On the development of novel chemicals using a systematic synthesis approach. Part I. Optimisation framework," *Chemical Engineering Science*, vol. 55, pp. 2529-2546, 2000.
- [9] O. Odele and S. Macchietto, "Computer aided molecular design: a novel method for optimal solvent selection," *Fluid Phase Equilibria*, vol. 82, pp. 47-54, 1993.
- [10] A. Duvedi and L. E. K. Achenie, "On the design of environmentally benign refrigerant mixtures: a mathematical programming approach," *Computers & Chemical Engineering*, vol. 21, pp. 915-923, 1997.



- [11] W. R. van Wijk, A. S. Vos, and S. J. D. van Stralen, "Heat transfer to boiling binary liquid mixtures," *Chemical Engineering Science*, vol. 5, pp. 68-80, 1956.
- [12] W. R. Van Wijk and S. J. D. Van Stralen, "Growth rate of vapour bubbles in water and in a binary mixture boiling at atmospheric pressure," *Physica*, vol. 28, pp. 150-171, 1962.
- [13] J. Hovestrijdt, "The influence of the surface tension difference on the boiling of mixtures," *Chemical Engineering Science*, vol. 18, pp. 631-639, 1963.
- [14] C. T. Avedisian and D. J. Purdy, "Experimental Study of Pool Boiling Critical Heat Flux of Binary Fluid Mixtures on an Infinitive Horizontal Surface," in *ASME International Electronics Packaging Conference*, Binghamton, New York, pp. 909-915, 1993.
- [15] W. R. McGillis and V. P. Carey, "On the Role of Marangoni Effects on the Critical Heat Flux for Pool Boiling of Binary Mixtures," *Journal of Heat Transfer*, vol. 118, pp. 103-109, 1996.
- [16] Y. Fujita and Q. Bai, "Critical heat flux of binary mixtures in pool boiling and its correlation in terms of Marangoni number," *International Journal of Refrigeration*, vol. 20, pp. 616-622, 1997.
- [17] S. G. Kandlikar and L. Alves, "Effects of Surface Tension and Binary Diffusion on Pool Boiling of Dilute Solutions: An Experimental Assessment," *Journal of Heat Transfer*, vol. 121, pp. 488-493, 1999.
- [18] H. Sakashita, A. Ono, and Y. Nakabayashi, "Measurements of critical heat flux and liquid–vapor structure near the heating surface in pool boiling of 2-propanol/water mixtures," *International Journal of Heat and Mass Transfer*, vol. 53, pp. 1554-1562, 2010.
- [19] P. J. C. Normington, M. Mahalingam, and T. Y. T. Lee, "Thermal management control without overshoot using combinations of boiling liquids," *Components, Hybrids, and Manufacturing Technology, IEEE Transactions on*, vol. 15, pp. 806-814, 1992.
- [20] A. A. Watwe and A. Bar-Cohen, "Enhancement of pool boiling critical heat flux using dielectric fluid mixture," in *Proceedings of IRSEE*, Germany, 1997.

- [21] M. Arik and A. Bar-Cohen, "Pool boiling of perfluorocarbon mixtures on silicon surfaces," *International Journal of Heat and Mass Transfer*, vol. 53, pp. 5596-5604, 2010.
- [22] D. L. Bennett and J. C. Chen, "Forced convective boiling in vertical tubes for saturated pure components and binary mixtures," *AIChE Journal*, vol. 26, pp. 454-461, 1980.
- [23] P. Sivagnanam and Y. B. G. Varma, "Subcooled boiling of binary mixtures under conditions of forced convection," *Experimental Thermal and Fluid Science*, vol. 3, pp. 515-522, 1990.
- [24] X. F. Peng, G. P. Peterson, and B. X. Wang, "Flow boiling of binary mixtures in microchanneled plates," *International Journal of Heat and Mass Transfer*, vol. 39, pp. 1257-1264, 1996.
- [25] E. McAssey Jr and S. Kandlikar, "Convective heat transfer of binary mixtures under flow boiling conditions," in *Two-Phase Flow Modelling and Experimentation 1999, Proceedings of the 2nd International Symposium on Two-phase Flow Modeling and Experimentation, Pisa, Italy*, pp. 271-278, 1999.
- [26] W. Rivera, A. Xicale, and O. García-Valladares, "Boiling heat transfer coefficients inside a vertical smooth tube for the water/lithium bromide mixture," *International Journal of Energy Research*, vol. 27, pp. 265-275, 2003.
- [27] S. G. Kandlikar and M. Bulut, "An Experimental Investigation on Flow Boiling of Ethylene-Glycol/Water Mixtures," *Journal of Heat Transfer*, vol. 125, pp. 317-325, 2003.
- [28] P. H. Lin, B. R. Fu, and C. Pan, "Critical heat flux on flow boiling of methanol–water mixtures in a diverging microchannel with artificial cavities," *International Journal of Heat and Mass Transfer*, vol. 54, pp. 3156-3166, 2011.
- [29] B. R. Fu, M. S. Tsou, and C. Pan, "Boiling heat transfer and critical heat flux of ethanol–water mixtures flowing through a diverging microchannel with artificial cavities," *International Journal of Heat and Mass Transfer*, vol. 55, pp. 1807-1814, 2012.
- [30] M. M. Sarafraz and S. M. Peyghambarzadeh, "Experimental study on subcooled flow boiling heat transfer to water–diethylene glycol mixtures as a coolant inside

- a vertical annulus," *Experimental Thermal and Fluid Science*, vol. 50, pp. 154-162, 2013.
- [31] K. G. Joback, "Design molecules possessing desired physical properties," Ph.D., Massachusetts Institute of Technology, Cambridge, Massachusetts., 1989.
- [32] T. W. G. Solomons, *Organic chemistry*. New York: Wiley, 1992.
- [33] K. G. Joback and R. C. Reid, "Estimation of Pure Component Properties from Group Contributions," *Chemical Engineering Communications*, vol. 57, pp. 233-243, 1987.
- [34] L. Constantinou and R. Gani, "New group contribution method for estimating properties of pure compounds," *AIChE Journal*, vol. 40, pp. 1697-1710, 1994.
- [35] G. M. Wilson and J. L. V., "Critical constants  $T_c$ ,  $P_c$ , estimation based on zero, first and second order methods," presented at the AIChE Spring Meeting, New Orleans, LA, 1996.
- [36] J. Marrero and R. Gani, "Group-contribution based estimation of pure component properties," *Fluid Phase Equilibria*, vol. 183–184, pp. 183-208, 2001.
- [37] P. Warriar, "Design and evaluation of heat transfer fluids for direct immersion cooling of electronic systems," Ph.D., Chemical Engineering, Georgia Institute of Technology, Atlanta, GA, 2012.
- [38] R. L. Rowley, W. V. Wilding, J. L. Oscarson, Y. Yang, and N. F. Giles. (2010). *DIPPR® Data Compilation of Pure Chemical Properties*. Available: <http://dippr.byu.edu>
- [39] C. A. P. E. Center. *Integrated Computer Aided System*. Available: <http://www.capec.kt.dtu.dk/Software/ICAS-and-its-Tools/>
- [40] *International Technology Roadmap for Semiconductors*, (2010)  
Available: <http://www.itrs.net/Links/2010ITRS/Home2010.htm>
- [41] W. M. Rohsenow, *A method of correlating heat transfer data for surface boiling of liquids*. Cambridge, Mass.: M.I.T. Division of Industrial Cooperation, 1951.

- [42] G. M. Lazarek and S. H. Black, "Evaporative heat transfer, pressure drop and critical heat flux in a small vertical tube with R-113," *International Journal of Heat and Mass Transfer*, vol. 25, pp. 945-960, 1982.
- [43] T. N. Tran, M. W. Wambsganss, and D. M. France, "Small circular- and rectangular-channel boiling with two refrigerants," *International Journal of Multiphase Flow*, vol. 22, pp. 485-498, 1996.
- [44] P. Warriar, A. Sathyanarayana, D. V. Patil, S. France, Y. Joshi, and A. S. Teja, "Novel heat transfer fluids for direct immersion phase change cooling of electronic systems," *International Journal of Heat and Mass Transfer*, vol. 55, pp. 3379-3385, 2012.
- [45] W. R. McGillis, V. P. Carey, J. S. Fitch, and W. R. Hamburgren, "Boiling binary mixtures at subatmospheric pressures," in *Thermal Phenomena in Electronic Systems, 1992. I-THERM III, InterSociety Conference on*, pp. 127-136, 1992.
- [46] R. M. Flynn, D. S. Milbrath, J. G. Owens, D. R. Vitcak, and H. Yanome, "Azeotrope-like compositions and their use," USA Patent, 2001.
- [47] K. N. Marsh, *Recommended reference materials for the realization of physicochemical properties*. Oxford [Oxfordshire]; Boston: Blackwell Scientific Publications, 1987.
- [48] J. G. Bleazard and A. S. Teja, "Thermal Conductivity of Electrically Conducting Liquids by the Transient Hot-Wire Method," *Journal of Chemical & Engineering Data*, vol. 40, pp. 732-737, 1995.
- [49] P. Griffith, J. D. Wallis, and D. S. R. P. n. Massachusetts Institute of Technology. Division of Industrial Cooperation, *The role of surface conditions in nucleate boiling*. Cambridge, Mass.: Massachusetts Institute of Technology, Division of Industrial Cooperation, 1958.
- [50] *Ramehart Model 250 Goniometer*, (2013), *PDF Brochure*. Available: <http://www.ramehart.com/250.htm>
- [51] J. M. Prausnitz, R. M. Lichtenthaler, and E. G. De Azevedo, *Molecular thermodynamics of fluid-phase equilibria*. New Jersey: Prentice Hall, 1998.

- [52] A. Klamt, *COSMO-RS : from quantum chemistry to fluid phase thermodynamics and drug design*, 1st ed. Amsterdam: Boston, 2005.
- [53] Y. Im, "Copper Nanowire and Flower-Like CuO Nanostructure Surfaces for Enhanced Boiling," Ph.D. Thesis, Korea Advanced Institute of Science and Technology, 2010.
- [54] S. J. Kline and F. A. McClintock, "Describing Uncertainties in Single-Sample Experiments," *Mech. Eng.*, p. 3, 1953.
- [55] Y. Im, "Copper Nanowire and Flower-like CuO Nanostructure Surfaces for Enhanced Boiling," PhD Doctoral Thesis, School of Mechanical, Aerospace and Systems Engineering, Korea Advanced Institute of Science and Technology, Republic of Korea, 2010.
- [56] S. Ahmed and V. P. Carey, "Effects of gravity on the boiling of binary fluid mixtures," *International Journal of Heat and Mass Transfer*, vol. 41, pp. 2469-2483, 1998.
- [57] A. Bar-Cohen and A. McNeil, "Parametric effects of pool boiling critical heat flux in dielectric liquids," in *Proceedings of the Engineering Foundation Conference on Pool and External Flow Boiling*, Santa Barbara, CA, pp. 171-175, 1992.
- [58] N. Zuber, "Hydrodynamic aspects of boiling heat transfer," Ph.D., Physics and Mathematics, University of California, Los Angeles, 1959.
- [59] J. H. Lienhard, V. K. Dhir, and D. M. Rihard, "Peak pool boiling heat-flux measurements on finite horizontal flat plates," *Journal of Heat Transfer*, vol. 95, pp. 477 - 482, 1973.
- [60] R. Chen, M. C. Lu, V. Srinivasan, Z. Wang, H. H. Cho, and A. Majumdar, "Nanowires for enhanced boiling heat transfer," *Nano Lett*, vol. 9, pp. 548-53, Feb 2009.
- [61] S. G. Liter and M. Kaviany, "Pool-boiling CHF enhancement by modulated porous-layer coating: theory and experiment," *International Journal of Heat and Mass Transfer*, vol. 44, pp. 4287-4311, 2001.

- [62] M. Sussman, P. Smereka, and S. Osher, "A Level Set Approach for Computing Solutions to Incompressible Two-Phase Flow," *Journal of Computational Physics*, vol. 114, pp. 146-159, 1994.
- [63] G. Son and V. K. Dhir, "A Level Set Method for Analysis of Film Boiling on an Immersed Solid Surface," *Numerical Heat Transfer, Part B: Fundamentals*, vol. 52, pp. 153-177, 2007.
- [64] S. Tanguy, T. Ménard, and A. Berlemont, "A Level Set Method for vaporizing two-phase flows," *Journal of Computational Physics*, vol. 221, pp. 837-853, 2007.
- [65] E. Olsson and G. Kreiss, "A conservative level set method for two phase flow," *Journal of Computational Physics*, vol. 210, pp. 225-246, 2005.
- [66] Y. C. Chang, T. Y. Hou, B. Merriman, and S. Osher, "A Level Set Formulation of Eulerian Interface Capturing Methods for Incompressible Fluid Flows," *Journal of Computational Physics*, vol. 124, pp. 449-464, 1996.
- [67] J.-J. Xu, Z. Li, J. Lowengrub, and H. Zhao, "A level-set method for interfacial flows with surfactant," *Journal of Computational Physics*, vol. 212, pp. 590-616, 2006.
- [68] A. Q. Raeini, M. J. Blunt, and B. Bijeljic, "Modelling two-phase flow in porous media at the pore scale using the volume-of-fluid method," *Journal of Computational Physics*, vol. 231, pp. 5653-5668, 2012.
- [69] C. W. Hirt and B. D. Nichols, "Volume of fluid (VOF) method for the dynamics of free boundaries," *Journal of Computational Physics*, vol. 39, pp. 201-225, 1981.
- [70] S. W. J. Welch and J. Wilson, "A Volume of Fluid Based Method for Fluid Flows with Phase Change," *Journal of Computational Physics*, vol. 160, pp. 662-682, 2000.
- [71] M. Renardy, Y. Renardy, and J. Li, "Numerical Simulation of Moving Contact Line Problems Using a Volume-of-Fluid Method," *Journal of Computational Physics*, vol. 171, pp. 243-263, 2001.

- [72] A. J. James and J. Lowengrub, "A surfactant-conserving volume-of-fluid method for interfacial flows with insoluble surfactant," *Journal of Computational Physics*, vol. 201, pp. 685-722, 2004.
- [73] G. Tryggvason, B. Bunner, A. Esmaeeli, D. Juric, N. Al-Rawahi, W. Tauber, J. Han, S. Nas, and Y. J. Jan, "A Front-Tracking Method for the Computations of Multiphase Flow," *Journal of Computational Physics*, vol. 169, pp. 708-759, 2001.
- [74] S. O. Unverdi and G. Tryggvason, "A front-tracking method for viscous, incompressible, multi-fluid flows," *Journal of Computational Physics*, vol. 100, pp. 25-37, 1992.
- [75] A. Esmaeeli and G. Tryggvason, "Direct numerical simulations of bubbly flows. Part 1. Low Reynolds number arrays," *Journal of Fluid Mechanics*, vol. 377, pp. 313-345, 1998.
- [76] J. Glimm, J. W. Grove, X. L. Li, K. M. Shyue, Y. Zeng, and Q. Zhang, "Three-dimensional front tracking," *SIAM Journal on Scientific Computing*, vol. 19, pp. 703-727, 1998.
- [77] S. Chen and G. D. Doolen, "Lattice Boltzmann Method for Fluid Flows," *Annual Review of Fluid Mechanics*, vol. 30, pp. 329-364, 1998.
- [78] T. Lee and C.L. Lin, "Pressure evolution lattice-Boltzmann-equation method for two-phase flow with phase change," *Physical Review E*, vol. 67, p. 056703, 2003.
- [79] K. Sankaranarayanan, X. Shan, I. G. Kevrekidis, and S. Sundaresan, "Analysis of drag and virtual mass forces in bubbly suspensions using an implicit formulation of the lattice Boltzmann method," *Journal of Fluid Mechanics*, vol. 452, pp. 61-96, 2002.
- [80] T. Reis and T. N. Phillips, "Lattice Boltzmann model for simulating immiscible two-phase flows," *Journal of Physics A: Mathematical and Theoretical*, vol. 40, p. 4033, 2007.
- [81] C. Pan, M. Hilpert, and C. T. Miller, "Lattice-Boltzmann simulation of two-phase flow in porous media," *Water Resources Research*, vol. 40, p. W01501, 2004.

- [82] M. Sussman and E. G. Puckett, "A Coupled Level Set and Volume-of-Fluid Method for Computing 3D and Axisymmetric Incompressible Two-Phase Flows," *Journal of Computational Physics*, vol. 162, pp. 301-337, 2000.
- [83] Z. Wang, J. Yang, B. Koo, and F. Stern, "A coupled level set and volume-of-fluid method for sharp interface simulation of plunging breaking waves," *International Journal of Multiphase Flow*, vol. 35, pp. 227-246, 2009.
- [84] T. Ménard, S. Tanguy, and A. Berlemont, "Coupling level set/VOF/ghost fluid methods: Validation and application to 3D simulation of the primary break-up of a liquid jet," *International Journal of Multiphase Flow*, vol. 33, pp. 510-524, 2007.
- [85] G. Son, "Efficient Implementation of a Coupled Level-Set and Volume-of-Fluid Method for Three-Dimensional Incompressible Two-Phase Flows," *Numerical Heat Transfer, Part B: Fundamentals*, vol. 43, pp. 549-565, 2003.
- [86] H. A. Akhlaghi Amiri and A. A. Hamouda, "Evaluation of level set and phase field methods in modeling two phase flow with viscosity contrast through dual-permeability porous medium," *International Journal of Multiphase Flow*, vol. 52, pp. 22-34, 2013.
- [87] J. Feng, C. Liu, J. Shen, and P. Yue, "An Energetic Variational Formulation with Phase Field Methods for Interfacial Dynamics of Complex Fluids: Advantages and Challenges," in *Modeling of Soft Matter*. vol. 141, M.-C. Calderer and E. Terentjev, Eds., ed: Springer New York, pp. 1-26, 2005.
- [88] J. W. Cahn and J. E. Hilliard, "Free Energy of a Nonuniform System. I. Interfacial Free Energy," *The Journal of Chemical Physics*, vol. 28, pp. 258-267, 1958.
- [89] COMSOL. (August 2013). *Boiling Water*. Available: [http://www.comsol.com/model/download/176245/models.cfd.boiling\\_water.pdf](http://www.comsol.com/model/download/176245/models.cfd.boiling_water.pdf)
- [90] P. Yue, J. J. Feng, C. Liu, and J. Shen, "A diffuse-interface method for simulating two-phase flows of complex fluids," *Journal of Fluid Mechanics*, vol. 515, pp. 293-317, 2004.
- [91] P. Yue, C. Zhou, J. J. Feng, C. F. Ollivier-Gooch, and H. H. Hu, "Phase-field simulations of interfacial dynamics in viscoelastic fluids using finite elements with adaptive meshing," *J. Comput. Phys.*, vol. 219, pp. 47-67, 2006.



- [92] D. Jamet. (August 2013). *Diffuse Interface Models in Fluid Mechanics*. Available: <http://pmc.polytechnique.fr/mp/GDR/docu/Jamet.pdf>
- [93] *COMSOL Multiphysics guide*. (August 2013). Available: [www.comsol.com](http://www.comsol.com)
- [94] W. Fritz, "Maximum Volume of Vapor Bubbles," *Physik Zeitschr*, vol. 36, pp. 379-384, 1935.
- [95] R. Cole and W. Rohsenow, "Correlations for Bubble Departure Diameters for Boiling of Saturated Liquids," *Chemical Engineering Progress*, vol. 65, pp. 211-213, 1969.
- [96] I. G. Malenkov, "Detachment frequency as a function of size for vapor bubbles," *Journal of engineering physics*, vol. 20, pp. 704-708, 1971.
- [97] Z. Yao, Y. W. Lu, and S. G. Kandlikar, "Effects of nanowire height on pool boiling performance of water on silicon chips," *International Journal of Thermal Sciences*, vol. 50, pp. 2084-2090, 2011.
- [98] A. K. Das, P. K. Das, and P. Saha, "Nucleate boiling of water from plain and structured surfaces," *Experimental Thermal and Fluid Science*, vol. 31, pp. 967-977, 2007.
- [99] M.-C. Lu, R. Chen, V. Srinivasan, V. P. Carey, and A. Majumdar, "Critical heat flux of pool boiling on Si nanowire array-coated surfaces," *International Journal of Heat and Mass Transfer*, vol. 54, pp. 5359-5367, 2011.
- [100] J. P. McHale, S. V. Garimella, T. S. Fisher, and G. A. Powell, "Pool Boiling Performance Comparison of Smooth and Sintered Copper Surfaces with and Without Carbon Nanotubes," *Nanoscale and Microscale Thermophysical Engineering*, vol. 15, pp. 133-150, 2011.
- [101] R. Kathiravan, R. Kumar, A. Gupta, and R. Chandra, "Preparation and Pool Boiling Characteristics of Silver Nanofluids Over a Flat Plate Heater," *Heat Transfer Engineering*, vol. 33, pp. 69-78, 2011.
- [102] [www.mcmaster.com](http://www.mcmaster.com). (2013) Available: <http://www.mcmaster.com/#garolite/=o796g3>

- [103] A. Bar-Cohen, J. Sheehan, and E. Rahim, "Two-Phase Thermal Transport in Microgap Channels—Theory, Experimental Results, and Predictive Relations," *Microgravity Science and Technology*, vol. 24, pp. 1-15, 2012.
- [104] P. Lee, "Experimental Investigations of Two-Phase Cooling in Microgap Channel," National Institute of Singapore, Technical Report, 2011.